Aalborg University

Master Thesis

Plasmonic Nanoparticles for Advanced Sensing and Detection

Authors:
Arūnė Makarevičiūtė
Francesco Zamboni

Supervisor:
Vladimir N. Popok

The Faculty of Engineering and Science
Department of Materials and Production

3rd of June 2021

AALBORG UNIVERSITY
STUDENT REPORT

AALBORG UNIVERSITY

S T U D E N T   R E P O R T

Title:

Plasmonic Nanoparticles for Advanced Sensing and Detection

Project:

Master Thesis

Project period:

September 2020 - June 2021

Project group:

MNNF4 - 5.321c

Members:

Arūnė Makarevičiūtė
Francesco Zamboni

Supervisor:

Vladimir N. Popok

Number of pages: 74
Appendix: 8 pages
Ended 03-06-2021

Abstract:

Metallic nanoparticles possess an optical effect named localized surface plasmon resonance (LSPR). It leads to enhancement of electric field in the proximity of nanoparticle during irradiation with light. This effect is applicable in sensing and detection methods, where metallic nanoparticles facilitate the detection of the signal from analyte with trace level concentration. In this work, gas-aggregated copper and silver nanoparticles, with diameters ranging from $7\,nm$ to $26\,nm$, were investigated. LSPR stability over time was studied for Cu NPs with different sizes. The plasmonic bands of the nanoparticles, kept in ambient atmosphere, were found to be preserved over the period of 6 months, while band parameters exhibited gradual change, related to oxidation. It was also found that UV-ozone treatment of Cu NPs led to the formation of oxide phase, which facilitated the plasmon band stability on a long time scale. Cu NPs were further used in the Surface Enhanced Raman Spectroscopy (SERS) and Matrix Assisted Laser Desorption Ionization Mass Spectroscopy (MALDI MS). A moderate signal enhancement was obtained. SERS substrates with Ag NPs showed better efficiency, reaching enhancement factor up to ~ 3.63×10^5 and possibility to detect methylene blue with concentration as low as $10^{-8}\,M$. MALDI measurements of pig brain and beeswax showed strong signals of negative phospholipid ions when matrices of Ag NPs were employed.

Preface

This project report was written by the undersigned authors during their 3$^{\text{rd}}$ and 4$^{\text{th}}$ semesters of Master's degree studies in Materials and Nanotechnology, Nanomaterials and Nanophysics at the Department of Materials and Production at Aalborg University.

References to literature are made following the IEEE citation style. Figures and equations are abbreviated as Fig. (#) and Eq.(#) respectively. They are also numbered according to respective chapter and section. Unless otherwise stated, all figures are made by authors.

Acknowledgements

Arūnė Makarevičiūtė

Arūnė Makarevičiūtė

Francesco Zamboni

Francesco Zamboni

List of Abbreviations

AFM	Atomic Force Microscopy
EF	Enhancement Factor
EQMS	Electrostatic Quadrupole Mass Selector
LSPR	Localized Surface Plasmon Resonance
MALDI MS	Matrix-Assisted Laser Desorption Ionisation Mass Spectroscopy
MB	Methylene Blue
NP	Nanoparticle
SERS	Surface Enhanced Raman Spectroscopy
UV	Ultraviolet
XPS	X-Ray Photoelectron Spectroscopy

Contents

Chapter 1

Introduction

Nowadays, nanomaterials is an intensively investigated field. Systematic studies of material properties, related with scaling-down the product size, and constant progresses of nanotechnology, led to successful integration of nanosystems in a daily use, and their applicability is constantly expanding.

Due to the reduced size of the system, nanostructures benefit of unique optical, electrical, magnetic and thermal properties which are exploited for a wide range of different applications. For instance, in medicine, metal nanoparticles can be applied in photothermal cancer treatment, with the advantage to prevent undesired side effects, due to the localized light-to-heat conversion [1], or in tissue engineering, where nanostructures of silver and particular metal oxides are used because of their antibacterial activity [2].

Moreover, metallic nanoparticles are known for an unique optical property, called localized surface plasmon resonance (LSPR). This phenomenon occurs when the light source irradiates nanoparticle and collective oscillations of free electrons are induced. As a consequence, electric field is strongly amplified in the proximity of the nanoparticle. This effect is advantageously applied in different areas such as optical systems [3, 4] or medical diagnostics [5–8].

Recently, sensing and detection methods started to use nanoparticles assemblies as an useful tool to overcome limitations of the conventional spectroscopies, improving the performance of analysis and extending the range of applicability. For instance, a variety of silver nanostructures of different shapes, had been successfully employed as a source of enhancement for Raman Scattering signal [9, 10]. In this way, this method allowed to detect concentration of analyte molecules as low as $10^{-10}M$ [11]. Meanwhile, various nanostructured silver surfaces, such as nanopatterns [12] and thin films [13], had been applied as matrices for MALDI MS. Different conventional organic matrices are often suitable for detection of specific analytes only [14], while matrices with silver nanoparticles can be used for detection of molecules in a wide range of masses with possibility of MS imaging [15, 16].

The goal of this project is to fabricate efficient plasmonic substrates and matrices with silver and copper nanoparticles of various sizes. A magnetron-based gas aggregation technique is employed [17] for synthesis of nanoparticles with high chemical purity and monocrystalline structure [18].

Although copper has a strong plasmon response and it is a less expensive alternative to silver, a practically important issue is the rapid oxidation, occurring when this metal is exposed to oxygen-rich environments [19, 20]. Presence of the copper oxide phase significantly affects the plasmon band, limiting the functionality of copper

nanostructures. [21, 22]. In order to identify changes in the composition of copper nanoparticles, stored in ambient atmosphere, periodical XPS measurements are performed. Moreover, the evolution of their plasmon band is analysed by monitoring the LSPR spectra for a period of six months. Different approaches to protect copper nanoparticles from oxidation, such as formation of passive coatings [23, 24], had been presented. In this work, post-deposition treatment in UV-ozone environment, is tested. The resulting formation of an oxide shell prevents from reactions with chemical species, and it improves the stability of plasmonic properties of copper nanoparticles, as already reported by Popok *et al.* [25].

The possibility to enhance the detection signal in SERS is explored using plasmonic substrates, produced in this work. Different parameters, as nanoparticles size and surface coverage, are considered to obtain high enhancement factors.

Similarly, matrices of silver nanoparticles are tested for the efficient detection of lipids with MALDI MS, analyzing the influence of different sizes of nanoparticles on the signal intensity. The capability of this type of matrices to detect small molecules was already demonstrated [26], where a correlation between quality of the mass spectra and nanoparticles size is emphasized. The possibility to reproduce the mass spectra of lipids with matrices of copper nanoparticles, is also investigated. Copper-containing MALDI MS matrices had been already tested in a few studies [27, 28].

The interaction between laser source and silver nanoparticles, during MALDI MS experiments, is studied in order to observe possible structural changes of nanostructres due to the irradiation [29].

Chapter 2

Metal Nanoparticles for Enhanced Sensing

This chapter discusses properties and methods of synthesis of nanoparticles, with a particular focus on the application in sensing and detection methods, which is main motivation of the project.

The distinct properties of metal nanoparticles, related with a size reduction, are introduced in the beginning. Particularly, the localized surface plasmon resonance (LSPR) effect, exhibited by metallic nanostructures, is presented together with its advantageous application in Surface Enhanced Raman Spectrocopy (SERS) and Matrix Assisted Laser Ionisation Desorption Mass Spectroscopy (MALDI MS).

Following section is about synthesis methods of nanoparticles, in which chemical and physical approaches are introduced. The formation of metallic clusters from the gas phase, utilizing magnetron sputtering, has a particular attention. Influence of the process parameters on the product particle size is also discussed.

The section about oxidation of copper is included as this metal is a great candidate for LSPR effect but its performance has a tendency to be strongly affected in ambient atmosphere.

2.1   Properties of Metallic Nanoparticles

Aggregates consisting of countable number (from two up to several hundred thousand) atoms (or molecules) are referred to clusters. [30] It can be formed either from one chemical element or different species and are considered as an intermediate form of the matter between discrete atoms (or molecules) and a bulk. Clusters with sizes ranging in nanometre scale are named nanoparticles. In this work, metal particles in diameters from 7 to $26\,nm$ are investigated. Thus, terms of metallic clusters and metallic nanoparticles have an equal meaning.

Physical properties of metals are strongly affected by the size of the system, resulting in unique behaviour of metallic nanostructures. The first consequence, rising from the reduced size of metal nanoparticle, compared with the bulk metal, is the discretization of the electronic structure, due to the confinement of the electrons.

The finite spacing between consecutive electronic states of nanoparticles, δ, was introduced by Kubo [31]:

$$\delta = 4E_F/3n \qquad\qquad (2.1)$$

where δ is Kubo gap, E_F is the Fermi energy of the bulk metal, and n is the number of valence electrons in the metallic nanoparticle.

As a consequence of the separation between energy states, the electrical conductivity of finite size metal nanostructures changes significantly compared with the corresponding bulk system. For this reason, the Kubo gap is considered as a criterion to predict the behaviour of metal nanoparticles at different temperatures. The metallic particles are considered as electrical conductors if the relation $\delta \le k_B T$ (k_B - Boltzman constant) is satisfied [32]. The Eq. (2.1) is instructive to estimate Kubo gap for nanoparticles of certain metal and with determined size, for instance, silver particle with a diameter of $3\,nm$ consists of ~ 10^3 atoms, and its Kubo gap value would be ~ $7\,meV$. At the room temperature, it is lower than $k_B T$(~ 25 meV) and thus Ag nanoparticle is defined as metallic (electrical conductor). Smaller nanoparticles (which is equivalent to the lower number of valence electrons, n) require higher temperatures to satisfy the condition of metallicity, thus at room temperature they can behave as insulators due to large Kubo gap (Fig. 2.1).

Indeed, emergence of metal-to-insulator transition, due to shrinking the size of the metallic system, was experimentally observed. For instance, an increase of core-level binding energy was found when the size of palladium and silver clusters was reduced [33, 34]. In these studies, the palladium clusters with diameter of ~ $1\,nm$ had binding energy $1.2\,eV$ higher than the bulk metal value, manifesting non-metallicity.

Furthermore, the reduction of size of the metallic structures had been found to result in lower melting temperatures. Experiments with gold nanoclusters showed a decrease of melting temperature of down to $300\,K$ for the smallest investigated size (several tens Å). This temperature is drastically lower than melting point of bulk gold (~ $1300\,K$). The observed trend was in the agreement of size-scaling law $T \sim 1/R$, valid in a large cluster regime ($>10^4$ constituent atoms). [30]

However, the melting temperature of small clusters (~ 10^2 atoms) does not evolve monotonically with reduction of size but is rather dependant on the complete formation of the outer layer of the cluster. Investigation of sodium clusters, consisting from
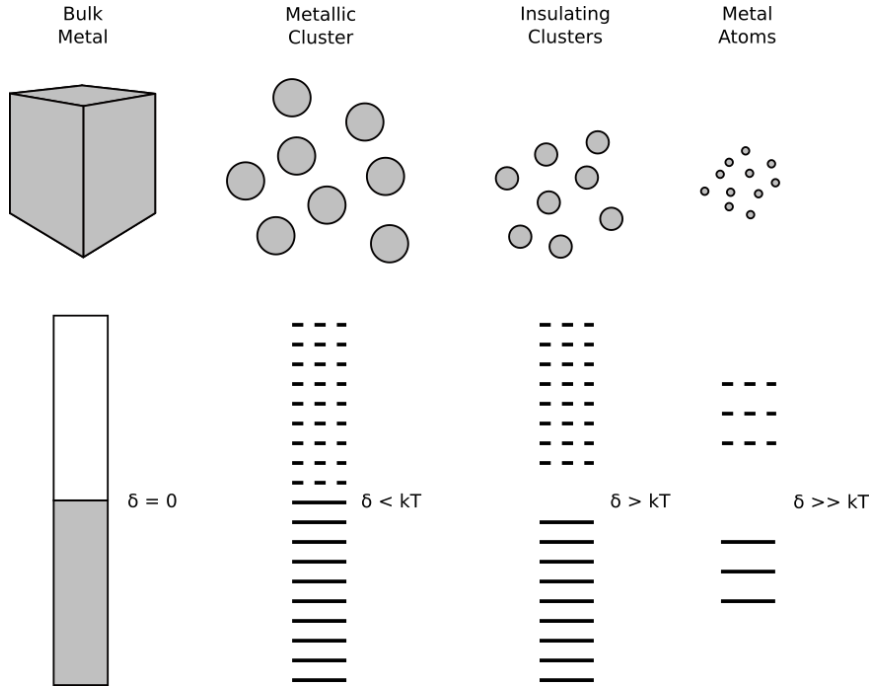
FIGURE 2.1: Representation of the increase of Kubo gap, δ, related
with a reduced size of the metallic systems (upper row)

several tens up to few hundred atoms, demonstrated evident peaks and minima of
melting temperature [35]. The change of cluster size by few atoms resulted in melting
temperature deviation by ~10 %. It was attributed to mobile surface atoms of icosa-
hedrons with incomplete outer shell facilitating melting process. Meanwhile, clusters
having fully closed icosahedra structure require higher melting temperatures.

Beyond aforementioned changes of metallic properties, particle size reduction also af-
fects the metal-light interaction. Free electrons of nanoparticle interacts with the elec-
tromagnetic wave, resulting in collective oscillations, responsible for increased light ab-
sorption and scattering, with a maximum at the resonance frequency. This behaviour
of metal nanoparticles is known as LSPR and is the subject of intensive research due
to the variety of advantageous applications, for instance, the improvement of sensing
and detection methods, discussed in the following section.

2.1.1 Localized Surface Plasmon Resonance

Metals are widely used as optical materials due specific behaviour in absorption and
scattering of electromagnetic waves. Specifically, metallic nanoparticles exhibit partic-
ular optical response, where incident electromagnetic field induce collective oscillations
of free electrons and strong local field enhancement is observed.

LSPR can be described by Mie theory [36], where the effect is studied considering
quasi-static regime approximation, thus assuming spherical particles with radius much
smaller than the wavelength of incident light ($r << \lambda$, see Fig. 2.2). Therefore, the
oscillating electromagnetic field is considered to be constant over entire volume of
particle, i.e, phase shifts are neglected. The Mie theory provided an analytical solution
of Maxwell's equations for the interaction of metallic particle and electromagnetic
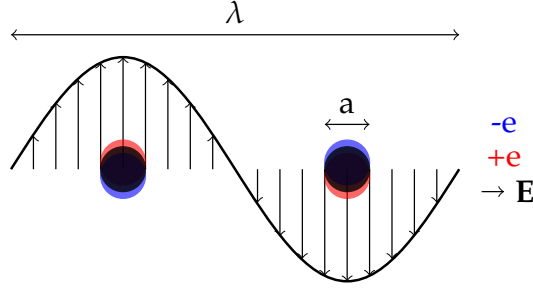radiation.

FIGURE 2.2: Schematic representation of electron oscillations, induced in the metallic nanoparticle by the electromagnetic field, in the quasi-static regime ($a << \lambda$)

The LSPR effect is commonly quantified in terms of the extinction cross section, which is the sum of absorption and scattering processes, $C_{ext}=C_{abs}+C_{sca}$. After interaction with metallic particle, the intensity of the incident light is reduced due to absorption or scattering. [37] The intensity changes for completely absorbing or scattering particle are given by [37]:

$$\triangle I_{abs/sca}(z) = I_0\left(1 - e^{-nC_{abs/sca}z}\right) \qquad (2.2)$$

where I_0 is intensity of incident light, n is number density of clusters, and z is the thickness of the sample.

Derived from Mie theory for the dipole mode, C_{ext} is given by [37]:

$$C_{ext} = \frac{24\pi^2 r^3 \varepsilon_m^{3/2}}{\lambda} \cdot \left[\frac{\varepsilon_i}{\left(\varepsilon_r + 2\varepsilon_m\right) + \varepsilon_i^2}\right] \qquad (2.3)$$

where r is radius of the particle, ϵ_m is dielectric constant of the surrounding medium, ϵ_r and ϵ_i are real and imaginary parts, respectively, of dielectric function of the plasmonic material, and λ is excitation wavelength. The resonance condition is related with a dielectric function of the metal: the denominator in brackets of the Eq. (2.3) has to be minimum, thus, ϵ_r must be negative and ϵ_i values should be close to zero, in order to achieve strong plasmonic response. In other words, the resonant electromagnetic field enhancement is achieved under the condition:

$$\epsilon_r = -2\epsilon_m \qquad (2.4)$$

which is know as Fröhlich's condition [38]. Particular metals satisfy the criterion of dielectric function with a high efficiency and demonstrate strong LSPR effect under the interaction with visible light. Moreover, excitation wavelength (frequency) dictates the choice of the metal. For instance, aluminium plasmon band is limited in UV region, while gold has large plasmon damping at wavelenghts longer than $500\,nm$. [39] Besides this optical property, one has to consider chemical inertness of the metal. For example, lithium supports plasmons but is very reactive and practically is rarely used. Copper is a great candidate for plasmonic applications but is prone to oxidation, where the presence of the oxide can affect the LSPR response of the nanostructure [25].

Another parameter, affecting the extinction cross section of the metal particle is the size. The particle size effects for LSPR were discussed in detail by Kreibig and Volmer [37]. The increase of the particle size leads to formation of multipole modes due to phase retardation. Therefore, correction of Mie theory have to be considered for particles with radii, larger than quasi-static limit. Moreover, whilst absorption is dominant term in extinction cross section for particles with small radii, in the case of larger particles it fades away and scattering contribution becomes stronger. In addition, the large distribution of particle sizes results in wider plasmon resonance peaks. The shape and the arrangement of the nanostructures also has an influence on the local electric field enhancement. Although Mie theory described LSPR effect of metallic spheroids, nanostructures with sharp edges can exhibit even more intense field, for instance, at the corners of the nanocube and are much larger compared with the nanospheres in the same dimensions. [40] An enhanced electric field can be even stronger at so called hot-spots - specific regions between plasmonic nanostructures, arranged in close distances, such as two spherical silver particles, separated by few nanometres.[41]

The LSPR effect can facilitate other physical processes, such as strong local heating [42, 43], and had attracted scientific interest due to advantageous application, for example, in photothermal cancer treatment. In comparison, $\sim 40\,nm$ gold nanoparticles have molar absorption coefficient of $\sim 8 \times 10^9 M^{-1} cm^{-1}$ at plasmonic resonance which is greatly larger than molar coefficient of extinction $\sim 10^4 M^{-1} cm^{-1}$ of indocyanine green dye, commonly used for laser treatment of tumors. [44] However, disease affected tissues are located deeply into the body, thus radiation treatment requires laser light in near-infrared spectral region, where human tissues are transparent. Therefore, nano-sized gold spheroids are not suitable since their plasmonic band lies in lower wavelengths region and tailoring different shape of nanoparticles is possibility to overcome this problem. Nanorods is a great candidate for tuning the plasmonic band. Rod-shaped nanoparticles of gold exhibit two plasmon resonances, transverse and longitudinal, where the former has the same wavelength as spheroids, while latter shows more intense LSPR band at longer wavelenghts and is linearly red-shifting with an increase of aspect ratio. [45, 46]

The proper combination of aforementioned parameters, affecting the plasmon band, such as material, particle size, shape and arrangement allows to apply metallic nanostructures for the improvement of various detection techniques [47, 48]. This application area is of the interest of this work and is further discussed in following sections.

2.2   Raman Scattering Effect

The Raman scattering effect is an optical process originating from the interaction between light and molecules. It was first observed in 1921 by Chandrasekhara Venkata Raman using the sun as light source, and lately he was awarded with the Nobel prize in physics for this discovery [49].

The scattering process involves the simultaneous absorption of an incident photon, coupled with an upward transition to a virtual state of the electron in the molecule, and the emission of another photon, corresponding to a downward transition. Considering energies of the incident and the emitted photons, scattering process is classified as *elastic scattering* (Rayleigh scattering, Fig. 2.3a), when it does not involve any energy loss, and *inelastic scattering* (Raman scattering, Fig. 2.3b), when the emitted photon

gains or loses energy, compared with the incident one, because of the interaction with the molecule.

Thus, this mechanism corresponds to a downward transition of the electron from a virtual state at higher energy to a different vibration/rotational state compared to the initial one, considered before illumination from the excitation source.
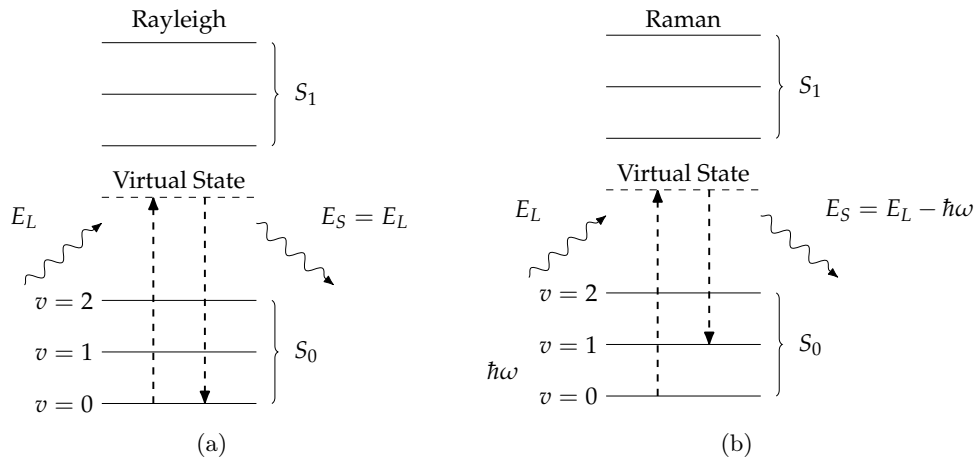

FIGURE 2.3: Schematic representation of a) Rayleigh scattering and b) Raman scattering. The solid horizontal lines correspond to vibrational states of the molecule. The dashed arrows show the transitions between different electronic states, S_0 and S_1. E_L and E_S are the energies of the excitation light and scattered light, respectively

The Raman scattering process is further classified according to the energy difference between the incident and the emitted photon. When the emitted photon has a lower energy compared with the incident one, the molecule is excited to an higher state as shown in Fig. 2.4a and this process is called *Stokes process*. On the other hand, when the emitted photon gains energy from the molecule, corresponding to an increase of its energy, compared with the incident photon, and the relaxation of the molecule to a lower state, this transition is called *Anti Stokes* (Fig. 2.4b). Consequently, detection of scattered photons, obtained by Raman spectroscopy, allows to define the specific vibrational structure of molecules. Hence, this technique is widely applied for chemical analysis.

However, the Raman scattering gives a weak signal, especially for transitions related with a larger energy difference, and for Anti-Stokes process, since the molecules have to be in an initial excited state. In the last decades, active research focused on the development of a new technique, aiming to improve the Raman signal. With this purpose, the recent advancements in the field of plasmonic nanostructures fabrication, opened the possibility to significantly improve the performances of Raman spectroscopy.

2.3   Metallic Nanoparticles for Raman Detection

The increase of the Raman scattering of molecules adsorbed on a roughed surface, was firstly observed by Fleischmann et al. [50], and initially attributed to the increase of the surface area. This result was followed by active research aiming to fabricate substrates capable to experimentally achieve strong Raman signals [51, 52], and find a theoretical explanation for this enhancement [53]. Moskovits [54] was the first to
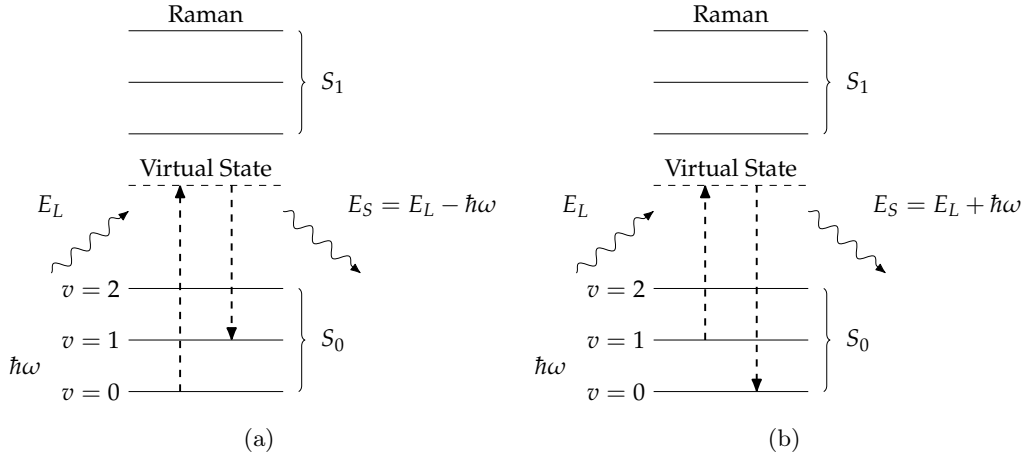
FIGURE 2.4: Schematic of Raman Scattering processes: a) Stokes, b)
Anti Stokes

attribute this effect to the plasmonic properties of structured metallic surfaces when interacting with a light source. It led to development of a new detection method named Surface Enhanced Raman Spectroscopy (SERS), which exploits advanced fabrication techniques of surface modification for the preparation of substrates which show SERS activity.
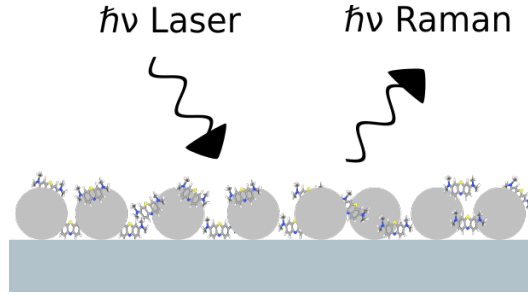

FIGURE 2.5: Schematic representation of Raman scattering process, where the plasmonic SERS substrate with spherical nanoparticles is used

In a conventional Raman experiment, the electromagnetic field of the incident light beam, $\mathbf{E}_{\text{Inc}}$, interacting with the molecule, induces a Raman dipole, $\mathbf{p}_{\text{R}} = \alpha_{\text{R}}\mathbf{E}_{\text{Inc}}$. Its oscillations are characterized by a specific frequency, ω_R, related with the polarizability of the molecule, $\alpha_{\text{R}}(\omega_R)$. Thus, the Raman signal is attributed to the emission from the induced Raman dipole. [55] A similar mechanism occurs when the molecule is placed in the vicinity of a metallic nanostructure (see Fig. 2.5), where the electric field is localized in narrow regions, called *hot spots*. The geometry of the plasmonic structure and its position, relative to the surrounding, affect the intensity of the SERS activity. Consequently, the hot spots are classified as *first generation* when they involve a single nanostructure, *second generation* when the field is confined between coupled nanostructure, and *third generation* when the confinement occurs between the nanostructure and the supporting material. In these conditions, the electromagnetic field is significantly modified and its intensity can differ by many orders of magnitude, according to the specific characteristics of the hot spot [56]. However, the fabrication of second and third generation hot-spots requires the employment of sophisticated production methods.

In these conditions, the amplitude of the incident electromagnetic field is dramatically enhanced when the excitation wavelength of the laser source is in the same range as the plasmon band of the metal, producing a *local field enhancement*. The modified electromagnetic field, $\mathbf{E}_{\mathrm{Loc}}$, induces a Raman dipole, $\mathbf{p}_{\mathrm{R}} = \alpha_{\mathrm{R}}\mathbf{E}_{\mathrm{Loc}}$, which emission in free space will be enhanced by a factor:

$$M_{\mathrm{Loc}} = \frac{|\mathbf{E}_{\mathrm{Loc}}|^2}{|\mathbf{E}_{\mathrm{Inc}}|^2} \tag{2.5}$$

At the same time, a second mechanism of enhancement results from the modification of the radiation properties of the Raman dipole. Thus, it is labeled as *radiation enhancement*. In SERS condition, the power emitted from an oscillating dipole, placed in close proximity of a metal surface, can be many order of magnitudes larger than the power radiated by the same dipole in free space. However, the efficiency of this mechanism is dependent on many parameters, like the geometry and dielectric function of the metal structure, the dipole position and orientation. Therefore, part of the enhancement is associated with the coupling of the Raman dipole oscillations with the free electron oscillations of metal nanostructure [57].

A secondary effect, usually neglected to estimate the total enhancement, is the *chemical enhancement* related with interaction between the analyte molecules and the SERS active substrate.

The enhance of the Raman signal is usually estimated quantitatively by the *Enhancement Factor* (EF), exhaustively studied by LeRu *et al.* [58]. Considering the SERS signal from a single molecule, the single molecule enhancement factor, SMEF, can be expressed as:

$$\mathrm{SMEF} \approx M_{\mathrm{Loc}}(\omega_L)M_{\mathrm{Rad}}^d(\omega_R) \tag{2.6}$$

where $M_{\mathrm{Rad}}^d(\omega_R)$ accounts for the radiation enhancement.

However, it has to be stressed that the magnitude of enhancement, of the Raman signal in SERS conditions, is affected by many factors, such as characteristics of the laser excitation, the detection setup, SERS substrate, properties of analyte and the interaction between the analyte and the substrate. Therefore, in order to precisely evaluate the enhancement factor, the signal from a conventional Raman setup has to be compared with a SERS setup, involving the same analyte molecule and the same environment. A proper choice of the experimental parameters is necessary to compare the results, obtained from different plasmonic substrates [58].

Moreover, the large number of parameters, such as non-uniform spatial distribution of analyte molecules, leads to highly non-uniform enhancement across the substrate. The quantitative comparison of different substrates can be obtained through the definition of a SMEF, which is evaluated only at specific locations on the substrate, or alternatively, an *average EF*, which identifies an average property of the substrates considered.

The *average* EF is often preferable, rather than the SMEF, due to the complexity of the experimental setup and the difficult control of arrangement of nanostructures, required in the latter case. In this case, the performance of SERS substrates is expressed according to [58]:

$$\text{EF} = \frac{\text{I}_{\text{SERS}}/\text{N}_{\text{SERS}}}{\text{I}_{\text{NR}}/\text{N}_{\text{NR}}} \tag{2.7}$$

where N_{SERS} and N_{NR} are the average number of molecules in the scattering volume, of SERS and normal Raman experiments, respectively, meanwhile I_{SERS} and I_{NR} are the respective intensities of the detected signal.

A more practical approach to evaluate the signal enhancement, is it to consider the *analytical* EF, defined as the ratio between the intensity of the SERS signal and the normal Raman signal, both normalized to the different concentrations of the same analyte:

$$\text{AEF} = \frac{\text{I}_{\text{SERS}}/\text{c}_{\text{SERS}}}{\text{I}_{\text{NR}}/\text{c}_{\text{NR}}} \tag{2.8}$$

In order to compare the analytical enhancement factor for different substrates, it is necessary to precisely describe the experimental setup and procedure. However, it is important to emphasize that it does not provide a physically correct value of the enhancement factor because the SERS signal can be wrongly estimated, as the number of molecule, excited during the experiment, is dependent on the adsorption characteristic of the molecular species on the substrate. The amount of analyte molecules deposited on the substrates, is generally different from the concentration c_{SERS} in liquid solution, considered in the analytical definition 2.8.

Development of SERS spectroscopy, obtaining large values of the enhancement factor, opened the possibility for high sensitivity analysis. For instance, single molecule detection was achieved in the experiments of Kneipp *et al.* [59] and Nie and Emory [60], who studied the scattered signal from different dyes molecules, in a solution of colloidal silver nanoparticles. Consequently, SERS is considered as a promising technique with possible applications in different fields, where the detection of trace concentrations of analyte is required.

However, the fabrication of SERS active substrates is a difficult task, which requires to combine different aspects as suggested by Natan [61] and Lin *et al.* [52]. Ideally, the application of SERS active substrate demands a high enhancement factor, to ensure a clear improvement of the Raman spectroscopy setup. Moreover, an uniform distribution of the enhancement and reproducibility of the measurement, are required to ease the comparison of different measurement with the same analyte. Meanwhile, regarding the fabrication procedure, it is necessary to guarantee the stability of the performance of the substrate over a sufficiently long time period, a relatively low-cost of production, and the cleanliness of the surface.

The first step for the design of a proper SERS active substrate, is the accurate choice of the plasmonic material employed. Different materials have been proposed, and intensive studies were carried out with noble metals due to LSPR. For this reason, silver and gold are the most common materials to improve a normal Raman spectroscopy, meanwhile aluminium has potential application for excitation in the UV range of the spectrum. Moreover, novel structures have been proposed in the last three years, combining different plasmonic materials, including bimetallic silver and gold nanoparticles, zinc oxide and metal heterostructures, and metal oxides based nanostructures [62]. For instance, William *et al.* [63] obtained a single molecule SERS with a sprouted potato-shaped Ag and Au bimetallic nanoparticles, detecting methylene blue in the

extremely low $10^{-15}\,M$ concentration. Meanwhile, ZnO nanorods coated with Ag nanoparticles revealed a limit of detection of $10^{-9}\,M$ for the same analyte [64]. Recently, a simple method for the production of cost efficient paper-based Au/Ag SERS substrates was presented by Yang *et al.*, for which they measured an enhancement factor of 9.0×10^7 on the spectra of Rhodamine 6G [65]. Moreover, Li presented the advantages and recent studies of flexible and transparent SERS active substrates [66]. Sruchan *et al.* fabricated microporous graphene foam, decorated by Ag NPs for successful SERS detection of methylene blue with a detection limit of $10^{-9}\,M$. [67]

The large enhancement obtained from gold and silver nanoparticles, opened the possibility to study the effect of other parameters affecting the magnitude of the enhancement. For example, research effort is devoted to explore the advantages of particle with different shapes thanks to the recent advances in nanofabrication techniques. As an example, Zanotti *et al.* [10], recently measured the enhancement factor of Ag nanostructures of different shapes, prepared by chemical methods. According to theoretical prediction [68], it is possible to increase the plasmonic intensity in the area close to sharp edges, supporting the research of novel structures, such as nanostars, in order to obtain larger enhancement rather than spherical nanoparticles.

The possibility to reduce the cost of fabrication relies on on different materials. With this goal, in the last decades, copper attracted more interest. Pettinger *et al.* [69] obtained the first SERS enhancement from a copper electrode in 1980. Later on, different fabrication methods of copper-based SERS substrates have been investigated, reporting enhancement factors varying from 10^1 to 10^8 [70]. Large variation of the reported EF values can be related with different experimental conditions, such as the excitation source or the properties of the surrounding environment, as well as substrate morphology, including nanostructure shape, size and distribution. A proper design of copper SERS substrate can lead to high SERS activity as reported by Keating *et al.* [71], justifying the interest to investigate different fabrication methods, aiming to obtain an enhancement factors, comparable with the performance of gold and silver substrates.

Moreover, the main concern about the possible application of copper, as a plasmonic material for SERS spectroscopy, is related with its tendency to react with atmospheric oxygen and consequent formation of copper oxide, which may induce a reduction of the plasmonic character. Wang *et al.* [72] reported a significant increase of the SERS spectrum of 4-aminobenzenethiol molecules, adsorbed on Si substrates, covered with copper nanodendrites. In their study, the signal emitted from molecules excited with a $532\,nm$ laser source, was larger in the case of a copper core - copper oxide shell compared with pure copper nanostructures. Consequently, this result is promising for the study of copper suitability for the fabrication of SERS substrates, considering the storage in oxidising environments.

2.4   Matrix Assisted Laser/Desorption Ionization Mass Spectroscopy

Mass spectrometry is a powerful and widely spread analytical tool, which relies on the detection of isolated ions, identified according to their mass-to-charge ratio by different instruments. Thus, the acquisition of the mass spectrum of analyzed substance, requires the desorption and ionization of compounds incorporated into the sample. This condition can be obtained thorough different methods. For example, desorption

can be enhanced by pressure difference, particles or ions bombardment, or light radiation. Meanwhile, ionization can be achieved by charge transfer. However, more energetic methods, often named as hard ionization, are source of molecular fragments of the biological analyte, increasing the complexity of the obtained spectra and resulting in a difficult identification of the sample components. Thus, a few soft ionization techniques were introduced and coupled with mass analyzers, in order to simplify the study of large biological molecules.

Among these techniques, such as Plasma Desorption and Electrospray Ionization, the studies of Karas *et al* [73] reported several advantages for the laser desorption of analyte molecules embedded in an absorbing matrix, including a lower degree of fragmentation and higher ionization efficiency. In their work, protonated amino acids were detected under certain laser irradiance, but an increase of this experimental parameter led to significant fragmentation of the molecules. Interestingly, the same ions were detected at significantly lower laser irradiance when these species were mixed with a different amino acid. Consequently, the term *Matrix-Assisted Laser Desorption* was introduced to present this result. Few years later, the same group presented the spectra of proteins mixed with an excess amount of the absorbing matrix [74] and dried on a supporting substrate, emphasizing the possibility to extend the application of this technique to larger molecules, obtaining high sensitivity and good spectral quality.

At the same time, these results led to the interest for the development of different absorbing matrices and simple sample preparation procedures. Indeed, Tanaka *et al.* [75] independently presented the spectrum of high-mass molecular ions with a simple procedure, employing an ultra fine cobalt powder as the matrix, further expanding the range of mass detection. This result was ascribed to a rapid heating of the sample promoted by the inorganic matrix, facilitating the vaporization, instead of decomposition of the analyte. Due to his contribution in the development of this technique and the successful detection of intact proteins molecules, he was later awarded with the Nobel Prize in Chemistry in 2002 [76]. A similar result was obtained ten years later with titanium nitride particles, suspended in glycerol [77]. Furthermore, Sunner *et al.* [78] suggested a surface desorption mechanism of proteins and peptides, assisted by large $(10-50\mu m)$ graphite particles. Thus, the name Surface Assisted Laser Desorption Ionization (SALDI) MS was firstly introduced in this work.

After decades of investigations, many phenomena, affecting the desorption and ionization of analyte molecules, have been studied but not fully understood yet. [79–81] This is mostly a consequence of the extremely complicated system.

More recent advances include nanoparticles in the sample preparation procedure, achieving significant improvements of MALDI MS [14] performance. The application of nanoparticles has several advantages. Firstly, nanoparticles can be employed to selectively concentrate the analyte of interest from an highly diluted solution, which is later mixed with a common organic matrix. Alternatively, these can replace absorbing matrix molecules and efficiently transfer the laser energy for the desorption and ionization of the analyte. Consequently, a large number of matrices based on nanostructures of different nature, i.e. metallic nanoparticles, metal oxides nanoparticles, carbon based nanomaterials and quanatum dots [82], have been introduced in the last few decades.

Moreover, predeposited nanoparticles, coated with analyte molecules, facilitate the preparation of homogeneously distributed samples, increasing the reproducibility of

the signal, compared with common matrices, for which "sweet spots" are commonly formed during the co-crystallization of the organic molecules and the analyte [14]. This characteristic is useful for the development of imaging mass spectroscopy, based on laser desorption/ionization. Indeed, silver nanoparticles embedded into a tissue of rat heart were successfully employed for the detection of lipids [15], meanwhile, due to a small background noise, commonly observed from the fragmentation of organic molecules in the low mass region, the spatial distribution of fatty acids in mouse liver and retinal samples were reproduced [16].

Similarly to the development of organic matrices, the application of nanoparticles mostly relies on an empirical investigation, which discusses the efficiency of the system in regards of the specific experiment. This approach is commonly employed since there are many phenomena, occurring simultaneously during the desorption and ionization of adsorbed analyte molecule and it is difficult to identify the predominant mechanism. It their review, Picca *et al.* [83] summarized a list of experimental studies, which evaluate the ion desorption efficiency of nanostructured materials related to different physicochemical properties. Heating, melting and photoabsorption are identified as main factors in the LDI process, however it is emphasized the needs for further investigation.

For instance, an extensive study of the ion desorption efficiency was carried by Ng *et al.* [84], in which different nanomaterials are compared in regards of several characteristic properties. According to their results, the authors suggest the development of SALDI substrates with high photoabsorption efficiency, weak binding interaction with the analyte and low melting temperature, in order to improve the detection sensitivity.

In this regard, nanoparticles modification has been proved as a possible beneficial mechanism for the detection of the analyte. Considering silver nanoparticles, Prysiazhnyi *et al.* [85] argued that the detection of small molecules is facilitated by the formation of metal ion-analyte adducts, during reaction occurring in the plume.

Indeed, The authors related the material release from silver clusters to the particle heating and the LSPR in a later study [26]. Moreover, it is concluded that size of nanoparticles and coverage of the substrate are key design parameters for the formation of adduct species, obtaining the best performance from small silver nanoparticles.

2.5   Synthesis of Nanoparticles

Nowadays research in nanomaterials field focuses on synthesis of nanoparticles (varying in a size scale from 1 up to 100 nm) utilizing diverse fabrication methods. Particular combinations of structural parameter of nanoparticles such as size, shape, composition and crystallinity, are required for different applications in order to successfully utilize the specific property and satisfy operational needs.

The aforementioned parameters of nanoparticles are controlled by choosing method of preparation. A large variety of fabrication procedures have been proposed and developed and are divided into two main categories. In top-down approaches nanoparticles are produced from bulk material (also referred as physical methods), whilst in bottom-up routes the nano-sized structures are built from atoms or molecules (via
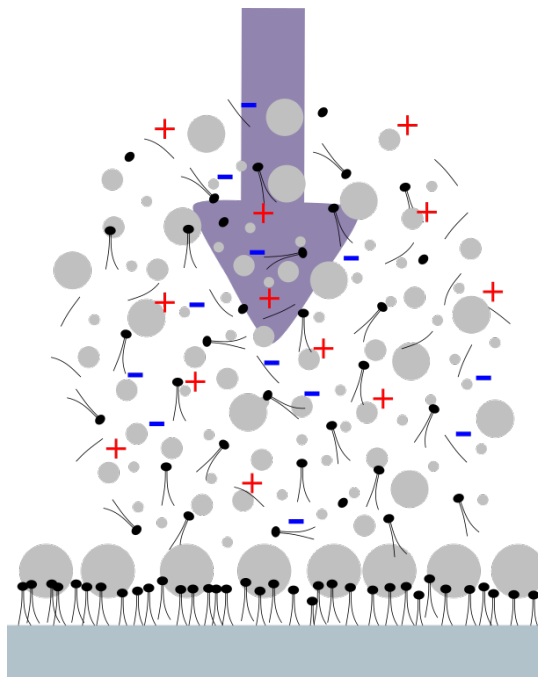
FIGURE 2.6: Schematic representation of MALDI MS process, where
the matrix with metalic nanoparticles, covering the analyte, is shown.
The formation of the plume, consisting of neutral and charged ana-
lyte and metal species, induced by laser irradiation (violet arrow), is
illustrated

chemical reactions). In this section, a few common physical and chemical synthe-
sis methods of metallic nanoparticles are presented, discussing their advantages and
drawbacks.

2.5.1 Chemical Methods

Wet Chemical Reduction

In chemical reduction-based synthesis of nanoparticles, the source of metal is ionic
salt which is reduced in aqueous solutions using reducing agents, such as sodium
borohydride, citrate [86] or hydrazine [87]. During reduction reaction, metal ions are
reduced to atoms which instantly agglomerate into particles with diameters of several
nanometres. For instance, silver nanoparticles are typically formed from silver nitrate,
as shown in a reaction with sodium borohydride [88]:

$$AgNO_3 + NaBH_4 \longrightarrow Ag + 0.5\,H_2 + 0.5\,B_2H_6 + NaNO_3$$
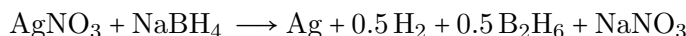
The size of particles can be controlled by choosing appropriate reductant: strong re-
ducing agents (such as borohydride) result in particles with narrow size distribution
while weaker ones (for instance, citrate) produce particles with broad range of di-
ameters. [88] The further growth of formed particles is prevented adding stabilizers,
for example, polyvinylpyrolidone (PVP) [86, 87, 89], polyethylene glycol (PEG) and
polymethylmethacrylate (PMMA) [88] or polyvinylalcohol (PVA) [89].

The chemical reduction method is widely used due to its simplicity and possibility to
synthesise small nanoparticles with a narrow size range. [90] The main drawback of
this approach is toxicity of reducing agents which are hazardous for human health,

such as sodium borohydride which may negatively impact the lungs if exposed, or hydrazine which is carcinogenic [89]. Thus, costly processes of removal dangerous substances from prepared nanoparticles is required.

Sol-Gel

Sol-gel processing is a versatile method for fabricating nanostructures of metal [91] or metal oxide [92] nanoparticles. The metal–organic route of sol-gel technique utilizes metal alkoxides as main precursors, dissolved in alcoholic solution. [93] The first key step of synthesis is hydrolysis where nucleophilic water attacks the metal atom and leads to the substitution of the alkoxide group (-OR) with the hydroxylgroups (-OH) [92], as shown in given chemical reaction below:

$$M-OR + HOH \rightleftharpoons M-OH + ROH$$
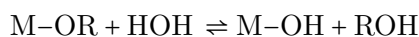
where M is metal, R - alkyl group (C_nH_{2n+1}).

Generally, acidic or basic catalyst is added for facilitating the hydrolysis reaction. The second step is polycondensation reactions where water and alcohol are eliminated building $M-O-M$ network [93]:

$$M-OH + MOH \rightleftharpoons M-O-M + HOH$$

$$M-OR + MOH \rightleftharpoons M-O-M + ROH$$
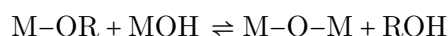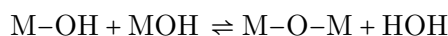
Polycondensation reaction, shown above, continues increasing the viscosity of the colloidal solution (sol) and its subsequent transition into the gel which is further dried during aging step. [92] Lastly, the thermal treatment is performed in order to remove the residues of water from the desired structure.

The method allows to efficiently control the composition, size and morphology of nanoparticles. [94] It can be used for preparation of various compounds but involves expensive precursors, it is time-consuming and has reproducibility issues thus is limited for application in industrial production. [89]

Flame Spray Pyrolysis

The flame spray pyrolysis process is synthesis method based on a gas phase combustion. The procedure of nanoparticles fabrication starts from atomization of a liquid precursor - metallorganic compound and a solvent. The liquid droplets of precursor mixture are formed with high pressure dispersion gas and gets ignited by the flame. The flame is fed by fuel (including oxygen), supplied through system of nozzles, and sustains the combustion of the precursor spray. In a hot reactor, the metallorganic compound decomposes, while supplied oxygen provides the complete combustion of organic parts into water vapour and carbon dioxide. From metallic parts of the precursor the primary particles are nucleated which further grow into larger clusters.

The size of the particles is determined by the particle residency time in high temperature region where primary particles aggregate into larger ones. This parameter can be controlled by varying oxygen flow rate [95] - increased amount of oxidant accelerate burning process of droplets. In this way, the length of spray flame is reduced and the growth region of particles becomes shorter, thus smaller particles are produced. The flame length can be also adjusted by changing configuration of nozzles for burning

gases [96]. Moreover, a cool air can be introduced into the system in order to limit the growth of particles via quenching. [97]

Generally oxidised particles are fabricated due to the oxygen presence in the flame pyrolysis process. Metallic nanoparticles are possible to synthesize using halide flames instead of hydrocarbon ones. This approach was utilized fabricating titanium nanoparticles, where metal chloride reacts with sodium vapour forming metallic particles, surrounded by sodium chloride shell. [98] NaCl coating was found to prevent from oxidation of titanium and to be easily removable by washing with water.

The flame spray pyrolysis method is successfully used for fabrication of high purity and multi-component particles with controlled sizes. For instance, doped metallic nanoparticles of $\sim 10\,nm$ were fabricated from Ag [99] and Ti [100]. Another advantage is possibility to deposit particles directly on the desired substrate [101]. The drawback of the method is high operating temperatures and subsequent quenching which might result in amorphous phases [102].

Chemical Vapor Deposition

Chemical vapour deposition (CVD) is a vapor-phase synthesis method, commonly used to form elemental or compound coatings and films [103], and recently customized for production of nanostructures. The synthesis procedure starts with introduction of vapor phase precursor into the reactor, together with carrier gases. Precursor molecules diffuse towards the substrate and are adsorbed on the surface where the nuclei of desired product are formed. The growth of the nuclei is followed by desorption of volatile byproducts which are removed out of the chamber together with unreacted species. It is possible to form nanoparticles and deposit them onto the substrate under the control of deposition conditions in the CVD reactor (selecting particular precursor type and flow, process time, temperature and pressure). [104]

The chemical vapour deposition method is attractive due to one-step synthesis of particles with controlled surface morphology and possibility to fabricate multi-component particles [105], various composites, enriched with metallic nanoparticles or nanostructures, coated with metal [104]. The drawbacks of this method are the high cost of the process and complex handling of hazardous precursors.

2.5.2 Physical Methods

Mechanical Ball Milling

The ball milling is method of particle size reduction where high mechanical energy is employed. During the synthesis process, the bulk powder is placed in the container together with several heavy balls, which roll down the surface of the milled material and transfer their kinetic energy into it. As a result, the bulk materials is cracked into smaller, nanodimensional particles having newly created surfaces. In order to avoid contamination, the milling chamber is sealed and filled with inert gases. Particular compounds are formed by introducing gases such hydrogen, nitrogen or air, producing hydrides, nitrides and oxides. [106]

Powder particles are reduced due to the internal strain induced during grinding. In another hand, freshly made particles strive to minimize their surface energy thus agglomerate into larger ones. To overcome the size increase, particles are synthesized in wet medium using surfactants. Depending on the nature of the material and surface charge characteristics, either cationic, anionic, zwitterionic or nonionic surfactants

are used. [106, 107] When adsorbed on the milling material surface, the molecules of active surface agents stabilize the particles and prevent them from uncontrolled cracking. Additionally, surfactants reduce the surface energy of particles and therefore minimize the agglomeration.

Surfactant assisted ball milling was successfully utilized fabricating Fe, Co, and FeCo NPs with average size of $6\,nm$ [108], and for Ag nanoparticles with sizes between 10 and $12\,nm$ [109] and from $14\,to\,34\,nm$ [110].

The mechanical ball milling nanoparticle synthesis route is inexpensive and can be used at room temperature but requires high energy consumption [89]. Another disadvantages are contamination of the product due to wear of mill balls and long process time. [111]

Gas-Phase Synthesis

In this project, the fabrication of nanoparticles is performed via gas-phase synthesis route. Gas aggregation methods are based on supersaturated vapor state, which is thermodynamically favorable for the molecules of the vapour phase to form a condensed phase under rapid cooling condition.

Nanoparticles are formed from a vapour excess of pure metal, sputtered of vaporized in vacuum, and collimated into the beam. This method allows to precisely control nanoparticles size, composition, and kinetic energy which defines either they are deposited or implanted to the substrate. [17, 112]

Vaporization Methods

Evaporation-Condensation

The simplest method of gas aggregation is based on heating of liquid or solid source placed in the furnace chamber until it evaporates. Then the source vapor is supersaturated by cooling in inert gas environment and is condensed, thus clusters nucleation and growth are facilitated. Similar process occurs in nature during the formation of fog and clouds. The evaporation method is suitable to produce metallic clusters such as silver particles in a sizes range from $9\,to\,60\,nm$. [113, 114] The sizes of produced particles can be controlled by varying inert gas flow rate and adjusting its pressure or process temperature. [114] The cold inert gas stream can be mixed with reactive gases, for instance, oxygen, thus oxide (or other compounds) of evaporated source material can be formed. [105]

The method has drawbacks of expensive equipment, high energy consumption. [89]

Supersonic Expansion

The supersonic expansion method utilizes adiabatic gas cooling to form clusters. The gas is expanded through the nozzle (diameter size ranges in micrometre scale) from source region with a high pressure to the low pressure region sustaining supersonic expansion and intense beam of clusters is formed which is further collimated with a skimmer. [112] For production of metallic nanoparticles, the seeded source is used in which vaporized metal is mixed with inert gas, which facilitates the cluster formation by adsorbing the heat of condensation. [115] The size of the produced nanoparticles can be tuned by changing temperature of the nozzle or varying pressure in source chamber. [112] Moreover, a choice of lighter inert gas (for instance, helium rather than argon) results in smaller product particles as cluster flow is faster and growth time is shorter.[115, 116]

The supersonic expansion successfully applied to fabricate metallic film consisting of $6\,nm$ silver particles [117], and multi-component coating of Al and Ti nanoparticles. [116]

Laser Ablation

Pulsed laser ablation is fabrication method where nanoparticles are formed directly from a bulk target. Powerful short laser pulses irradiates and vaporizes the desired material leading to the formation of the laser plume, consisting of individual atoms or molecules and small clusters. It acts as a source of nanoparticles, directly deposited on the substrate.

The laser ablation process can be conducted in a vacuum, gas environment or in a liquid. Particularly, the laser fabrication of nanoparticles in liquids forming colloidal solution is preferable due to relatively simple instrumentation (compared to the systems with vacuum chamber), which includes a pulsed laser, focusing optics, and a target, placed in a container with liquid. [118]

Sizes of nanoparticles can be controlled by varying laser parameters such as wavelength, energy density (fluence), pulse duration and repetition rate [118, 119] or concentration and nature of the solvent if ablating in aqueous medium approach is applied (Ag NPs [119], Cu NPs [120, 121], Au NPs [122]).

The preparation of nanoparticles can be improved by shortening the pulse duration from nanoseconds (ns) to picoseconds (ps) or even femtoseconds (fs), the heat affected zone decreases therefore less micron-sized particles are ejected due to minimization of thermal diffusion in the target material. [118]

Possibility to produce small-sized particles from different materials including various metals, without altering chemical composition, makes the laser ablation an attractive tool for clean and fast nanoparticle synthesis. Nevertheless, the method is unsuitable for productive large-scale fabrication and has disadvantage of high energy consumption. [118]

Sputtering Methods

Arc Discharge

Another method of formation of nanoparticles from vapor of metals is arc discharge method which utilizes electric discharge to sputter the material. A large electric current is run for a short time through two metal electrodes resulting in ignition of electric discharge between anode and cathode. Electrodes are usually made from metal of production interest and serve as a source of vapor which subsequently condenses forming metal particles.

Metal electrodes can be made of inert metal (for instance, titanium) and immersed in liquid solution with metallic precursor (such as $AgNO_3$ in deionized water). [123] During electric discharge event, electron exchange occurs in plasma region and silver ions are reduced.

The arc discharge method offers high production rates of metallic particles with relatively simple equipment and few step procedure and low contamination. The disadvantage of the method is large size distribution of synthesized nanoparticles. [89]

Magnetron-Based Cluster Synthesis

In this work, metallic nanoparticles are produced by cluster beam deposition technique using magnetron sputtering cluster apparatus (MaSCA, Fig. 3.1) where metal target is vaporized due to bombarding with high energy argon ions using magnetically confined plasma. Sputtered metal atoms start to form clusters in the aggregation chamber with the help of cooled helium, acting as a buffer gas. Two individual sputtered metal atoms nucleate into a small cluster, and the excess of energy is released due to the binding. Under the collision with helium atom the emergent dimer stabilizes because the inert gas carries away the energy excess.

Large fraction of the clusters, produced by magnetron sputtering, are ionized and widely distributed in mass [124]. Thus, before deposition on the sample, the particles in the cluster beam can be filtered by size and charge employing electric field in electrostatic quadrupole mass selector [17].

The beam intensity and size of the clusters can be tuned by proper combination of process parameters: increased magnetron power changes density of plasma thus increase the number of sputtered source atoms; extended length of aggregation region leads to longer time for particle growth. Magnetron- based gas-phase synthesis ensure high atomic density of metallic clusters, arranged in symmetric polyhedral-shapes, described by Wulff constructions. [125] It results in high coordination number of surface atoms therefore a great chemical inertness of produced nanoparticles. Another advantages are high purity of fabricated particles due to high vacuum synthesis and high production rates. The main drawback of the method is limited cluster beam stability. [126]

2.6   Metal oxidation: The Case of Copper

The performance of devices based on metallic nanostructures is strongly dependent on the interaction between the metal surface and the surrounding environment because of the reactions occurring when exposed to ambient air at room temperature. Consequently, gold is usually preferred to silver as it owns a higher stability. Indeed,

the latter one is prone to react in ambient condition with sulfur compounds, to form silver sulfide, Ag_2S [127].

Moreover, the larger surface to volume ratio of metal nanostructures compared with thin films, increases the rate of reaction, determining a change in the chemical composition and morphology of the structure over a relatively short time period [127, 128], and consequently strongly affecting the properties of the nanostructure, which has to be considered as a limit for successful applications.

Similarly copper is known for the formation of stable oxides when exposed to ambient condition and the oxidation process have been intensively studied. A review over the most recent research aimig to explain the atomistic mechanism of copper oxide formation and the outcome related with different ambient condition are given by Gattinoni *et al.* [129], describing the initial dissociative adsorption of oxygen on the surface of pure copper and the subsequent nucleation and coalesence of nano-island.

In spite of the results produced by the studies on the oxidation process during the last century, focusing mostly on thin films and bulk copper, a precise explanation for the mechanism of the interaction between oxygen and copper nanostructure is not completely developed. The reduced dimension of copper nanostructures, compared with microstructures, increases further the reactivity with the oxygen molecules in the surrounding environment, because of the large surface to volume ratio [130]. The formation of an oxide layer on the nanoscale copper surface have been proved experimentally. Kim *et al.* [131] produced $100 - 140\,nm$ diameter copper spheres on silicon substrate using hydrogen-free spray pyrolysis together with electrostatic percipitator and kept it exposed to ambient laboratory conditions. The results from TEM images show the formation of a thin oxide coating immediately after the synthesis. The oxide layer was measured to grow approximately linearly over a period of one year, forming a crystalline Cu_2O shell surrounding the particle, as observed by X-ray diffraction (XRD) measurements.

The morphology of smaller copper nanoparticles, around $25\,nm$, exposed to ambient condition for a period of three months, where studied with TEM imaging by Boyd *et al.* [19]. The images obtained from both samples present a copper core - oxide shell structure, where the oxide shell consists of an inner Cu_2O phase and outer CuO phase.

Real time *in situ* studies of oxidizing copper nanoparticles had been presented by LaGrow *et al.* [20] They produced nanoparticle in a wide range of size, ~ 6 to $80\,nm$, by sputtering copper target and further reduced with hydrogen prior oxidation experiments. Opposite to aforementioned experiments, here particles were oxidized at elevated temperatures (300°C and 500°C) in order to accelerate the oxidation and observe the phase change of the single particles. The oxygen at $2\,Pa$ pressure was supplied to the sample and at regular time intervals TEM images were obtained. Intensity differences of captured particles showed nucleation event of oxide on one point of the copper particle in the beginning and further unidirectional growth across the particle until single phase of cuprous oxide was reached. The observed oxidation manner was found to be independent of particle size, support material (carbon and silicon nitride was compared), temperature and pressure - only oxidation rate was increasing at higher temperatures (from 300°C to 500°C) and pressures (from 2 to 5 and $10\,Pa$).

Even though the controlled formation of an oxide shell can be advantageous for some application, such as the photocatalytic degradation of organic and inorganic dye molecules [132, 133], the spontaneous oxidation of copper in ambient condition, is considered as the main limitation to for the applicability of copper-based plasmonic nanostructures. The growth of an oxide layer is responsible for the attenuation of the plasmonic property, which has to be taken into consideration in order to guarantee the performances of copper based devices through the storing period, before the actual use. In the last decade, many studies aimed to develop a protective outer layer to prevent the native oxidation. Some solutions which have been proposed include the covering of Cu-based nanostructures with copper formate [24], organic ligands [134] and Cu-Au core-shell particles [135]. Recently, Popok *et al.* [25] proposed an easy and less expensive procedure for the fabrication of monocristalline high purity copper nanoparticle which include the controlled growth of a thin protective oxide layer, aiming to prevent further oxide formation and, consequently, extend the stability of the plasmonic property.

2.6.1 Oxidation of Copper Nanoparticles. Effect on LSPR

Different studies approached the oxidation problem by observing the time evolution of the LSPR. According to Eq. (2.3), the extinction cross section is affected by different parameters, including the dielectric properties of the surrounding environment. As an example, in the case of supported nanoparticles, the presence of an isolating substrate changes the properties of the plasmonic peak when compared with a particle suspended in an homogeneous dielectric, such as oil or water [136].

Similarly, the formation of a copper oxide phase will affect the intensity and the wavelength of the plasmonic peak, until the complete oxidation of the pure copper particle with the consequent disappearing of the plasmonic character. This behaviour was related to the thickness of the oxide shell by Ghodselai *et al.* [137], in good agreement with the prediction derived by Mie theory. Later on, Rice *et al.* [21, 22] experimentally studied the mechanism of oxidation for chemically synthesized copper nanoparticles by in-situ optical spectroscopy. In both studies, they reported an attenuation of the plasmonic peak after the formation of the oxide phase surrounding the particle and they observed the occurring of a pure copper-copper oxide core-shell structure by TEM. The intensity of the plasmonic peak decreased drastically until the complete oxidation of the sample, corresponding to the disappearing of the copper core. This tendency is in agreement with analytical predictions based on Mie Theory, for which the formation of the oxide shell causes the increase in the intensity of the plasmonic peak and its red shift. Accordingly, the optimal ratio between oxide shell thickness and particle size allows to avoid the interference related with interband transitions [138], and consequently, to improve the plasmonic properties of pure copper particles.

More recently, Nilsson *et al.* [139] replicate the results obtained from Rice *et al.*, considering a single disk-shaped nanostructure and presented an electrodynamic simulation which replicates the experimental results considering the morphological changes of the copper structure related with an initial growth of the outer oxide shell and simultaneous disappearing of the core copper. It has to be noted, that they assumed the formation of an internal void, due to the nano Kirkendall effect. However, this phenomena seems to occur only for oxidation process at temperature higher than 150°. Consequently, this phenomena is not investigated in this report.

Chapter 3

Instrumentation, experimental and analysis methods

3.1 Formation and Deposition of Nanoparticles

Gas-phase synthesis of metallic nanoparticles was performed using system called magnetron sputtering cluster apparatus, MaSCA (Fig. 3.1, detailed description of the machinery can be found in [17]). The commercial source containing magnetron creates a plasma with sputtered metal atoms which are aggregated into clusters with the help of helium gas and further collimated into a beam. The formation is processed under high vacuum conditions using turbomolecular pumps and fore-vacuum pumps (all from Pheiffer Vacuum, Germany).
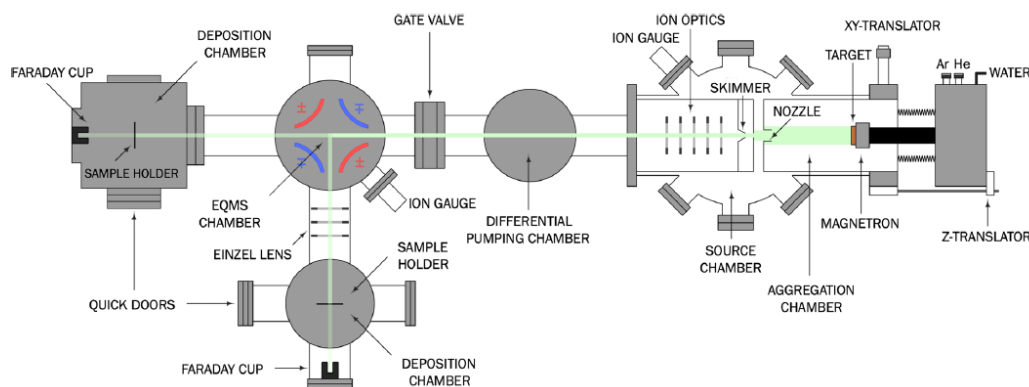

FIGURE 3.1: The schematic of MaSCA. Adopted from [124] with a permission of Springer Nature

More than a half of the particles, produced by magnetron sputtering, are ionized and distributed in a wide interval of sizes. [124] Therefore, the electrostatic quadrupole mass selector (EQMS) is placed in the beam path to filter the clusters, prior the deposition. There is also a possibility to perform straight deposition where formed clusters are deposited directly onto the sample without mass and charge selection.

Size selection is performed by electric fields which allows to filter charged nanoparticles. The EQMS is consisted of four electrodes, constructed in hyperbolic shape and surrounded by a grounded shield, with circular openings for the beam of clusters. [17] The electrodes can be biased in pairs of opposite polarities and equal magnitudes of voltages generating hyperbolic equipotential field which deflects charged particles with negative or positive electric charge by 90° to the deposition chamber.

The mass-selection is implemented satisfying the condition that the electrostatic field energy balances the kinetic energy of the deflected particle, valid for the relation:

$$\frac{m}{q} = \frac{2U}{v^2} \qquad (3.1)$$

where m and q is mass and charge of the particle, respectively, U is potential, applied to electrodes, and v is velocity of the particles (assumed to be the same for all incoming particles).

Considering that clusters pass through the filtering with the same velocities, mass-to-charge ratio is proportional to the potential applied to EQMS electrodes:

$$\frac{m}{q} \sim U \qquad (3.2)$$

The Faraday cup is placed in the deposition chamber to the density of the charged clusters beam by measuring the current:

$$\frac{N}{t} = \frac{I}{e} \qquad (3.3)$$

where the number of charged particles captured per second is equal to the electric current per elementary charge.

In the current work, metallic nanoparticles were deposited in two different ways. In the first case, no potential was applied to electrodes of mass selector($V_{EQMS} = 0\,V$) and nanoparticles of all sizes, produced in the aggregation chamber, were steered straight onto the substrate (see Fig. 3.1). In the second case, certain values of potential were applied to EQMS and nanoparticles of particular mass-to-charge ratio (as discussed above) were deflected by $90°$ and deposited onto a substrate in the other chamber (see Fig. 3.1). The details about mass filtering voltages are given below, in the descriptions of samples used for every study method.

Typical background pressure in the source chamber was $(3-9) \times 10^{-8}\,mbar$, which increased up $2-3 \times 10^{-3}\,mbar$ under the magnetron operation. In the deposition chamber, the background pressure was $(1-6) \times 10^{-7}\,mbar$, increased to $(5-6) \times 10^{-6}\,mbar$ during the cluster deposition. Copper nanoparticles were deposited using gas flows of argon and helium at $72-78\,sccm$ and $10-30\,sccm$, respectively. For production of silver nanoparticles, argon flow of $76-84\,sccm$ and helium flow of $7-38\,sccm$ were kept. Typical operating values of magnetron power were set to $70-85\,W$ for fabrication of silver, and $70-100\,W$ for copper nanoparticles.

UV-Ozone Treatment

Several quartz substrates with deposited copper nanoparticles were treated in UV-ozone environment after the deposition.

The ultraviolet-ozone cleaning apparatus was employed to form protective copper oxide layer [140] on Cu nanoparticles, immediately after samples with particles were taken out of deposition chamber. Previous studies with XPS had revealed direct

copper oxidation to cupric oxide phase after ozone treatment of Cu foils [140] and Cu nanoparticles [25].

The set-up of UV-ozone treatment consists of two lamps, emitting ultraviolet $184.9\,nm$ and $253.7\,nm$ light which irradiates atmospheric oxygen.

Under illumination with ultraviolet rays, oxygen molecules absorb the $184.9\,nm$ light and form ozone via following reactions:

$$O_2 \longrightarrow O + O$$

$$O + O_2 \longrightarrow O_3$$
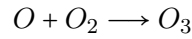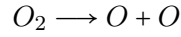
Meanwhile, ozone decomposes when irradiated with $252.7\,nm$ ultraviolet light.

Both processes generate atomic oxygen which is strong oxidising agent.

3.2 Atomic Force Microscopy

Samples of silicon substrates, covered by silver and copper nanoparticles, were produced for size analysis by AFM. Different samples were produced applying V_{EQMS} = 0, 700, 1300 V for deposition of copper, and, V_{EQMS} = 200, 500, 1100, 1700 V for silver nanoparticles. Deposition time was kept short in order to fabricate samples with low nanoparticle coverage (less than 1 monolayer).

Scanning Probe Microscope NTEGRA Aura (NT-MDT) was used to measure surface topography of samples by atomic forces. Standard silicon cantilevers with tip curvature radius smaller than $10\,nm$ were used, tapping mode was selected for the measurements.

Evaluation of nanoparticle sizes was performed in Image Analysis software using Advanced Watershed module. This option allows to collect data of maximum heights from automatically detected grains (particles). However, only isolated single nano particles were considered, in order to disregard wrong measurements related with poor quality of the image, possible impurities on the substrate surface and stacks of few nanoparticles.

Previous studies had demonstrated that clusters, produced by MaSCA, are tend to preserve nearly spherical shape [112]. Therefore, heights of nanoparticles, measured by AFM, are approximately equal to the diameter ($h_{cluster} \approx d_{cluster}$).

3.3 X-ray Photoelectron Spectroscopy

Composition of copper nanoparticles was analyzed by X-ray photoelectron spectroscopy (XPS) together with Auger Electron Spectroscopy (AES). The measurements were performed repeatedly during the period of 2.5 months in order to study spectral changes related to copper oxidation.

For the analysis, a set of two silicon substrates, covered by copper nanoparticles, were used. Nanoparticles were filtered at V_{EQMS} = 700 V prior deposition. One sample was measured immediately after deposition. Another one was treated in ozone environment for 20 minutes immediately after deposition of nanoparticles and stored in N$_2$ atmosphere in order to prevent further interactions with atmospheric oxygen,

until the first measurement, performed after a week (indicated as day 8). Both samples were kept in ambient laboratory conditions and room temperature between the measurements.

Spectroscopy measurements were carried out using a system from SPECS equipped with Phoibos 150 hemispherical analyser, one-dimensional delay-line detector and monochromatic X-ray source. The spectra were recorded with Al X-rays ($1486.6\,eV$) at a fixed pass energy of 50 eV in the analyser ensuring a high transmission and providing a sensitivity for identification of small spectral shifts of the peaks of interest, $Cu2p_{3/2}$, $Cu2p_{1/2}$ and satellites as well as Cu and Cu oxide Auger electron peaks. The measurements were carried out in ultra-high vacuum conditions (pressure lower than $2{\times}10^{-9}\,mbar$) on the samples with as-deposited copper nanoparticles and those treated in UV-ozone environment.

3.4   Optical Spectrometry

The optical spectrophotometer Lambda 1050 UV/VIS/NIR (Perkin Elmer, United States) was employed to measure the relative extinction spectra of nanoparticles.

Several samples with size-selected copper (V_{EQMS} = 700, $1300\,V$) and silver (V_{EQMS} = 200, 500, 1100, $1700\,V$) nanoparticles, deposited on quartz substrates, were analyzed. In a case of copper, two samples with each size of nanoparticles were produced. One of them was kept in ambient laboratory conditions, the other one was UV/ozone treated immediately after the deposition and then kept in the same ambient conditions.

The wavelength range of $\lambda = 350 - 800\,nm$ was used in optical measurements, for samples with copper nanoparticles and $\lambda = 320 - 750\,nm$ for the samples, covered by silver nanoparticles.

The measurement requires to individually collect the transmission spectra of the samples and bare quartz substrates in order to obtain relative extinction of the metal particles only. Therefore, the following formula was used to calculate relative extinction of metallic nanoparticles, $E_{nanoparticles}$:

$$E_{nanoparticles} = (100\% - T_{nanoparticles+q}) - (100\% - T_q) \tag{3.4}$$

where $T_{nanoparticles+q}$ is the transmittance of samples with metal nanoparticles and T_q is the transmittance of bare quartz substrate.

3.5   Surface Enhanced Raman Spectroscopy

The Raman spectroscope inVia (Renishaw, United Kingdom) was used to examine methylene blue (MB) molecules on the silicon substrates (with deposited nanoparticles and without) evaluating the LSPR contribution to the intensity change of Raman scattered light. The laser light of $532\,nm$ was used as an excitation source.

Sample preparation

Silicon substrates were covered with size-selected copper and silver nanoparticles. Copper nanoparticles were filtered at V_{EQMS} = 700, $1300\,V$ meanwhile silver nanoparticles were deposited applying V_{EQMS} = 500, 1100, $1300\,V$. Simultaneously, the coverage of the substrate was controlled by adjustments of the deposition time in relation to the measured current of the cluster beam.

Methylene blue is chose as the probe molecule for these experiments. Methylene blue powder was purchased from Sigma-Aldrich and the proper amount was mixed with milliQ water in order to prepare a stock solution with concentration of $1mM$. Subsequently, volumes of $1\mu M$, $0.1\mu M$ and $0.01\mu M$ methylene blue aqueous solution were prepared by dilution steps. Droplet with volume of $0.1mL$, from these solutions, were poured on the surface of the substrate. The samples covered with a droplet were placed inside a vacuum drier in order to facilitate the evaporation of the water content and let the methylene blue molecules to deposit on the surface of the substrate.

The methylene blue concentration $c_{MB} = 1mM$ was used for Normal Raman measurements on bare silicon substrate. For SERS measurements, both silver and copper nanoparticle substrates were covered with $c_{MB} = 1mM$, while droplet of $1\mu M$, $0.1\mu M$ and $0.01\mu M$ analyte solution were dried only on silver SERS substrates.

SERS procedure

Conventional Raman scattering spectroscopy was performed on different spots, approximately in the central area of the substrate where most of the nanoparticles are deposited. The excitation source, the corresponding power of $0.225\,W$ (0.5% of total laser power), exposure time, $5\,s$, and number of acquisition, 50, are maintained unchanged for each measurement.

Enhancement Factor Evaluation

The enhancement factor (EF) of Raman Scattering signal was evaluated according Eq. (3.5) at two distinct peaks: $\sim 1400\,cm^{-1}$ and $\sim 1600\,cm^{-1}$, corresponding to characteristic vibrational modes of methylene blue molecules.

$$EF = \frac{I_{SERS}/c_{SERS}}{I_{NR}/c_{NR}} \tag{3.5}$$

here I_{SERS} and I_{NR} are Raman Scattering intensity (measured in counts) at SERS and Normal Raman conditions, c_{SERS} and c_{NR} are analyte concentrations at SERS and Normal Raman conditions.

This parameter was evaluated considering the higher signal obtained in the set of measurements performed on each sample.

3.6 Matrix-assisted Laser Desorption Ionization Mass Spectroscopy

Two types of matrices with silver and copper nanoparticles were tested for MALDI analysis of biological samples.

MALDI experiments where performed at Masaryk University, Czech Republic, according the procedure, described below.

Analyte preparation

The model samples were pig brain homogenized tissue and natural beeswax. Both were purchased in local stores, ensuring the pig brain was fresh. Then, the as received pig brain was manually homogenized, followed by PYREX® Dounce tissue grinder. The homogenized mass was frozen at −80°C. The beeswax was cut into small cubes with $1\,cm$ lateral size. The substrates were Si wafers cut into $12\,mm \times 12\,mm$ pieces

and washed with pure methanol. The tissue slicing was done under $-20°C$ using Leica CM1950 microtome. The cut thickness was $20\,\mu m$ for both sample types.

Matrix fabrication

Copper matrices were prepared depositing copper nanoparticles directly on samples with homogenized tissue by MaSCA without size selection. Sample coverage by Cu nanoparticles was estimated to be ~ 1 monolayer.

Silver matrices were made by depositing gas aggregated Ag nanoparticles on top of samples with biological analyte. Silver particles were size-selected at filtering voltages of V_{EQMS} = 500, 1100, 1700 V.

Before and after deposition of nanoparticles, samples were stored below room temperature in order to preserve the molecular composition of biological tissues (mostly prevent degradation through oxidation).

Moreover, a matrix of thin copper thin was produced for comparison with copper nanoparticle matrices. Thin copper film was deposited on silicon using magnetron sputtering technique. The deposition was done using $3\,in$ water cooled magnetron gun (TORUS from Kurt J. Lesker) equipped with 99.99% copper target. The process was carried at 1.5 Pa pressure in argon atmosphere and using $150\,W$ DC source. The thickness of thin copper film was $8\,nm$ (determined by optical ellipsometry).

Mass spectra acquisition

The mass spectra were acquired using ultrahigh resolution mass spectrometer with orbital electrode (QExactive Plus from ThermoFisher Scientific). The ion source was sub-atmospheric pressure (sub-AP) source SubAP/MALDI(ng) from MassTech equipped with Nd:YAG laser operated at $1\,kHz$ frequency. Third harmonic of the laser at $355\,nm$ was used. The MS experiments were carried out at $1-12\,mTorr$ pressure in N_2, positive ion extraction for copper nanoparticles matrices, positive and negative for silver nanoparticles matrices, mass range from 50 to $1200\,Da$, mass resolution 140000 at m/z = 200, and laser shooting in constant speed rastering mode with $3.4\,mm/s$ with ion accumulation time $1\,s$.

3.6.1   Laser Irradiation of Silver Nanoparticles

The purpose of this experiment is to study the effects of laser irradiation in MALDI, on silver nanoparticles. Thus, six squared frames were scratched on the surface of a silicon substrate, before the deposition, across the entire surface, of nanoparticles size selected at V_{EQMS} = 1100 V. This procedure allows to easily identify different areas of the substrate. Each frame was irradiated along horizontal lines, separated by a step of $20\,\mu m$, with a beam of the same laser as used in MALDI experiments (see Section 3.6). The power of the laser is changed in each frame, and it is presented in arbitrary units (LE = 5, 30 and 50), according to its relative increase. A schematic of the sample is given in Fig. 3.2, indicating the scratched frames (black squares) which are irradiated with different energy values of the laser beam (blue lines), after the deposition of silver nanoparticles (gray dots).

The scanned frames were initially investigated by scanning electron microscope (SEM), in order to evaluate the effects of the laser irradiation and roughly estimate changes of the nanoparticles coverage, inside and outside the irradiated lines.
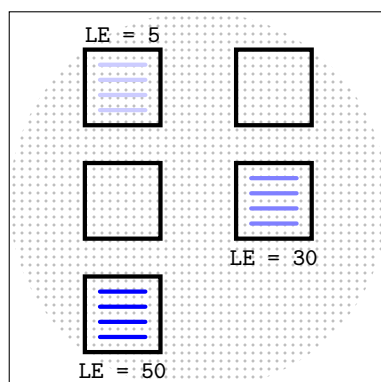
FIGURE 3.2: Schematic of the sample, showing the scratched frames with the irradiated lines. The different energy of the laser is reproduced by the intensity of the color

This experiment was combined with AFM images, inside the scanned frames, which allowed to further analyze the modification of nanoparticles morphology after laser irradiation.

Chapter 4

Results

4.1 Evaluation of Nanoparticle Sizes

The topography of the samples covered with copper or silver nanoparticles was analysed by AFM in order to evaluate the size distributions of nanoparticles selected with different voltages applied to the EQMS. Two examples of images are presented in Fig. 4.1. Earlier investigations showed that deposited Cu and Ag NPs preserve almost spherical shape, they slightly oblate in vertical direction [17, 141] Therefore, the measured height is considered to be approximately equal to the diameter and it is referred as the size of the nanoparticle.

The mean size of the nanoparticles, filtered at different voltages, is obtained from several images taken in different areas of each sample, in order to get sufficient statistics. The data are collected from three samples with copper nanoparticles and four samples with silver nanoparticles, deposited with different parameters of mass selection. In the first set of samples, copper nanoparticles filtered at $V_{EQMS} = 0, 700, 1300\,V$ are considered and the corresponding size distributions are illustrated in the histograms of Fig. 4.2. Similarly, the mean height of silver nanoparticles, deposited applying $V_{EQMS} = 500, 1100, 1700\,V$, is found from the histograms in Fig. 4.3. It is important to notice that nanoparticles located in close proximity or other strange features of the sample morphology have been neglected, thus, only isolated nanoparticles, highlighted with white circles in Fig. 4.1a and Fig. 4.1b were considered for the analysis in order obtain an accurate estimation of the nanoparticle size distribution.

The size distribution of nanoparticles, formed in the aggregation chamber and deposited straight without applying potential to EQMS, was identified with a lognormal distribution according to [142]:

$$f_{LN} = \exp\{-\ln^2(h/h_0)/(2\ln(2\sigma))\} \tag{4.1}$$

where h and h_0 are the measured height and the most frequent value, respectively, and σ is the shape parameter. This distribution is reproduced in the histogram obtained from the data relative to non-filtered nanoparticles (red line in Fig. 4.2a). Thus, the mean value extrapolated from the fitting curve is $h_0 = 17.5 \pm 5.1\,nm$. Meanwhile, a precise procedure for the study of the distribution of size-selected silver nanoparticles was proposed by Popok and Gurevich [124], considering the possible formation of multiply charged particles as previously suggested by Marom *et al.* [143].

Thus, the mean height of each sample is associated with a Gaussian curve centered at the most frequent value. The presence of multiple charged nanoparticles in the cluster beam, results in the appearance of larger masses and, respectively, larger sizes,
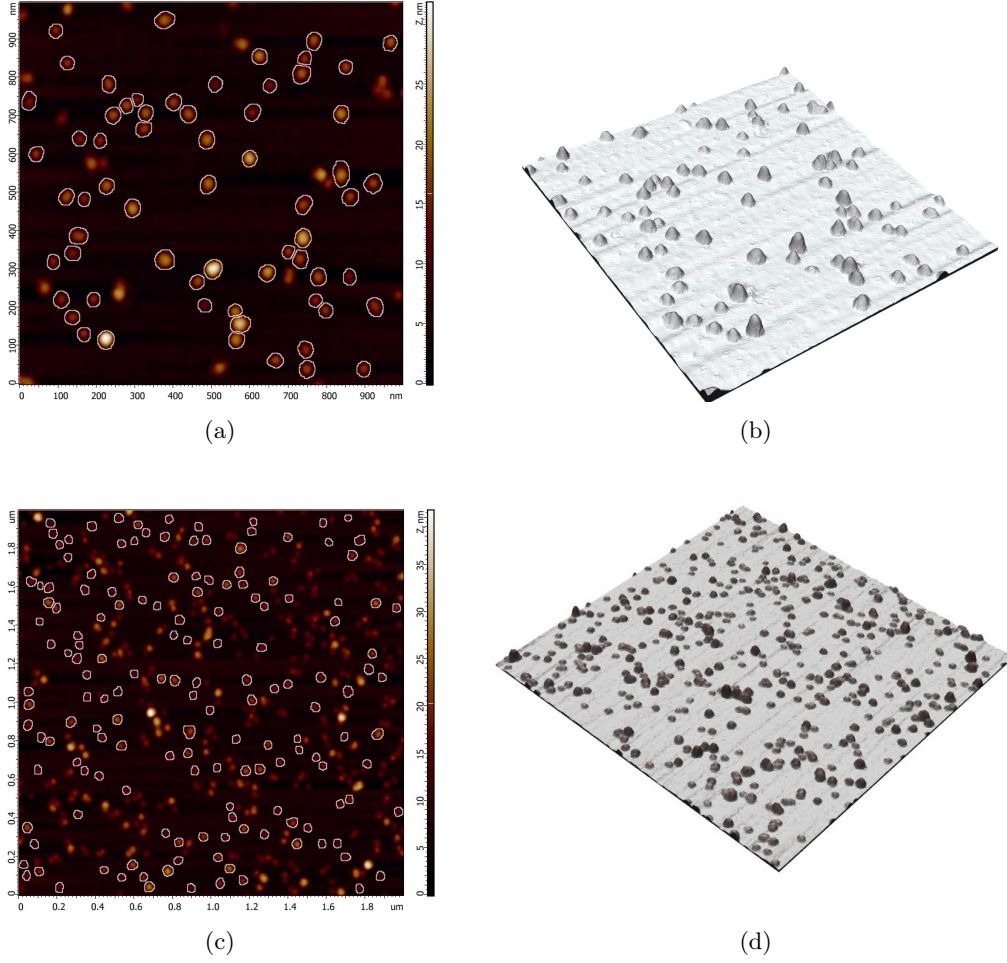
(a)   (b)

(c)   (d)

FIGURE 4.1: AFM images of a-b) silver nanoparticles and c-d) copper nanoparticles in 2D and 3D. The circles indicate nanoparticles selected for analysis

such as to satisfy the condition of a constant mass to charge ratio, given in Eq. (3.2). Thus, assuming the density independent of the cluster size, the height of multiple charged particles will also be increased proportionally to the cubic root of the number of charges n, according to $d = h_s \sqrt[3]{n}$, where h_s is the mean height of singly charged nanoparticle. Consequently, the size distribution of multiple charged nanoparticles is described by Gaussian curves and it is shown in each histogram, together with the total distribution, represented by the sum of Gaussian curves for singly and multiply charged nanoparticles.
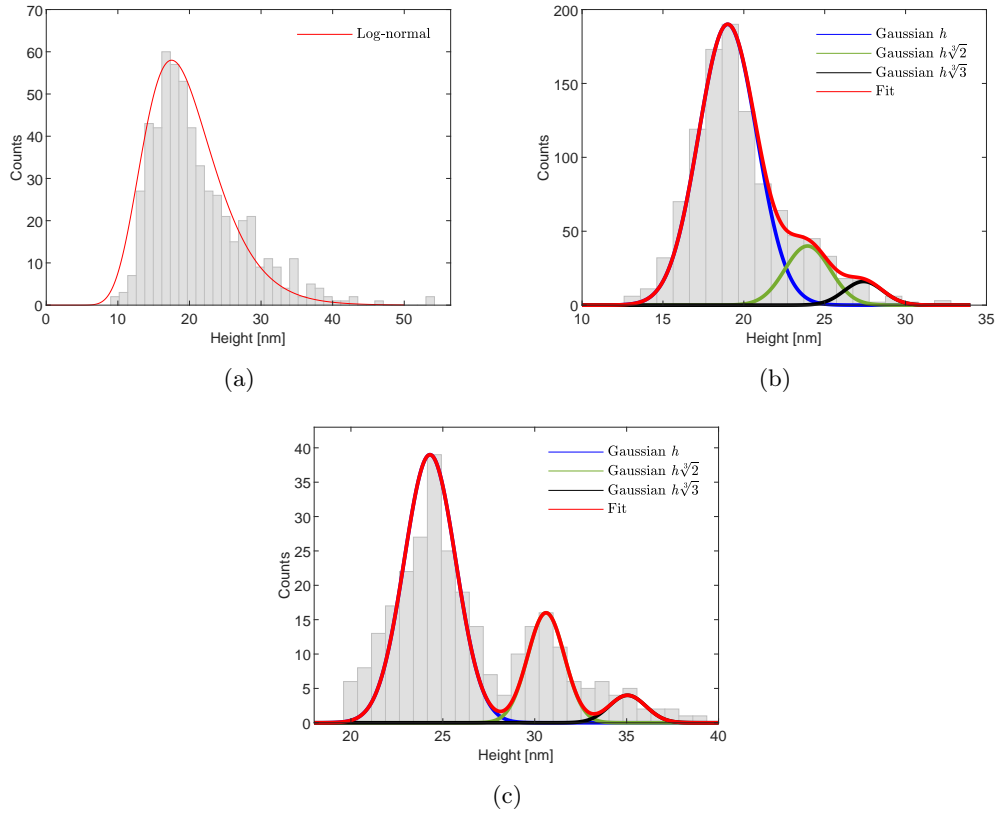
(a)

(b)

(c)

FIGURE 4.2: Size distribution of Cu NPs filtered at a) $V_{EQMS} = 0V$,
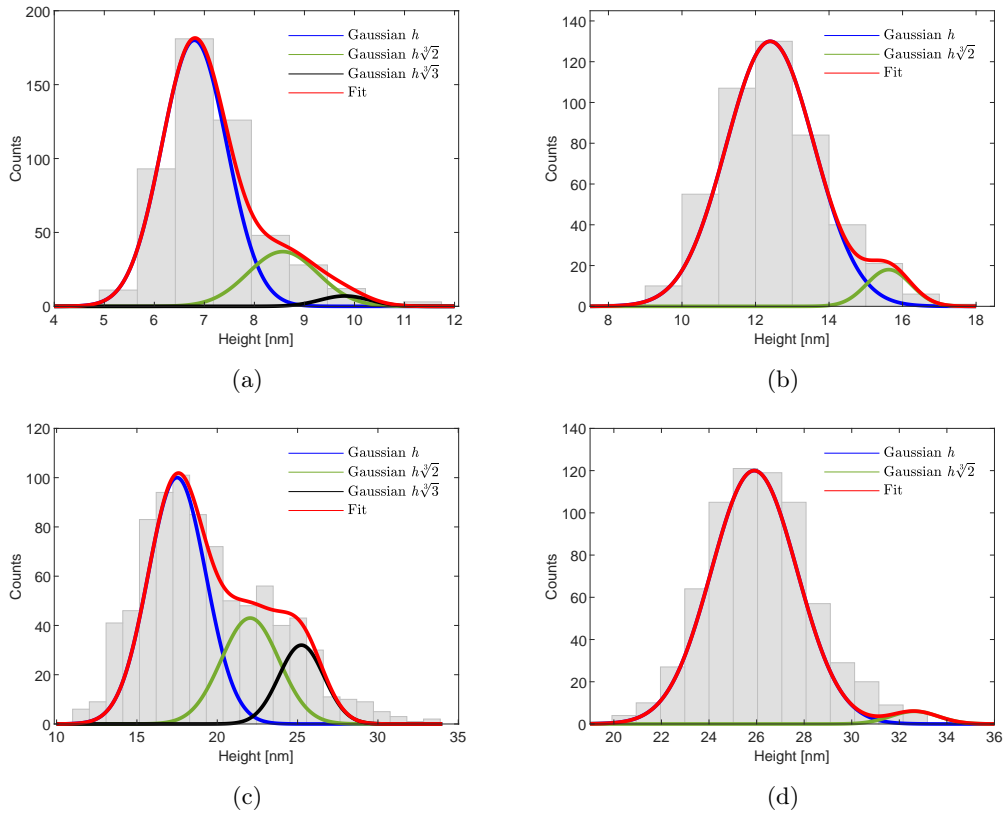b) $V_{EQMS} = 700V$ and c) $V_{EQMS} = 1300V$

(a)

(b)

(c)

(d)

FIGURE 4.3: Size distribution of Ag NPs filtered at a) $V_{EQMS} = 200V$,
b) $V_{EQMS} = 500V$, c) $V_{EQMS} = 1100V$ and d) $V_{EQMS} = 1700V$

As one can see from the histograms presented in Fig. 4.2 and Fig. 4.3, singly charged particles represent the majority in the beam. They are considered to be the "main" sizes filtered under given potentials. According to this procedure, the mean height of singly-charged copper nanoparticles filtered at $V_{EQMS} = 700\,V$ and $V_{EQMS} = 1300\,V$ are $h = 19 \pm 2\,nm$ and $h = 24.3 \pm 1.4\,nm$, respectively. Meanwhile, the values extrapolated for silver nanoparticles filtered at $V_{EQMS} = 200, 500, 1100\,V$ and $V_{EQMS} = 1700\,V$ are $h = 6.8 \pm 0.7\,nm, 12.4 \pm 1.2nm, 17.5 \pm 1.8$ and $h = 25.9 \pm 2nm$, respectively. These values have been summarized in Table 4.1, together with the number of nanoparticles analyzed (3rd column) and the ratio of multiple charge nanoparticles to single charge nanoparticles (5th and 6th columns).

TABLE 4.1: Size distribution of Cu and Ag nanoparticles filtered at different voltages

Material	V_{EQMS}	# NP	h Single	Double/Single	Triple/Single
Cu	0V	563	-	-	-
	700V	1051	19 ± 2	0.21	0.08
	1300V	286	24.3 ± 1.4	0.41	0.1
Ag	200V	503	6.8 ± 0.7	0.2	0.06
	500V	455	12.4 ± 1.2	0.14	-
	1100V	845	17.5 ± 1.8	0.43	0.32
	1700V	677	25.9 ± 2	0.05	-

4.2 Detection of Copper Oxide by X-ray Photoelectron and Auger Electron Spectroscopy

XPS and AES measurements of copper nanoparticles, repeated periodically during approximately two months, are presented in this section. One of the two samples considered here was covered with ozonated nanoparticles as described in Section 3.3.

The evolution in time of the characteristic peaks in the X-ray photoelectron and Auger electron spectra, obtained from the sample with deposited copper nanoparticles, are presented in Fig. 4.4a and Fig. 4.4b, respectively.

Similarly, changes of characteristic peaks in the X-ray photoelectron and Auger electron spectra, measured from the sample with ozonated copper nanoparticles, are presented in Fig. 4.4c and Fig. 4.4d, respectively.

Two characteristic peaks, located at ~ $933\,eV$ and ~ $952\,eV$ and related to $Cu2p_{3/2}$ and $Cu2p_{1/2}$ states, respectively, are clearly visible in each XPS spectrum of copper nanoparticles, stored in ambient air condition after deposition (see Fig. 4.4a). The satellite band at ~ $945\,eV$ becomes more pronounced with time. Over time these two distinct bands become less symmetric due to emergence of shoulder peaks, related to CuO oxide or Cu(OH$_2$) contribution, as well as intensity of the Cu^{2+} satellite peak increases.

Meanwhile, the Auger spectra from the same sample (Fig. 4.4b) contain Cu LMM peaks where the dominance of Cu$_2$O is observed together with a weaker shoulder of metallic copper. It also worth noting a peak, located at around $910\,eV$, which could be related to LVV Auger transitions [144]. This peak disappears with time.

XPS spectra from ozonated copper nanoparticles (Fig. 4.4c) are very different, where the signal of two bands at ~ $933\,eV$ and ~ $952\,eV$ corresponding to $Cu2p_{1/2}$ and
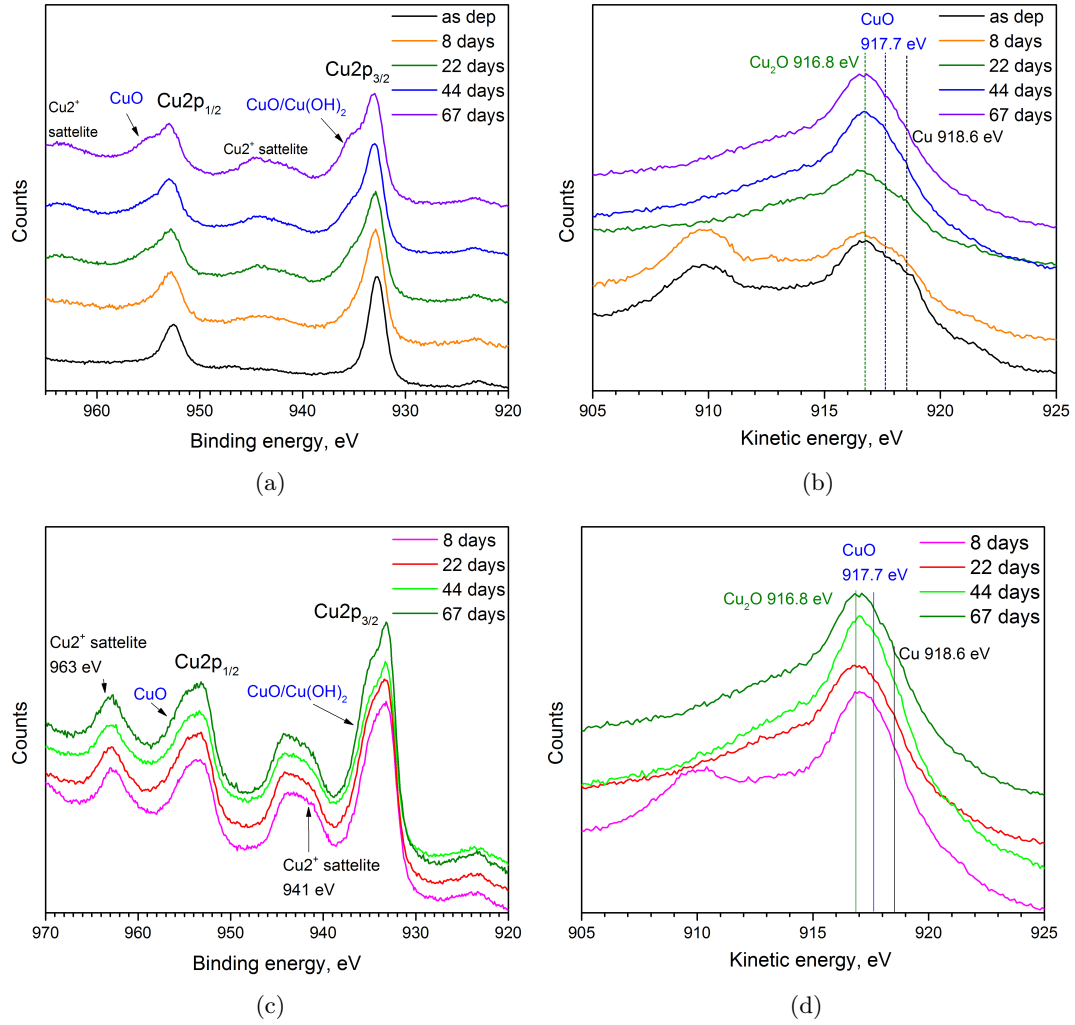
(a)

(b)

(c)

(d)

FIGURE 4.4: Time evolution of $Cu2p_{1/2}$ and $Cu2p_{3/2}$ states in X-ray Photoelectron Spectra (a, c) and bands of Cu, Cu_2O and CuO (kinetic energies are indicated by vertical lines) in Auger Electron Spectra (b, d), obtained from freshly deposited and ozonated copper nanoparticles, respectively. Spectra are vertically shifted for a clear graphical representation of measurements, performed at different times

$Cu2p_{3/2}$ states, emerge together with strong satellite peaks at ~ 963 eV and ~ 941 eV. An increase of CuO shoulder at $Cu2p_{1/2}$ state as well as shoulder of CuO/Cu(OH)$_2$ for $Cu2p_{3/2}$ state, are observed over time. Moreover, the signal from two satellite peaks of Cu^{2+} state, which are typically attributed to CuO phase [145], is considerably intense. At the same time, the Auger spectra from ozonated particles (Fig. 4.4d) have pronounced peak of CuO meanwhile no clear signal of metallic copper is observed. Compared to non-ozonated nanoparticles, the spectra of the UV-ozone treated ones do not show any significant time evolution. Moreover, the peak at ~ 910 eV is present in the first measurement, as it was detected in the Auger spectra of freshly deposited particles, kept in ambient without any treatment.

4.3 Extinction Spectra of Copper and Silver Nanoparticles

In this section, the extinction spectra of silver and copper nanoparticles are presented.

4.3.1 Silver Nanoparticles

Extinction spectra of silver nanoparticles of four distinct sizes were used to analyze variations of the plasmon band, related with the mean diameter of the deposited nanoparticles. More precisely, the AFM measurement presented in Section 4.1 are considered to estimate the size of nanoparticles fabricated with different deposition parameters.

The extinction spectra measured from samples with each size of nanoparticles are presented in Fig. 4.5. The plasmon band with maximum, located in the range of wavelengths between $370\,nm$ and $390\,nm$, is clearly visible in every spectrum.
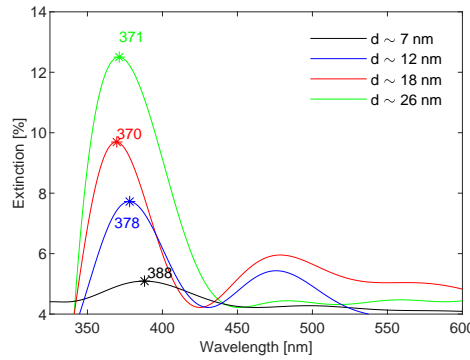

FIGURE 4.5: Extinction spectra of Ag nanoparticles with different sizes. The wavelengths corresponding to the maximum values of the extinction are marked

Considering the sample covered with the smallest silver nanoparticles ($d \sim 7\,nm$, black), the maximum value of the plasmon band is located at $388\,nm$. In the case of larger nanoparticles ($d \sim 12\,nm$, blue, $d \sim 18\,nm$, red, and $d \sim 26\,nm$, green), the positions of the corresponding extinction maxima are blueshifted, towards smaller wavelengths.

The intensity of the extinction band increases in relation to the mean size of nanoparticles.

Less pronounced secondary peaks, located around $\lambda \sim 470nm$, are visible in each measurement.

4.3.2 Copper Nanoparticles

Extinction spectra of copper nanaoparticles of two sizes (d $\sim$ 19 nm and d $\sim$ 24 nm) were measured periodically to investigate the stability of the LSPR, when the samples were stored in ambient condition. Below, these two sizes of nanoparticles are refereed as *small* and *large*.

One substrate covered with small copper nanoparticles (Fig. 4.6b) and one sample covered with large copper nanoparticles (Fig. 4.6d) were treated in ozone environment

immediately after the deposition process, and thus indicated as *ozonated copper*. Two more samples with small Fig. 4.6a and large copper nanoparticles (Fig. 4.6c) have been exposed to ambient laboratory conditions starting from the moment after they were removed from deposition chamber, without being exposed to any specific treatment. The latter two samples are named as *pure copper*.

A few selected extinction spectra of each sample are presented in Fig. 4.6. For each case, the spectra presented as black lines were measured immediately after the deposition, noted in the figures as *As Dep*. Also, the blue lines represent measurements performed approximately 50 days after the deposition, the magenta lines (if present) corresponds to a period of approximately 70 days, meanwhile the green lines corresponds to measures taken after more than 5 months. In the cases of the ozonated samples, the extinction spectra depicted in red, and indicated in the legend as *Ozonated*, were measured immediately after the samples were treated in ozone environment.

Thus, a distinguishable extinction peak is observed in every spectra and the wavelength position corresponding to the maximum value is superimposed to each diagram. Small variation of intensity can be discerned from these selected spectra.
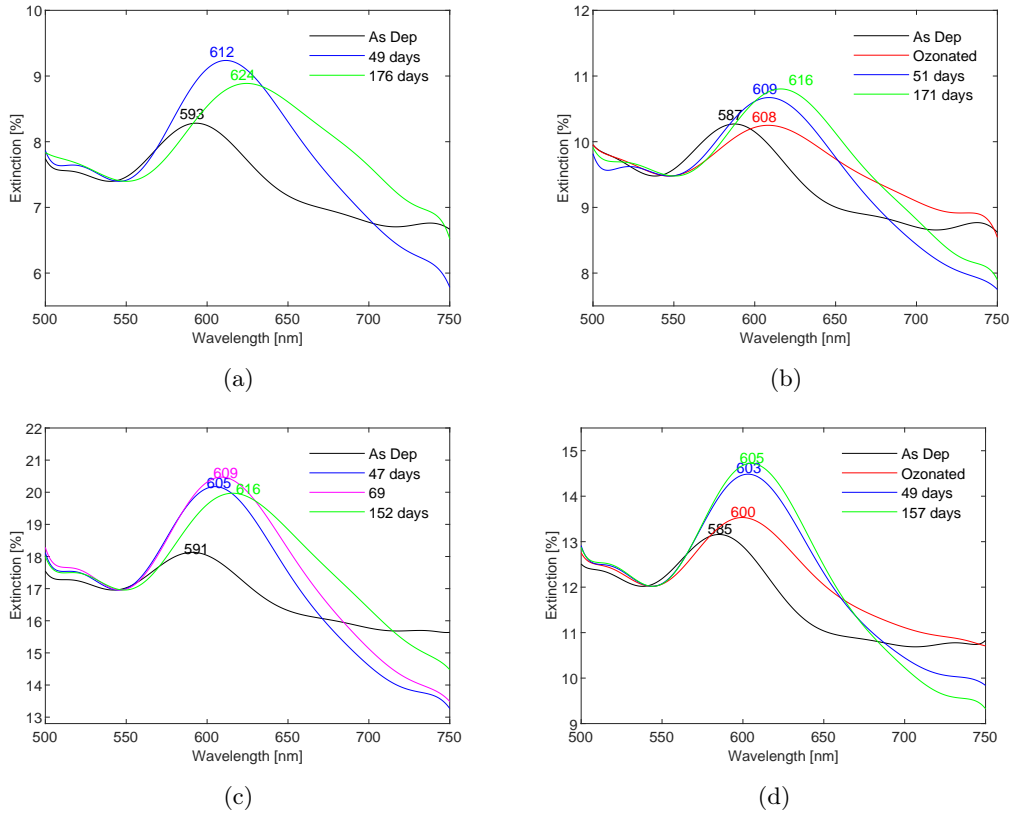

FIGURE 4.6: Extinction spectra measured over time of the samples with a) small pure Cu NPs, b) small ozonated Cu NPs, c) large pure Cu NPs and d) large ozonated Cu NPs. The wavelength of each peak is indicated

In order to study the stability of plasmonic properties exhibited by copper nanoparticles, the features of the plasmon band were monitored over a period of 6 months and shown in Fig. 4.7. The change of the band intensity, ΔExt in Fig. 4.7a, was estimated in reference to the values measured after the deposition of each sample.

Likewise, shifts of band maxima, $\Delta\text{WL}_{\text{Peak}}$ in Fig. 4.7b, are compared to the initial peak position measured after deposition. In these diagrams, the black and red marks correspond to small and large pure copper nanoparticles, respectively. Meanwhile, blue and green marks are assigned to small and large ozonated copper nanoparticles, respectively.
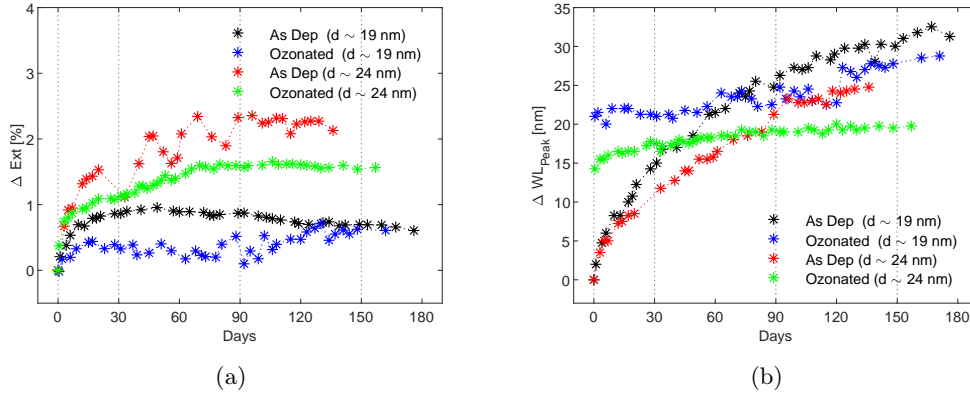

(a) (b)

FIGURE 4.7: Evolution of a) intensity and b) position of the extinction
peaks, of the samples measured over period of ~ 6 months

4.4 SERS Measurements of Methylene Blue

The vibrational spectrum of methylene blue molecules was measured using substrates covered with metallic nanoparticles, and the results were compared with the spectrum measured in Normal Raman condition (see Section 3.5).

The Raman scattering peaks, commonly referred to vibrational modes of methylene blue molecules [146], are clearly visible in the spectrum obtained in Normal Raman condition. These peaks are indicated in Fig. 4.8.
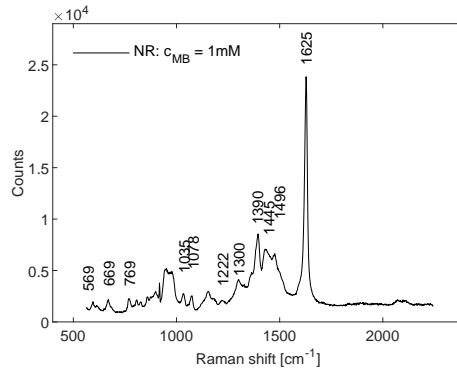

FIGURE 4.8: Normal Raman spectrum of methylene blue

The characteristic peaks of the analyte were also detected with SERS substrates. Hence, all the spectra in this section are presented together with the result obtained in Normal Raman condition, providing a visual comparison. Moreover, two distinct peaks, located at ~ $1400\,cm^{-1}$ and ~ $1600\,cm^{-1}$, were detected with highest intensities, thus, these have been selected as a reference to compare the performance of different SERS substrates. For each measurement, the same volume of $1mM$ aqueous solution

of methylene blue was deposited on SERS substrates with different coverage and size of deposited nanoparticles.

In the first case, copper SERS substrates, fabricated with nanoparticles of $d \sim 24\,nm$ and different surface coverage of particles which are refereed here as high (H, red line) and low (L, blue line), are presented in Fig. 4.9a. The detected spectra are presented in Fig. 4.9a, showing a higher intensity of the signal obtained from the copper SERS substrates with high coverage of deposited nanoparticles. The enhancement factors evaluated for the two reference peaks were 4.43 and 1.29, respectively, for high coverage of nanoparticles, and 3.67 and 1.05, respectively, for low coverage.

At the same time, the Raman spectrum, measured from a copper SERS substrate with high coverage and smaller nanoparticles ($d \sim 19\,nm$, blue line), is presented. This result is visually compared with the spectrum obtained from the copper SERS substrate covered with larger particles ($d \sim 24\,nm$, red line in Fig. 4.9b), introduced previously. Comparing these two spectra, it is possible to see that higher signal enhancement was obtained with larger copper nanoparticles and a lower signal intensity is observed in case of substrate, covered with smaller copper particles. Indeed, the corresponding enhancement factors are 1.51 from the peak at $\sim 1400\,cm^{-1}$ and 0.49 considering the peak at $\sim 1600\,cm^{-1}$.

Furthermore, a third set of samples, fabricated with ozonated copper nanoparticles with two different sizes ($d \sim 19\,nm$, blue line and $d \sim 24\,nm$, red line) was investigated. The obtained SERS spectra are presented in Fig. 4.9c, in which the intensity of the detected signal is on the same scale as for the Normal Raman measurement (black). Accordingly, the enhancement factors evaluated for the peaks located at $\sim 1400\,cm^{-1}$ and $\sim 1600\,cm^{-1}$ are 1.57 and 1.09 respectively, from the copper SERS substrate covered with smaller ($d \sim 19nm$) nanoparticles. Meanwhile, for the substrate covered with larger nanoparticles ($d \sim 24nm$) the enhancement factors are 1.35 and 0.94 for the two reference peaks.

The values of the enhancement factor evaluated for the different copper SERS substrates are summarized in the last two columns of Table 4.2. In this table are distinguished samples with different size (in the 1st column), ozonated and as deposited particles (in the 2nd column), and different coverage (in the 3rd column).

TABLE 4.2: SERS enhancement factors of plasmonic substrates with copper nanoparticles. Reference peaks of methylene blue, $1mM$, coverage (H-high, L-low) and size of nanoparticles are indicated

Diameter [nm]	Type	Coverage	EF @ $1400\,cm^{-1}$	EF @ $1600\,cm^{-1}$
19	As Dep	H	1.51	0.49
	Ozonated	H	1.57	1.09
24	As Dep	L	3.67	1.05
	As Dep	H	4.43	1.29
	Ozonated	H	1.35	0.94

Moreover, the applicability of silver nanoparticles for SERS substrates was investigated. The efficiency of silver SERS substrates was initially studied considering different coverage and sizes of the deposited silver nanoparticles, keeping the same concentration ($1mM$) of the methylene blue for each sample.

Regarding the spectra obtained from two substrates fabricated with different coverage, low L, blue line and high H, red line, of deposited silver nanoparticles with $d \sim 18\,nm$
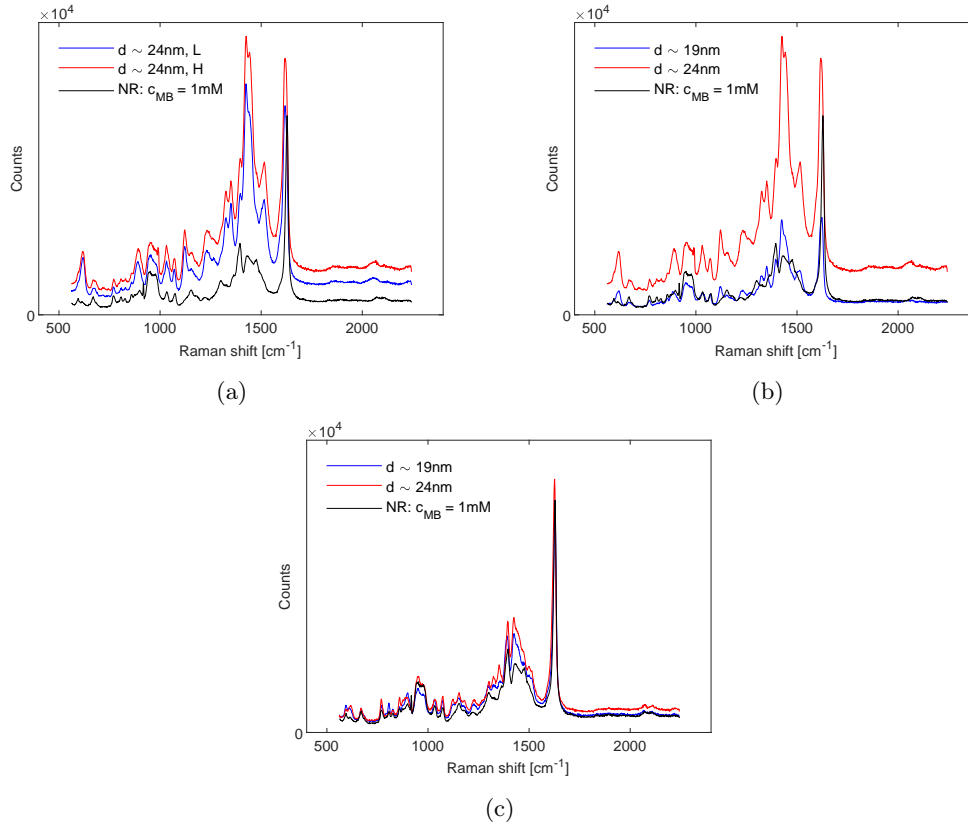
FIGURE 4.9: SERS spectra of $1\,mM$ methylene blue obtained from
copper SERS substrates with: (a) different coverage, (b) different size
and c) ozonated copper nanoparticles of different size

(see Fig. 4.10a), a stronger Raman signal was detected from sample with high coverage of silver nanoparticles-similarly as in case of copper. Thus, considering the sample with lower coverage of silver nanoparticles, the enhancement factor for the peak located at $\sim 1400\,cm^{-1}$ is 13.39, and the value evaluated considering the peak located at $\sim 1600\,cm^{-1}$, is 8.04. Meanwhile, the enhancement actors, obtained from sample with higher coverage are 24.56 and 21.33 for the same reference peaks, respectively.

Moreover, the higher Raman scattering signal intensity was obtained when substrates with larger particles (put size) were utilized. (see Fig. 4.10b). This result is more evident when the spectrum obtained from the silver SERS substrate covered with small ($d \sim 12\,nm$, blue line) nanoparticles, is compared with the signal obtained from similar samples but covered with larger nanoparticles ($d \sim 18\,nm$, red line and $d \sim 26\,nm$, green line). Indeed, considering the two samples with larger nanoparticles, the difference in the intensity of the signal is not so pronounced. Thus, the enhancement factors evaluated for these three samples, referred to the two reference peaks ($\sim 1400\,cm^{-1}$ and $\sim 1600\,cm^{-1}$), respectively, are 2.68 and 2.08, 24.56 and 21.33, 27.29 and 28.8, with diameters varying from $d \sim 12nm$ to $d \sim 18nm$ and $d \sim 26nm$.

The evaluated values of the enhancement factor (4th and 5th column) are summarized in Table 4.3. In this table, it is indicated the mean size (1st column) and the estimated coverage (2nd column) of silver nanoparticles deposited on the corresponding substrate.

Furthermore, the possibility to detect analyte at lower concentrations utilizing silver
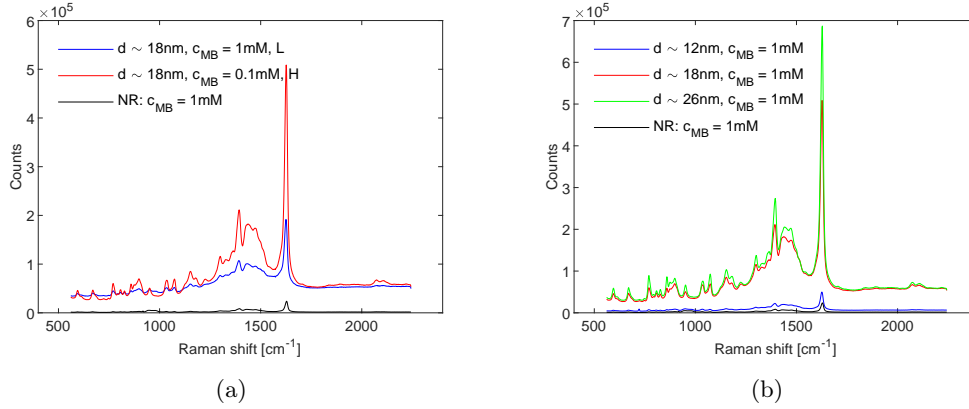
(a)   (b)

FIGURE 4.10: SERS spectra of $1\,mM$ aqueous solution of methylene
blue obtained with: (a) different coverage and (b) different size of the
deposited silver nanoparticles

TABLE 4.3: SERS enhancement factors of plasmonic substrates with
silver nanoparticles. Reference peaks of methylene blue, coverage and
size of nanoparticles are indicated

Diameter [nm]	Coverage	EF @ $1400\,cm^{-1}$	EF @ $1600\,cm^{-1}$
12	H	2.68	2.08
18	L	13.39	8.04
	H	24.56	21.33
26	H	27.29	28.8

nanoparticles was investigated. Therefore, different silver-based SERS substrates with
varying mean size of the deposited nanoparticles from $d \sim 12\,nm$ (Fig. 4.11a) to
$d \sim 18\,nm$ (Fig. 4.11b) and $d \sim 24\,nm$ (Fig. 4.11c)were considered. More precisely, the
concentration of methylene blue was decreased to $1\mu M$ (blue line), $0.1\mu M$ (red lines)
and $0.01\mu M$ (green lines).

It is important to notice that spectra from the $0.01\mu M$ concentration of methylene
blue were measured only for the silver SERS substrates covered with nanoparticles
of $d \sim 12\,nm$ and $d \sim 18\,nm$. However, none of the characteristic peaks of methylene
blue was detected from the latter sample.

From these results, the enhancement factor, relative to the reference peaks, was evalu-
ated for each sample. Thus, considering the silver SERS substrate covered with small
($d \sim 12\,nm$) nanoparticles and decreasing concentrations of methylene blue aqueous
solution from $1\,\mu M$ to $0.1\,\mu M$ and $0.01\,\mu M$, the enhancement factors, relative to each
solution, are 1.41×10^4, 2.67×10^4 and 1.22×10^5, referred to the peak located at
$\sim 1400\,cm^{-1}$. At the same time, the enhancement factors evaluated from the intensity
of the peak located at $\sim 1600\,cm^{-1}$ are 1.41×10^4, 2.67×10^4 and 1.22×10^5.

Similarly, the enhancement factors, relative to decreasing concentration of analyte
solution ($1\mu M$ and $0.1\mu M$), evaluated for the spectra obtained from silver SERS
substrates covered with nanoparticles of $d \sim 18\,nm$, are 2.51×10^4 and 4.07×10^4,
considering the peak located at $\sim 1400\,cm^{-1}$. Regarding the other reference peak
($\sim 1600\,cm^{-1}$), the enhancement factors are 1.24×10^4 and 2.86×10^4.

Silver SERS substrates covered with large ($d \sim 26\,nm$) nanoparticles led to enhance-
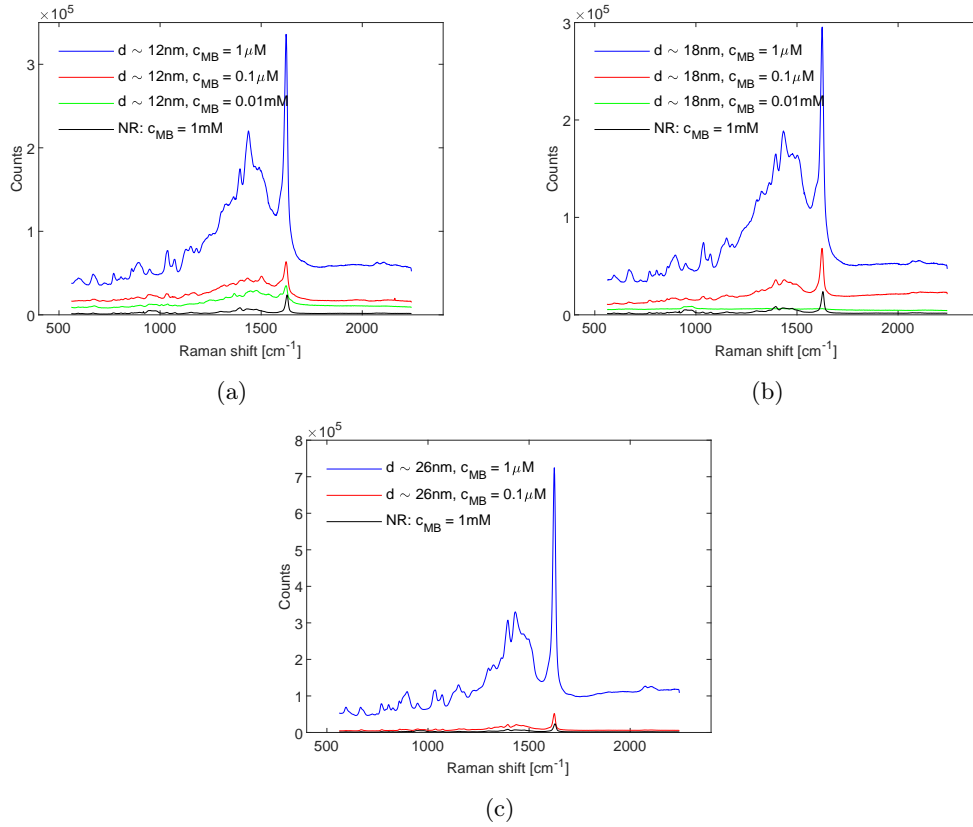ment factor for the peak located at $\sim 1400\,cm^{-1}$, of 3.04×10^4 and 2.88×10^4, relative

FIGURE 4.11: SERS spectra of methylene blue obtained from substrates with different-sized silver nanoparticles: a) $d \sim 12\,nm$, b) $d \sim 18\,nm$ and c) $d \sim 26nm$. Concentrations of methylene blue are indicated in the legend

to concentration of the analyte solution of $1\mu M$ and $0.1\mu M$, respectively. Simultaneously, the enhancement factor of the second reference peak ($\sim 1600\,cm^{-1}$) are 4.38×10^4 and 2.17×10^4, relative to decreasing concentration of the analyte solution.

The evaluated values of the enhancement factor, reported from different concentration (1st column) of the analyte solution, deposited on silver SERS substrates covered with nanoparticles of different sizes (2nd column), are summarized in Table 4.4.

TABLE 4.4: SERS enhancement factors of plasmonic substrates with silver nanoparticles. Reference peaks of methylene blue, analyte concentration and sizes of nanoparticles are indicated

$c_{MB}\,[\mu M]$	Diameter [nm]	EF @ $1400\,cm^{-1}$	EF @ $1600\,cm^{-1}$
1	12	3.05×10^4	1.41×10^4
	18	2.51×10^4	1.24×10^4
	26	3.04×10^4	4.38×10^4
0.1	12	6.08×10^4	2.67×10^4
	18	4.07×10^4	2.86×10^4
	26	2.88×10^4	2.17×10^4
0.01	12	3.63×10^5	1.22×10^5

4.5 Mass Spectra of Biological Tissues Obtained Using Metal Nanostructures

Mass spectra of biological tissues covered by with Cu and Ag NPs, measured utilizing Laser Ionization/Desorption technique, are presented in this section.

4.5.1 Mass Spectra Obtained with Cu Nanoparticles Matrices

Firstly, the mass spectrum from the matrix of Cu NPs without analyte was measured in sub-AP MALDI unit in order to determine Cu-containing ions, originating from surface of nanoparticles.
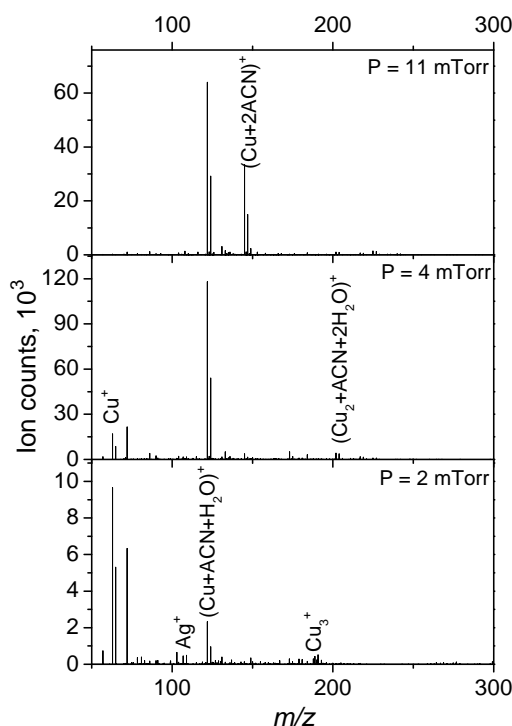

FIGURE 4.12: LDI mass spectra obtained from Cu NPs matrix at different pressures

As can be seen in Fig. 4.12, the most prominent ions, excited from matrix with Cu NPs, are Cu+, (Cu+ACN+H2O)+, (Cu+2ACN)+, and (Cu2+ACN+2H2O)+, where ACN is an acetonitrile (C_2H_3N).

Applicability of copper nanoparticles matrices in detection of phospholipids in biological tissues was evaluated by comparison with signal obtained using matrix of thin copper film, obtained by sputtered deposition on silicon.

In Fig. 4.13, the mass spectrum of pig brain tissue covered with Cu NPs (in red) is compared with the spectrum obtained from a copper thin film (in green) which was employed as a matrix covering the analyte.

One of the most common phospholipids observed in the pig brain tissue is phosphatyl-choline PC(34:1), which is detected as [PC(34:1)+H]+ corresponding to three ions at m/z = 760.58, 761.58 and 762.59 (as can be seen in Fig. 4.14a) with ratio between ions corresponding to the isotopic pattern. Meanwhile the lipid from same group,
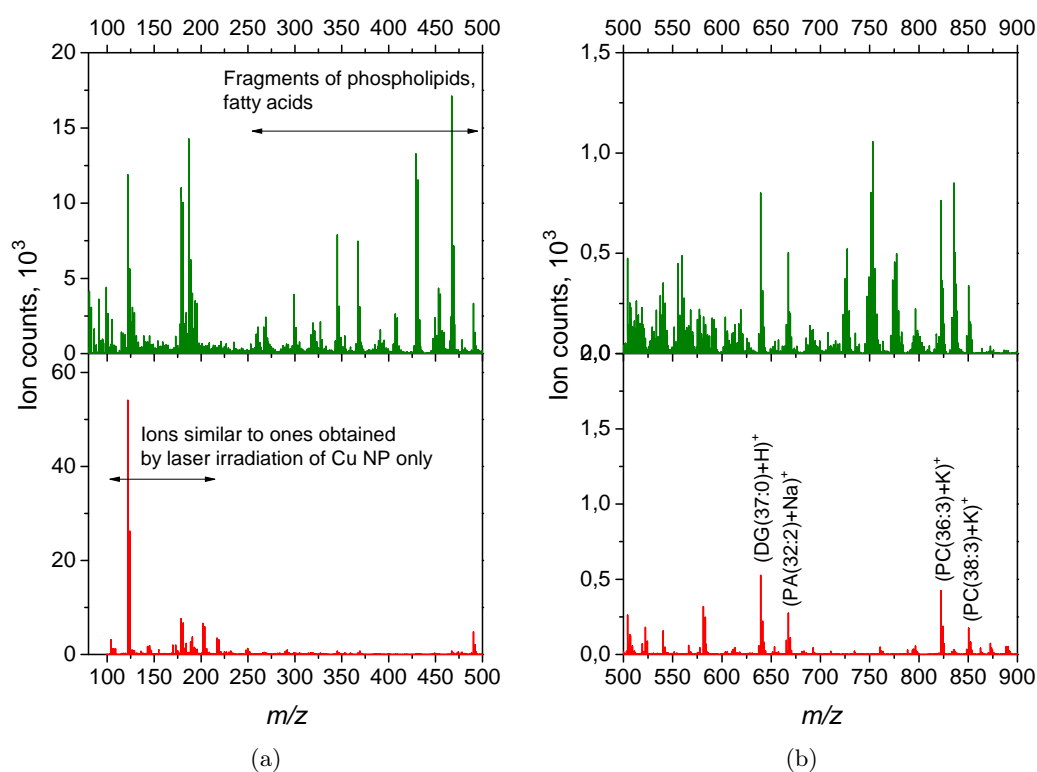
FIGURE 4.13: Mass spectra from pig brain tissue, obtained from Cu
NPs matrix (bottom panels) and Cu thin film matrix (top panels): a)
low ion mass region, b) high ion mass region

PC(36:4), was detected from the sample coated with Cu thin film, but not found in a case of Cu-nanoparticles matrix (Fig. 4.14b).

In the notations of phospholipids, 34 and 36 mean the combined number of CH_2 chains in both fatty acids, while 1 and 4 means the number of double bonds located in the fatty acid chain.

FIGURE 4.14: Phospholipids in mass spectra of pig brain, measured utilizing matrices of copper thin film (green) and copper nanoparticles (red). Detected ions of phosphatylcholine: a) PC(34:1) b) PC(36:4)
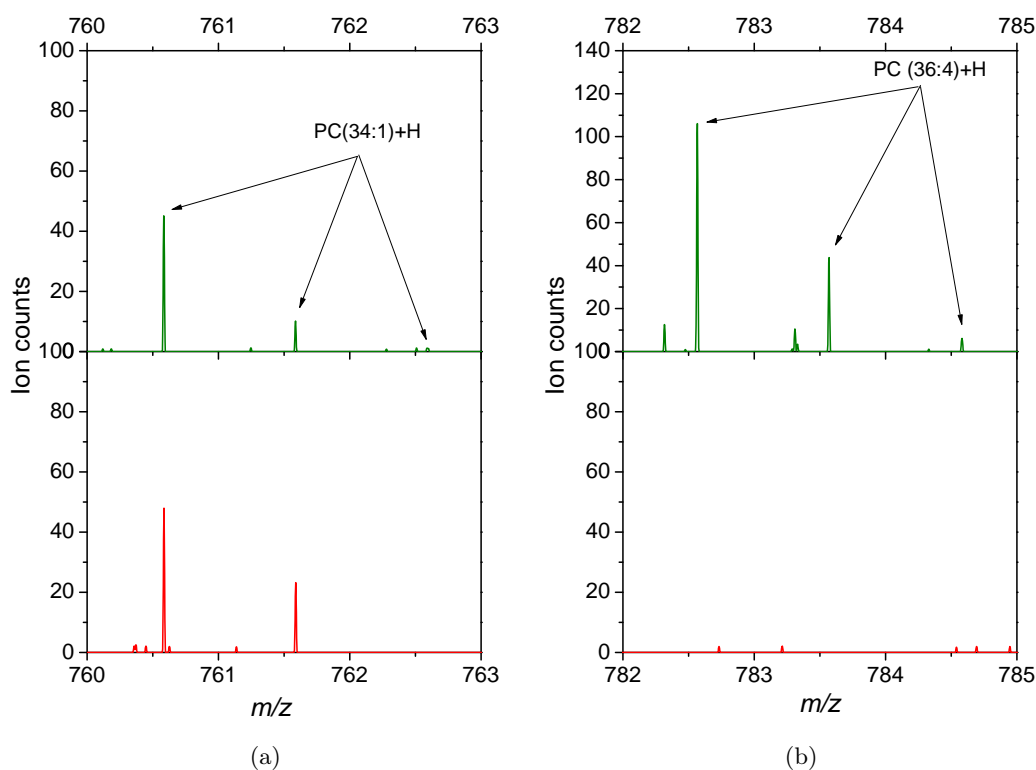
4.5.2 Mass Spectra Obtained with Ag Nanoparticles Matrices

The mass spectra obtained from gas-aggregated silver nanoparticles in positive and negative ion extraction modes, are presented in Fig. 4.15 As it can be seen, it contains only ionized silver adducts: Ag^+, $Ag2^+$, $Ag3^+$. Additional adducts with water/acetonitrile(ACN) were also detected, which can be a result of small oxidation on the nanoparticle surface, or due to silver fragments in a gas-phase reaction with surrounding humidity and acetonitrile, similarly to the case of copper, presented above.

Mass spectra of phospholipids, measured from samples with pig brain tissue covered by silver nanoparticles with different sizes, are presented in Fig. 4.16. Negative and positive ion extraction modes were employed.

As seen in Fig. 4.16, positive ion spectra contains much lower variety of ions, compared to the one, obtained in the negative ions extraction mode. However, in both cases, matrices with smaller silver NPs resulted in increase of detection signal, while ion variability remains independent of particle size.

Similarly, negative ions mass spectrum, measured from sample with beeswax using substrate with small silver nanoparticles (Fig. 4.17a), demonstrate higher variability and stronger signal, compared with spectra of positive ions (Fig. 4.17b. The trend of ion counts increase for smaller sizes of nanoparticles, seen in the case of phospholipids from pig brain mass spectra, is also observed in negative ions mass spectra of beeswax. Particulary, mass spectrum of beeswax obtained with small silver nanoparticles (Fig. 4.17c) contains signals from saturated/unsaturated fatty acids with maximum at 367 m/z (tetracosanoic acid). Moreover, it is possible to detect unsaturated
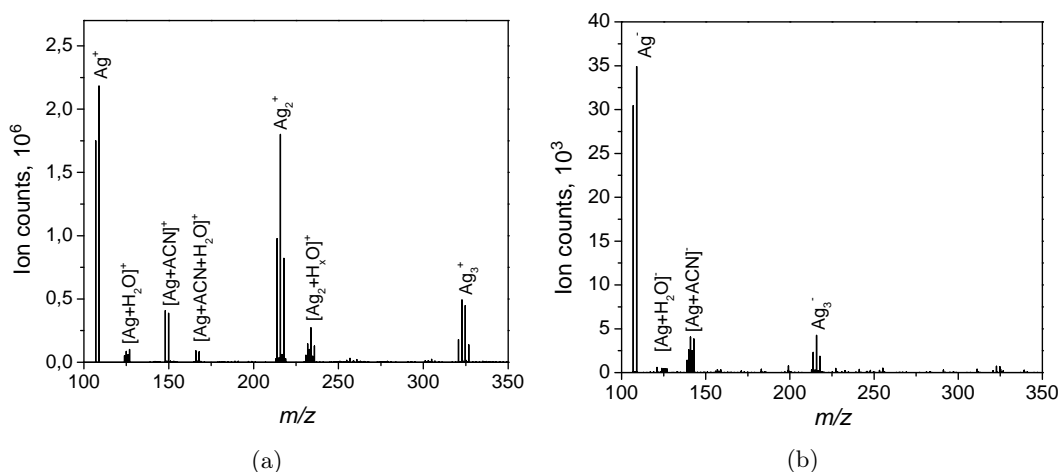
FIGURE 4.15: Positive ion (a) and negative ion (b) mass spectra obtained from gas aggregated silver nanoparticles (d~18 nm)
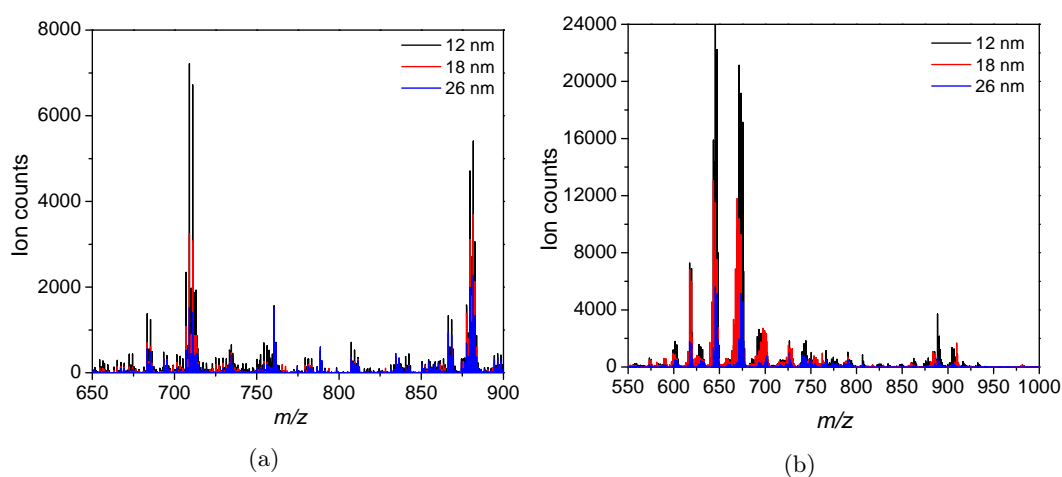

FIGURE 4.16: Phospholipids region in mass spectra of pig brain, measured using Ag NPs matrices: a) positive ions mode, b) negative ions mode. Sizes of nanoparticles, deposited onto substrates with analyte, are indicated

fatty acids such as [C24:1]. Also, a formation of [2M+Ag-H]- ions is observed in the higher mass regions.

(a)

(b)

(c)
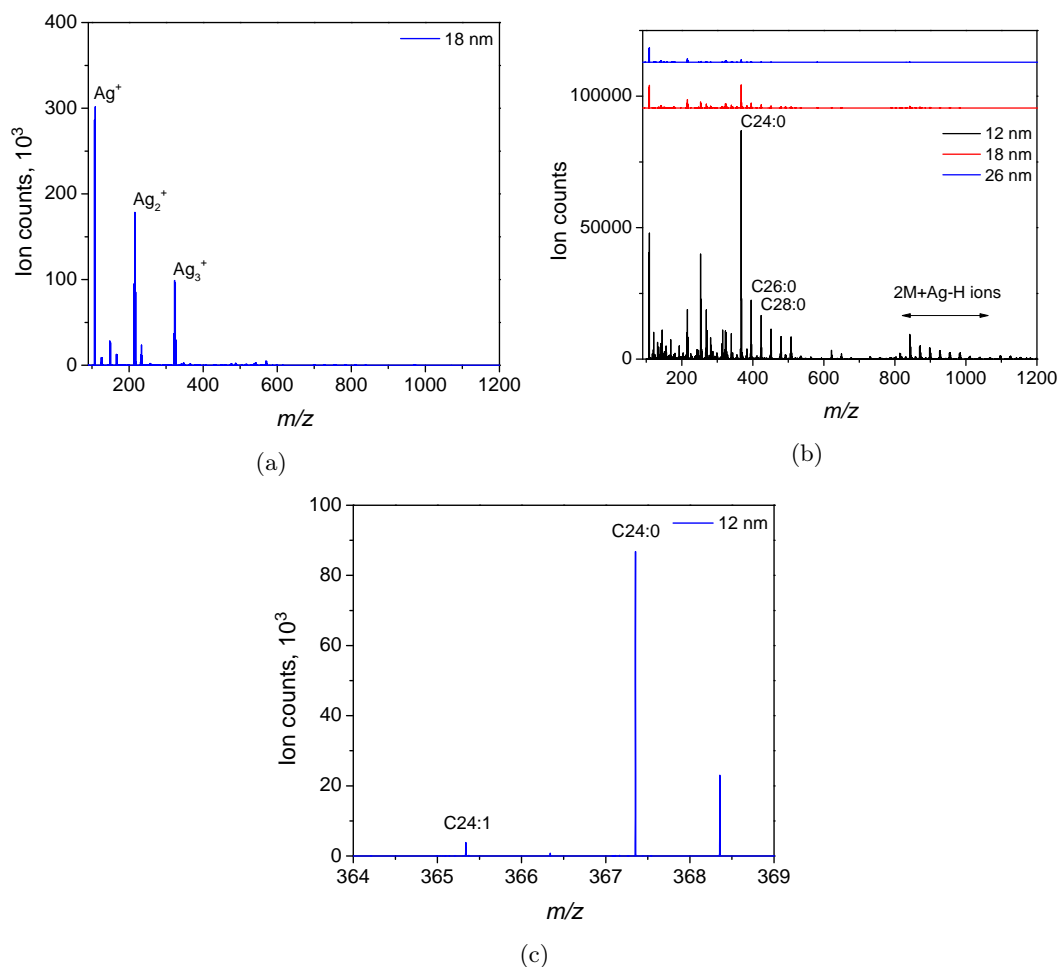
FIGURE 4.17: Mass spectra of beeswax measured with Ag NPs matrices: a) positive ions extraction mode, small NPs, b) negative ions extraction mode (with offset), different sizes of NPs, c) negative ions extraction mode, small particles, fatty acids region

4.5.3   Laser Irradiation of Silver Nanoparticles

The effect of laser irradiation on silver nanoparticles was investigated by SEM and AFM as described in Section 3.6.1. The irradiated areas are clearly visible in the SEM images presented in Fig. 4.18.
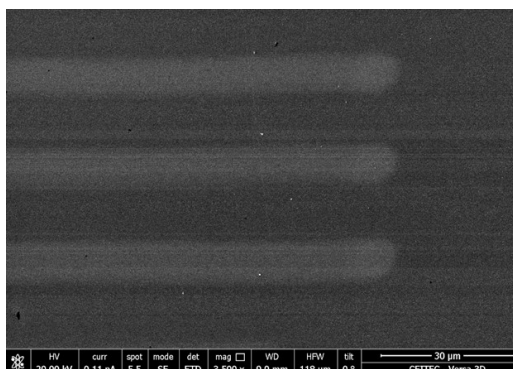
FIGURE 4.18: Example of SEM image of the sample with irradiated silver nanoparticles. Bright lines, scanned by laser, are clearly visible

A few SEM images with high magnification, are taken from frames with different laser energy, LE=5 and LE=30. In the areas non-irradiated by the laser beam, individual nanoparticles are clearly visible (see Fig. 4.19a and Fig. 4.19b). The next two panels (see Fig. 4.19c and Fig. 4.19d) correspond to the boundary, separating, from top to bottom, the non-irradiated and irradiated areas. In this images, a gradual decrease in contrast, making difficult to identify the nanoparticles, is noticeable especially in the case of high LE. Moreover, in the bottom of Fig. 4.19f, stripes in vertical (slightly tilted) direction are observable. Nanoparticles can be hardly distinguished in the images taken from the irradiated areas (see Fig. 4.21d Fig. 4.19f)

To identify areas irradiated by the laser beam using AFM, the scans presented in Fig. 4.20 are performed. In panels Fig. 4.20a and Fig. 4.20b it is possible to distinguish between the horizontal stripes populated by nanoparticles and those not clearly showing them. Thus, a good correlation with SEM images is found, showing that the laser irradiation leads to change of the morphology.

The three dimensional morphology of different areas is presented in Fig. 4.21. For the frame I at the boundary between the non-irradiated and irradiated stripes (see Fig. 4.21a and Fig. 4.21b), the particle height gradually decreases. This decrease is much more pronounced for the LE=50. The areas inside the irradiated stripes show either very low in height nanoparticles (Fig. 4.21b for LE=5), or no nanoparticles (Fig. 4.21d for LE=50).

(a)

(b)

(c)

(d)

(e)

(f)
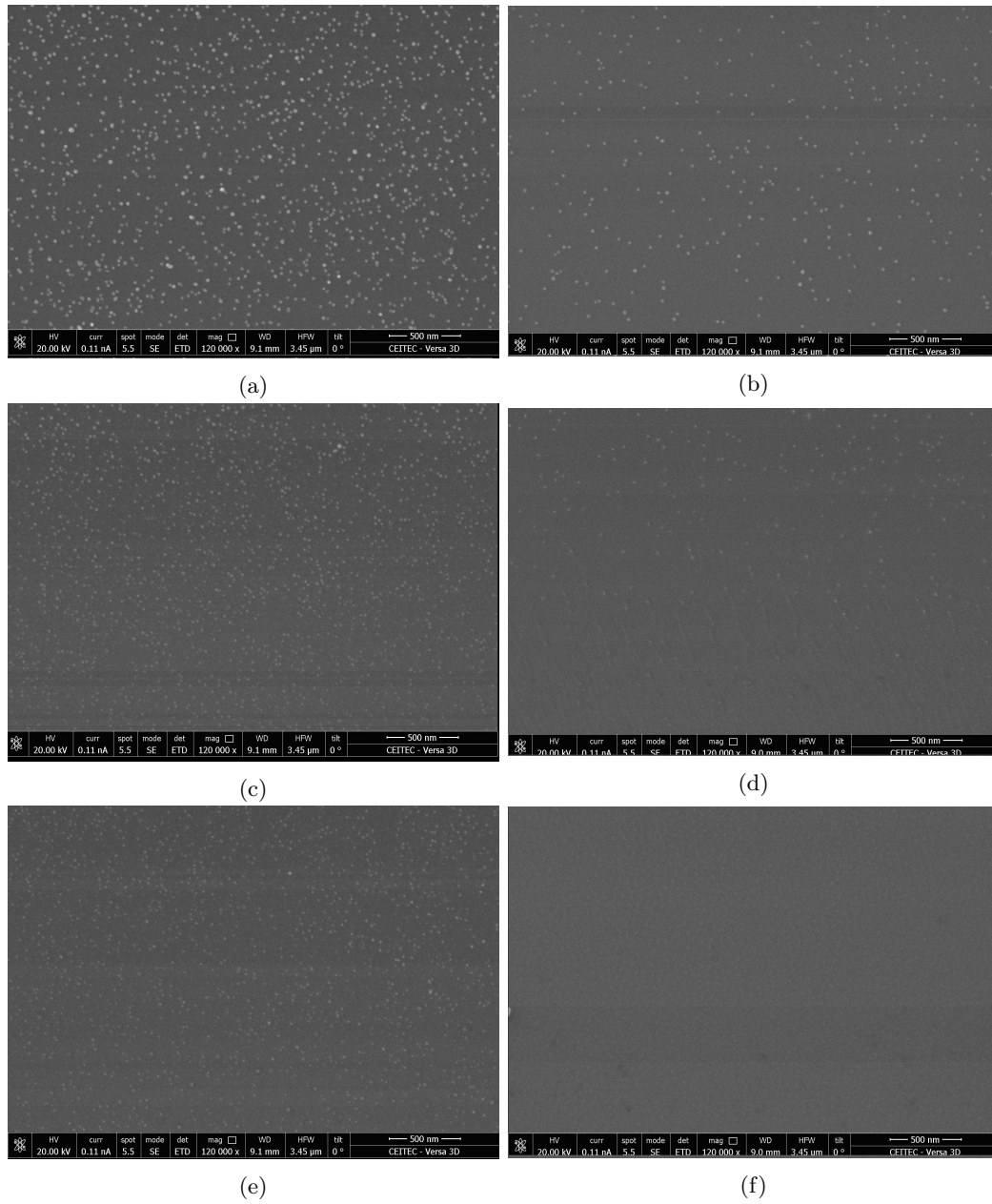
FIGURE 4.19: SEM images taken from a,b) outside, c,d) the edge and e,f) inside the irradiated line with laser energy 5 and 30, respectively
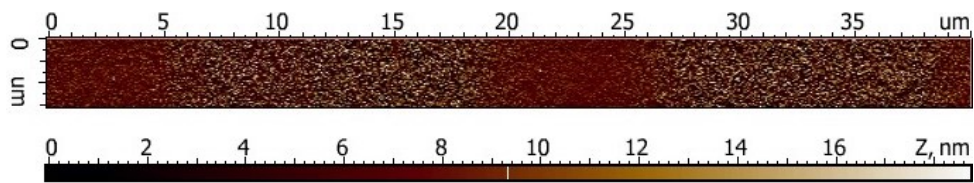
(a)
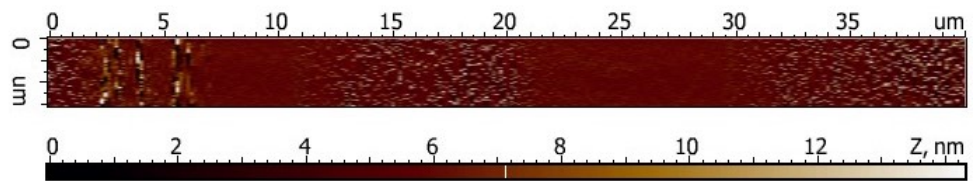
(b)

(c)

FIGURE 4.20: AFM images from the frames irradiated with a) LE=5 and b) LE=50. A schematic is presented in c), indicating with red squares the areas at the edge (I) and inside (II) the laser irradiated stripes

(a)   (b)

(c)   (d)
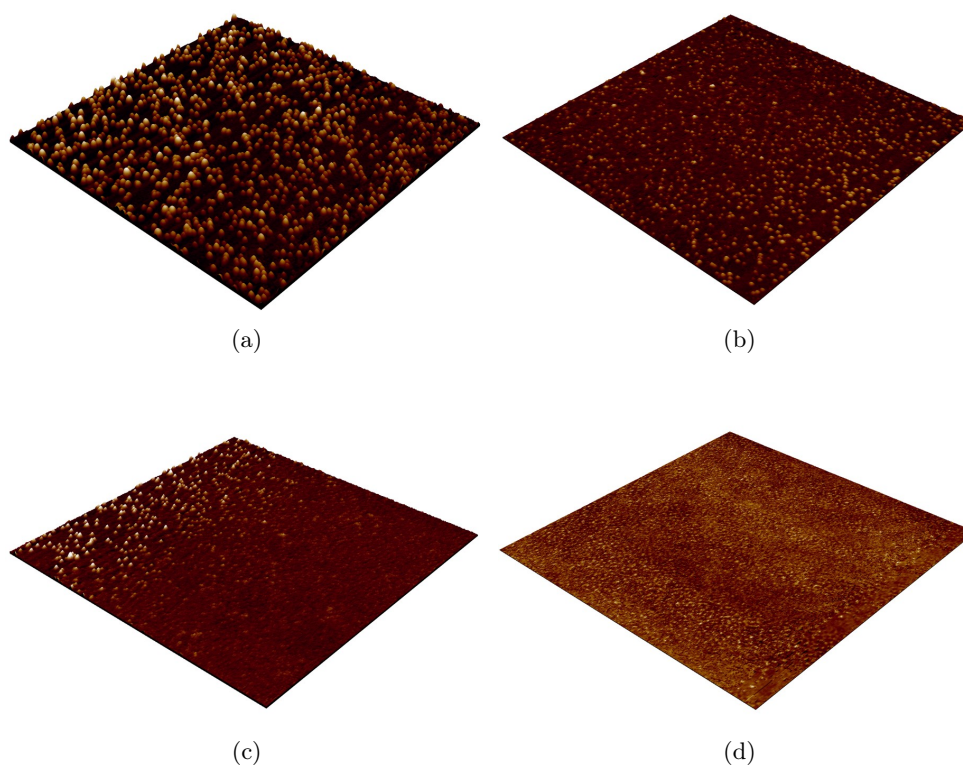
FIGURE 4.21: AFM images for a) the edge and b) inside the line
identified in the frame LE=5, and in c) the edge and d) inside the line
marked by the laser with LE=50

Chapter 5

Discussion

5.1   Size of Nanoparticles

The morphology of supported nanoparticles was investigated with AFM. The results in Section 4.1 allow to identify the shape and surface coverage of the deposited nanoparticles and to investigate the corresponding size distribution, depending on the parameters applied for the mass selection (Section 3.1).

First, the circular shape observed in the 2D AFM images, combined with the hemispherical shape, clearly visible in the 3D AFM images, can be related with nanoparticles of approximately spherical shape, as already shown in earlier studies [17, 141]. However, the lateral dimension of the particles observed in the 2D AFM images is not considered as a reliable data to estimate the real size distribution of the sample as it is affected by the sharpness of the probe tip, due to convolution effects [147]. Hence, the estimation of nanoparticles size is obtained according to the measure of nanoparticles height.

Thus, different size distributions were obtained from samples prepared with different fabrication parameters. It is observed in Fig. 4.2a that a wide range, from $10\,nm$ to $40\,nm$, of nanoparticles size is formed in the aggregation chamber, with mean value at $\sim 17.5\,nm$. The lognormal distribution of nanoparticles size, deposited independently of their mass, or equivalently with $V_{EQMS} = 0V$, reproduce approximately the results expected for nanoparticles produced by gas-aggregation [142].

Meanwhile, the measurement of size selected nanoparticles, through mass filtering, allows to study the size distribution obtained by deflecting the cluster beam with different intensity of the hyperbolic electric field generated in the electrostatic quadrupole (Section 3.1). For each sample, it is identified a mean value of nanoparticles size, corresponding to the most abundant data, and also, a few, less frequent, larger values which are related with the presence of multiply charged nanoparticles (see Fig. 4.2 and Fig. 4.3), as observed by Marom *et al.* [143] and in agreement with Eq. (3.2), as explained in Section 4.1.

Interestingly, it is also observed from the height analysis, that silver and copper nanoparticles with comparable size, are deposited at significantly different voltages. Since the atomic mass of silver is larger compared with copper, it is assumed that less silver atoms are necessary to form nanoparticle of the same weight. In other words, the volume of the deposited nanoparticles will be smaller for heavier materials, if it is assumed the same atomic density, defined as the number of atoms per volume. However, this assumption does not account for different size of the atoms of different materials.

5.2   Oxide Detection in Copper Nanoparticles

Formation of oxide phase, experimentally detected in copper nanoparticles (see in Section 4.2), is discussed in this section. During the period of analysis, two samples were stored in ambient condition and measured periodically (see Section 3.3). One sample was ozonated (see Section 3.1) and the other was not treated after the deposition. Thus, the latter one is referred to the reader as "*as deposited*", while the former as "*ozonated*".

The value of the binding energy for $Cu2p_{3/2}$ electrons, emitted from pure Cu, and that corresponding to Cu_2O, are very similar: 932.6 eV and 932.7 eV, respectively [145, 148]. Therefore, it is nearly impossible to distinguish if the investigated material is either pure copper or copper oxide, from the analysis of the XPS spectrum obtained with freshly deposited copper nanoparticles (Fig. 4.4a).

On the other hand, the difference between the LMM peaks of metallic copper and copper oxides in Auger spectra is larger [149]. Indeed, it is seen in Fig. 4.4b that the maximum signal coincides well with the kinetic energy value of 916.8 eV, corresponding to Cu_2O, but there is also a well-pronounced shoulder at 918.6 eV, which indicates the presence of metallic Cu. However, for the "as deposited" copper nanoparticles, the contribution of the peak at 918.6 eV (pure Cu) decrease with time, while those corresponding to Cu_2O and CuO start dominating. Since Auger electrons are emitted from very thin surface layer (up to 2 nm), formation of an oxide shell around the metallic core can be assumed. The thickness of this shell increases with time surpassing the signal of metallic copper. Additionally, the Cu_2O oxide phase was detected from the AES, already in the measurement taken after the deposition, indicative of the poor stability of copper when exposed to atmospheric oxygen.

Moreover, the time evolution of the Auger spectra from the "as deposited" copper nanoparticles, supports the variations observed in the XPS spectra (see Fig. 4.4a) of the same sample. In the latter case, high-energy shoulders, for both peaks ascribed to $Cu2p_{1/2}$ and $Cu2p_{3/2}$ emissions, start to appear with time. This observation can be interpreted as formation of CuO or even $Cu(OH)_2$, according to the literature [145]. Additionally, the occurrence of Cu^{2+} satellite peaks at 945 eV and 963 eV, is also indicative of the presence of the CuO phase. Thus, it can be concluded that copper nanoparticles exposed to ambient conditions, tend to form initially a Cu_2O oxide shell, which gradually converts into CuO phase with time. These results are in good agreement with the earlier findings [25] but show more details on time evolution.

Meanwhile, features similar to the ones observed in the XPS spectrum from the "as deposited" sample, measured several weeks after the deposition, are visible in the XPS spectrum of the ozonated copper nanoparticles (Fig. 4.4c), already after the first week. More precisely, strong shoulders of $Cu2p_{1/2}$ and $Cu2p_{3/2}$ peaks, as well as intense satellite bands, indicating the presence of CuO and possibly $Cu(OH)_2$, appeared immediately. In opposition to the other sample, where the oxidation in ambient atmosphere was dominated by Cu_2O with gradual transformation to CuO, the oxidation under UV-ozone treatment undergoes predominately through the formation of CuO phase. This tendency is supported by the Auger LMM peaks (see Fig. 4.4d). The predominate formation of CuO is also in agreement with findings of UV-ozone treatment of Cu films analysis published elsewhere [140]. It is worth mentioning that both XPS and Auger spectra of ozonated copper nanoparticles are stable on the time scale of this experiment, i.e. no significant changes in the spectral features. Thus the

composition of the intentionally formed oxide shell, through the ozonation procedure, is unaffected by further oxidation in ambient condition.

5.3 Extinction Spectra of Silver Nanoparticles. Size Effect

Experimentally obtained extinction spectra of different-sized silver nanoparticles, deposited on quartz substrates (Fig. 4.5), are good indication of plasmonic response of silver nanoparticles and its relation with nanoparticles size.

The tendency for plasmon resonance to be more intense for larger structures, predicted theoretically by Eq. (2.3), is evident from the extinction spectra. The intensity of the plasmonic peak increased up to 7.4% considering the sample with largest deposited silver nanoparticles.

At the same time, it is possible to see that plasmonic resonance positions are shifted towards shorter wavelenghts as the size of the nanoparticles increases from $d \sim 7$ nm to $d \sim 18$ nm. However, the position of the peak for the largest nanoparticles ($d \sim 26$ nm) coincide with the position of the peak for nanoparticle with $d \sim 18$ nm.

According to Fröhlich's condition (Eq. (2.4)), the maximum extinction is observed at the wavelength for which the real part of dielectric function of the metal is equal to two times the negative value of the dielectric constant of the surrounding environment. Regarding supported nanoparticles, it is necessary to consider the presence of the substrate material. In other words, for two silver particles located on top of quartz substrate, the value of effective dielectric constant of the surroundings will be larger for the smaller one, which leads to longer wavelength of the plasmon band due to a stronger interaction with the substrate. Consequently, the Fröhlich's condition requires the definition of an effective dielectric constant which properly accounts for all the surrounding materials which may be in the vicinity of the metallic nanostructure.

A possible method to analytically evaluate the effective dielectric constant, was already presented in our previous work [150]. This approximation relates the value of the effective dielectric constant with the size of the metallic nanoparticles, resulting in a reduced contribution of the substrate to the dielectric constant of the surrounding environment when the size of the nanoparticles is increased. Consequently, the position of the peak for large silver nanoparticles was predicted at shorter wavelengths, which is in agreement with the general trend experimentally observed in Fig. 4.5.

However, there is another phenomenon related to the contribution of depolarization field, induced by the polarized matter surrounding the center of a nanoparticle. This effect was described in works by Barber [151] and Meier [152], which introduced the correction of resonance condition where denominator of Eq. (2.3) becomes:

$$\epsilon_r(1 - q^2) + (2 + q^2) + 2/3\epsilon_i q^3 \tag{5.1}$$

here $q = kr$, k-wavenumber and r-particle radius. Eq. (5.1) has to be equal to zero in order to have the resonance. For silver nanoparticles with greater radii, this condition is satisfied for more negative values of ϵ_r which corresponds to longer wavelenghts of the LSPR.

The effect of the substrate, leading to a blueshift of the plasmon band, is dominant for small nanoparticles, as observed in Fig. 4.5 considering d = 7, 12 18 nm. However, with size increase, the substrate effect decreases, while the contribution of the depolarisation effect emerges, leading to redshift of the plasmon band.

Moreover, in this discussion we would also like to address secondary bands at longer wavelengths (470 – 480 nm), which appear in all the extinction spectra, except the one of small particles (d ~ 7 nm). The presence of these bands were earlier mentioned in the literature [141] and attributed to the formation of dimers of nanoparticles located in close proximity. Because of the non spherical shape, these structures introduce a secondary plasmonic mode corresponding to collective oscillations of the electrons in the elongated direction.

5.4   Extinction Spectra of Copper Nanoparticles. Evolution in Time

Similarly, the plasmonic response of copper nanoparticles with different sizes was analyzed in terms of extinction spectra (Fig. 4.6). In the case of large pure copper nanoparticles, the extinction band is identified at λ = 590 nm, and a small blueshift and increase of intensity is observed when compared to the plasmon band of smaller nanoparticles, with maximum resonance at 591 nm. However, it is important to emphasize that the precise position of the plasmon band can be affected by noise in the measurement. Nevertheless, this trend replicates the effect observed from silver nanoparticles with different sizes (Fig. 4.5) and discussed in Section 5.3. However, the secondary peak visible in the spectra of silver nanoparticles and attributed to the presence of dimers (see Section 5.3), is not detected from any sample covered with copper nanoparticles. A possible explanation can be related with the formation of an oxide phase immediately after taking the samples from vacuum chamber into ambient atmosphere, which creates a separation between two nanoparticles and, thus, preventing the formation of dimers. Indeed, emission from the oxide phase is detected in the Auger spectrum (Fig. 4.4a) of "as deposited" copper nanoparticles, already after the deposition, supporting this explanation.

Therefore, the characterization of optical properties is necessary to anticipate the possible application of plasmonic nanoparticles, involving the interaction with monochromatic light. In this regard, the stability of plasmonic properties of copper is highly debatable in literature, mentioning the nanoparticles oxidation in ambient conditions to be the main reason for the degradation of the LSPR with time. The XPS and Auger spectroscopy data (Fig. 4.4a), show that, indeed, copper nanoparticles undergo oxidation in ambient atmosphere, as already discussed in Section 5.2, modifying the environment surrounding the metallic nanoparticles.

In this section, the evolution of extinction spectra of copper nanoparticles over time (Fig. 4.7) is discussed, aiming to indirectly relate the oxidation process with changes in the plasmonic property.

This experiment shows that the intensity of the plasmonic bands, observed in the extinction spectra of small (d ~ 19nm, see Fig. 4.6a) and large (d ~ 24nm, see Fig. 4.6c) pure copper nanoparticles, were increasing in the first two months of observation, reaching its maximum value after 49 and 69 days, respectively, and the increase is more pronounced in the case of larger nanoparticles. Yet, the increase of intensity is not larger than 2%. Nevertheless, these results are combined with the study of

the XPS and AES discussed in Section 5.2. Accordingly, it is assumed a continuous growth of the oxide phase which affects the value of the effective dielectric constant, i.e. increasing it, resulting in a stronger resonance (see Eq. (2.3)). On the other hand, growth of oxide shell may occur in expense of the metallic core, thus, reducing the particle size, which according to Eq. (2.3) and the trend observed for silver nanoparticles (Fig. 4.5), should lead to the decrease of the plasmon band intensity. Hence, these two phenomena would interplay in a complex manner yielding a small increase of the intensity.

Moreover, recalling again Eq. (2.3), the position of the maximum value is dependent on the surrounding environment, as the Frolich condition is satisfied at a different wavelength. Consequently, the formation of the oxide phase leads, also, to redshifts in the resonance wavelength as it is shown in the results presented in Section 4.3. Furthermore, it is noticed that this effect is more pronounced with small nanoparticles, according to the experiments.

From the results presented here, it is assumed a shorter time necessary for the oxidation of relatively smaller nanoparticles, with larger surface to volume ratio, as the exposed surface area is increased. Thus, supporting a relatively smaller increase of the plasmonic property and larger redshifts of the plasmonic band. However, it is important to mention that a complete explanation may require the analysis of the mechanism of oxide growth, in order to understand the simultaneous effects involving changes of the surrounding environment and modification of the volume of the nanoparticles. A possible study may include a quantitative analysis of the evolution of XPS spectra, comparing samples with copper nanoparticles of different size, and it can be combined with TEM images, which was already employed in other studies to investigate the mechanism of oxidation [19, 20, 131]. Additionally, further understanding of a possible relation between size of copper nanoparticles and modification of the plasmonic properties, due to the formation of the oxide phase, can be achieved by comparison of the time evolution of the extinction spectra, measured from more samples with larger or smaller copper nanoparticles.

In the end, the improved stability of the composition of ozonated copper nanoparticles, achieved by ozonation (Section 3.1), as discussed in Section 5.2, is considered as a possible solution to extend the lifetime of plasmonic copper nanoparticles, limiting further growth of the oxide phase. For this reason, the time evolution of the extinction spectra of ozonated nanoparticles is observed over a period of approximately five months.

Therefore, the intensity of the peak measured on the sample covered with larger nanoparticles, increased slightly (~ 0.5%) for a period of approximately two months. This behaviour is not observed in the case of smaller ozonated copper nanoparticles as the change in intensity can be considered negligible (see Fig. 4.7a).

Moreover, the initial formation of the oxide shell, due to the UV-ozone treatment, leads to the immediate red shift ($\Delta WL > 15\,nm$) of the plasmon band (red lines in Fig. 4.6b and Fig. 4.6d), resulting in a range of wavelength significantly different compared with pure copper nanoparticles. On the other side, the band position is nearly stable on the time scale of five months, showing just a very small and gradual redshift for larger nanoparticles (see green line Fig. 4.7b), which could be related to further oxidation and it is consistent with the slow increase of the peak intensity (see green lines in Fig. 4.7a).

Consequently, due to the small increase of intensity, observed only for larger nanoparticles, and the unchanged position of the plasmonic band, this procedure is considered to efficiently improve the stability of copper nanoparticles, opening the possibility for the fabrication of reliable plasmonic substrates based on copper nanoparticles, without requiring any special condition for the storing period.

5.5   SERS Measurements of Methylene Blue

The results previously discussed (see Section 5.3), demonstrated the plasmonic property of copper and silver nanoparticles produced by MaSCA, as described in Section 3.1. Thus, these nanostructures are suitable to increase the Raman scattering signal when analyte molecules are placed in their vicinity as explained in Section 2.2. The results presented in Section 4.4, demonstrate the advantageous application of metallic nanoparticles, since it is generally observed higher intensity of the detected signal when the analyte molecules are deposited on top of SERS substrates, rather than bare silicon. Hence, the perfromance of plasmonic substrate is optimized considering the parameters which affects the their efficiency, such as coverage and size of nanoparticles, and it is evaluated in terms of enhancement factor, according to the definition in Eq. (3.5) and limit of detection, corresponding to the lowest concentration of the analyte solution which allows to detect the vibrational spectrum. Additionally, the applicability of ozonated nanoparticles as SERS substrates, was investigated.

In these experiments, the effects of nanoparticles coverage and size are initially evaluated with $1mM$ aqueous solution of the methylene blue. Higher intensity of the spectra and larger values of the enhancement factor of copper and silver SERS substrates, are obtained from the samples fabricated with a longer deposition time, equivalent to the increase of the coverage of nanoparticles. More precisely, the enhancement factor is 1.2 times and 2.6 times larger, for copper SERS substrates and silver SERS substrates, respectively, fabricated with high coverage. Indeed, the distance between nanoparticles sitting on the substrate, is reduced when the coverage is increased, and so it is possible to increase the probability of randomly forming second generation hot spots, which will enhance further the signal detected (see Section 2.2).

Furthermore, the enhancement factor is 2.8 times and 1.3 times larger for copper and silver SERS substrates, respectively, when are considered nanoparticles with $d \sim 18 - 19\,nm$ in comparison with larger nanoparticles ($d \sim 24 - 26\,nm$). Indeed, the intensity of the plasmonic band increases proportionally to the the nanoparticles size as proved by the results discussed in Section 5.3. Consequently, analyte molecules will experience a more intense electromagnetic field when placed in the proximity of larger nanoparticles, leading to a higher probability to detect scattered photons.

These first results are different for ozonated copper SERS substrates, for which it is not clearly visible any increase of intensity. Indeed, the highest value of the enhancement factor estimated, among the different substrates fabricated with this procedure, is only 1.6, considering the optimal combination of coverage and size. Although the intensity of the plasmonic band is not affected significantly, the resonance wavelength is significantly red shifted after the UV-ozone treatment, due to the formation of an initial oxide phase (see Section 5.4). Thus, the excitation source employed is not adequate as it does not match the resonance wavelength of the SERS substrate. However, it is important to mention that it may be possible to achieve a good results with a different excitation source, but it cannot be compared with the performance of "as deposited" copper SERS substrates, since the experimental conditions are different.

Furthermore, the highest the enhancement factors, considering the peak located ~ $1400cm^-1$, obtained in these experiments, are ~ 4.5 and ~ 27.3 for copper SERS substrates and silver SERS substrates, respectively. These values are significantly smaller compared to the ones commonly found in the literature. In the case of copper nanoparticles-based substrates, the reported values of enhancement factors vary in a scale from ~ 10^3 [153] to ~ 10^5 [154] for certain SERS configurations. Meanwhile, SERS substrates with silver nanoparticles were found to be even more efficient than copper. For instance, silver nanodecahedra with sizes of 60-80 nm successfully enhanced Raman signal by ~ 10^6 order of magnitude when methylene blue was a probe molecule and $532\,nm$ excitation laser was used [155]. In other SERS studies of silver nanoparticles with a methylene blue, the enhancement factors vary from ~ 10^2 for spherical particles with diameter of $15\,nm$ [156], up to ~ 10^9 for larger spherical/rock-shaped particles with average size of $100\,nm$ [157]. Here, is important to emphasize that reported enhancement values were estimated from measurements where concentrations of the analyte were few magnitudes lower than $1mM$. As a consequence of the higher concentration, the deposited molecules, dried on top of the sample, will form a thick layer which may decrease their interaction with the plasmonic nanostructures, responsable for the signal enhancement.

For this reason, lower concentrations of methylene blue ($1\mu M$, $0.1\mu M$ and $0.01\mu M$) were dried on top of silver SERS substrates, which exhibited a stronger enhancement compared with copper, when the same conditions are considered, as discussed above. Hence, the intensity of the signal is decreased proportionally to the number of molecules deposited on the substrate, but it was still possible to detect the vibrational spectrum of methylene blue, without changing the experimental parameters.

Indeed, the enhancement factors estimated from the samples with $1\,\mu M$ and $0.1\,\mu M$, ranged from 1×10^4 to 4×10^4 and from 2×10^4 to 6×10^4, respectively, for silver SERS substrates covered with nanoparticles of different size. Interestingly, the intensity of the signal detected from $1mM$ solution is of the same order, or even lower, compared with $1\mu M$ solution. Thus, it is reasonable to assume the saturation of the nanoparticles layer, reached with a certatin concentration of analyte, above $0.1\,\mu M$.

Nevertheless, variation of the enhancement factor in between the range identified, are not necessary a consequence of the different size of the nanoparticles. Instead, slightly different values may be related with an uneven distribution of the molecules on the substrates, especially when low concentration of the analyte are dried on top of the substrate. Improvements in this step of the sample preparation, are facilitate the detection procedure.

In the end, the lowest concentration of methylene blue solution tested in this work is $0.01\mu M$ and it allowed to successfully detect the vibrational modes of the analyte molecule, obtaining enhancement factor of ~ 10^5. However, the characteristic peaks of methylene blue were reproduced only from one sample. Consequently, this result can not be considered reproducible but it proves the capability of detecting small amounts of analyte molecules with the methods for the sample preparation and substrate fabrication, emplyed in this study. Indeed, comparing to the limit of detection, reported for SERS experiments with silver nanoparticles for methylene blue, current result is comparable ($0.001\mu M$ [157]) or even better ($0.1\mu M$ [155]).

5.6   Metallic Nanoparticles Applicability as Matrices for MALDI MS

5.6.1   Copper Matrices

From mass spectra, obtained with bare copper nanoparticles matrix (nanoparticles deposited on silicon, Fig. 4.12) several copper containing ions are detected, where a few of them include acetonitrile. It is a solvent typically used as a mobile phase in a liquid chromatography laboratory where mass spectroscopy facility is located. Therefore, it enters into the sub-AP unit together with humidity and explains the detection of acetonitrile ions in mass spectra. Increasing the pressure, a decrease of ACN/water adducts can be observed as a result of lower gas influx into the sub-AP MALDI unit. Additionally, a small amount of silver ions is detected in these spectra, at lower pressure. Their presence is attributed to leftovers of sputtered silver which were trapped on the shielding grid of the EQMS of MaSCA, during previous experiments with silver cluster beams. Thus, it is possible that silver fragments were detached from the grid when hit by the beam of copper nanoparticles, and later became co-deposited, on the sample.

The performance of copper nanoparticles-based matrices is tested by measuring mass spectra of pig brain tissue. As presented in Fig. 4.13b (green), only a few ions peaks are detected in this configuration and related to high-mass lipid species. At the same time, only ions originating from the matrix itself are detected in the low-mass region of the ion spectrum from pig brain with copper nanoparticles. Consequently, the absence of charged molecular fragments suggests an inefficient energy transfer from laser to analyte, promoted by the copper nanoparticles.

Additionally, the results from copper nanoparticles are compared to the mass spectra obtained with the same measurement conditions but employing a matrix of thin copper film. It can be seen in Fig. 4.13 that the overall number of different ions detected in the mass spectrum of pig brain from copper thin film is larger and the relative signals are more intense, compared with the spectra obtained with a copper nanoparticles matrix. More precisely, considering the mass region of phosphatylcholine PC(34:1) in the pig brain spectra (Fig. 4.14a), the intensity of characteristic ions is higher with the copper thin film matrix. Moreover, lipid from the same group, PC(36:4), are detected with the sample coated with thin film, but not with the copper nanoparticles matrix (Fig. 4.14b).

Regarding the low-mass ion region, a few charged fragments of phospholipids are detected for the case of copper thin film matrix, differently to the result obtained with copper nanoparticles (see Fig. 4.13a), as discussed previously.

These results show that copper nanoparticles matrices are not suitable for the efficiency detection of lipids and fatty acids. The low ion variety and detected signal intensity, may indicate that copper nanoparticles weakly promote the desorption/ionization of the analyte.

5.6.2   Silver Matrices

Another set of samples were analyzed where copper nanoparticles matrices were replaced with silver nanoparticles matrices. The mass spectra obtained from pig brain

and beeswax, coated with silver nanoparticles, show a significant increase of the detected ion counts when the measurement was performed in negative ions mode, compared with positive ion mode. It is assumed that the high purity of the nanoparticles produced in this work, leads to a smaller presence of contaminants which may facilitate the formation of positive ions. However, this explanation requires a deeper investigation of the mechanism for the multitude of ionization reactions occurring during the experiment and it is out of this project scope.

Furthermore, ions corresponding to the analyte, were detected from the beeswax covered with silver nanoparticles when the measurement was performed with negative ions extraction (Fig. 4.17b), while only silver ions were registered (Fig. 4.17a) in positive ion mode, resulting in a larger variability of detected species, in the former case.

Moreover, the matrix efficiency of silver nanoparticles with different sizes was evaluated. This parameter did not affect the variability of the detected ions, however, the counts are higher from the sample with smaller nanoparticles ($d \sim 15nm$), resulting in a better quality of the spectrum. Consequently, it is assumed a greater efficiency of the desorption process, which can be related with the increase of the local heating due to the decreased dimension of silver nanoparticles.

This trend is also observed in the mass spectra of beeswax, obtained with silver nanoparticles of different sizes (Fig. 4.17b).

Specifically, the beeswax mass spectra from matrices with silver nanoparticles show signal from negative ions of saturated/unsaturated fatty acids with maximum at 367 m/z (tetracosanoic acid) only for the case of small particles (Fig. 4.17c). It is possible to detect some unsaturated fatty acids as well, as, for example shown in Fig. 4.17c. Also, a formation of [2M+Ag-H]- ions were observed in the higher mass regions Fig. 4.17b. The intensity of the signal is much higher than the signal detected from the sample covered with larger silver nanoparticles. It is important to notice that these ions were not detected in positive mode.

Laser irradiation of Silver Nanoparticles

When silver nanoparticles were exposed to laser beam, the surface coverage and nanoparticles size are affected, as observed by the analysis of SEM and AFM images presented in Section 4.5.3.

Indeed, the coverage and size of nanoparticles are lower in the areas irradiated by the laser beam, according to the images taken from the sample with the lowest energy (LE=5). The same trends are observe with higher energy irradiated on the sample, and, interestingly, nanoparticles were not detected inside the lines marked with the highest energy beam (LE=50). This result show a increased degradation of the deposited material for higher energies and it can be combined with the mass spectra measured from silver nanoparticles deposited on a silicon substrate, supporting the detection of silver ions after sublimation from the deposited nanostructure.

Additionally, a few stripes (Fig. 4.19f) are visible in the SEM images from the frame irradiated with LE=30 which may be a signal of nanoparticles melting and diffusion due to a thermal gradient between areas inside and outside the laser beam.

The obtained results show interesting phenomena on laser-nanoparticle interaction, which have not been addressed in literature so far. Further studies in this direction

would bring a considerable contribution into better understanding of heat transfer mechanisms affecting the LDI.

Chapter 6

Conclusion

In this work, the fabrication and performance of plasmonic substrates, covered with gas aggregated nanoparticles was investigated. These substrates were applied for the enhancement of Raman scattering signal and in the detection of lipids by MALDI-MS. High-purity silver and copper nanoparticles were produced by MaSCA, and deposited onto desired samples. The concurrent effects of several parameters related with the efficiency of the substrates, were studied. Indeed, optical properties of metallic nanoparticles were found to be affected by size, surface coverage and surrounding environment.

After the deposition, the morphology of nanoparticles was characterized by AFM, allowing to monitor the surface coverage and measure sizes of nanoparticles. The sizes were found to follow log-normal distribution for the case of nanoparticles, produced without mass-filtering. Size distribution of mass-filtered nanoparticles are well-fitted by Gaussian curves. Singly-charged clusters were found to dominate in the beam, while presence of small fractions of multiply-charged nanoparticles was also observed. Size deviations of the singly-charged nanoparticles were estimated to be within $\pm 10\,\%$, thus, showing very good efficiency of mass filtering.

Plasmonic application of plasmonic copper nanoparticles is often limited by the composition changes due to the rapid formation of oxide, which subsequently affects their performance. For the purpose to address this issue, a study of oxidation process of copper nanoparticles was included. The composition of copper nanoparticles, stored in ambient atmosphere, was analysed periodically by XPS. Cu_2O phase was detected immediately after the deposition followed by gradual transition to CuO phase with time. The same experiment was carried with copper nanoparticles, treated in UV-ozone environment, in order to test an alternative method which can limit the oxidation process. The obtained XPS spectra revealed the predominant formation of CuO phase, preventing nanoparticles from further oxidation.

Copper nanoparticles exhibited a distinguishable plasmon band with maximum around $590\,nm$, with negligible differences between the spectra of small and large nanoparticles, after the deposition. The formation of the oxide phase affected the characteristics of the plasmon band during the following five months. The resonance position was gradually shifted towards longer wavelengths, meanwhile the intensity changed only slightly. The redshift tendency of plasmon band of copper nanoparticles, was attributed to oxidation process which may be faster in the case of smaller particles. Further details need to be investigated in order to relate the evolution of the plasmonic peak with a precise description of the oxide formation.

On the other hand, extinction spectra of ozonated copper nanoparticles revealed higher stability of plasmon resonance which did not change significantly for a period of approximately five months. The improved stability of the plasmonic property was attributed to the stable composition of ozonated nanoparticles, exposed to ambient atmosphere condition. Consequently, the UV-ozone treatment is a potential method to efficiently extend the applicability of plasmonic copper nanostructures.

The extinction spectra for silver nanoparticles of different sizes, exhibited a plasmon band at shorter wavelengths ($370 - 388\,nm$), compared with copper nanoparticles. The spectra of larger silver nanoparticles showed a tendency to be more intense and shifted towards shorter wavelengths. The higher plasmon band intensity is in agreement with Mie theory. Meanwhile, the blue-shift of peak position disagreed with commonly accepted tendency of a red-shift, with an increase of nanoparticle size, which is assigned to the depolarization phenomenon. The discrepancy was explained by the effect of quartz substrate, which considerably increases the effective dielectric function of the medium surrounding the nanoparticles. This effect is especially strong for small nanoparticles.. One more plasmon band located at longer wavelengths (~ 470 nm) was observed for silver nanoparticles of all sizes, and it was assigned to the formation of closely located dimers, leading to additional transverse resonance. Interestingly, secondary plasmon bands, which were found in LSPR spectra of silver, were not observed for copper nanoparticles. It can be explained that copper nanoparticles were immediately oxidized in ambient atmosphere and presence of the oxide shell prevented the excitation of this resonance mode.

The composition(either copper or silver) and nanoparticle size, affecting the optical properties, were considered during the fabrication of plasmonic substrates for Raman spectroscopy. SERS measurements with both silver and copper nanoparticles showed low enhancement factors in the case of $1\,mM$ solution of methylene blue. However, the silver nanoparticles showed better SERS performance, compared with copper ones, was related with the more intense plasmon band. In the experiments with copper nanoparticles, the enhancement factor, obtained with ozonated copper SERS substrates, was lower than in the case of non-ozonated copper. It could be related to a significant red-shift of the plasmon band after the ozonation, moving it away from the laser wavelength. Consequently, a different excitation source, such as a He-Ne laser with $\lambda = 632.8\,nm$, may improve the enhancement provided by ozonated copper nanoparticles.

Low values of the enhancement factor in the experiments with $1\,mM$ solution of methylene blue, were suspected to be caused by too high concentration of the analyte, forming a thick layer, covering the nanoparticles. It may lead to shielding of the topmost molecules from an enhanced electromagnetic field, generated by the plasmonic particles. Thus, lower concentration ($0.1 - 0.01\,\mu M$) of the analyte solution was tested on silver nanoparticles. The obtain much higher enhancement proved the assumption showing the values of $10^4 - 10^5$, which are comparable with the literature. The best SERS enhancement factor of 3.63×10^5 was obtained, reaching the detection limit of $0.01\,\mu M$. Interestingly, a clear relation between the size of silver nanoparticles and enhancement factor was not observed. Therefore, substrates with small nanoparticles, prepared by MaSCA, would be preferable because of more efficient gas aggregation of relatively small nanoparticles (ca. $10 - 12\,nm$ in diameter) providing high beam intensity and requiring much shorter deposition times..

Due to COVID restrictions and limited access to the experimental facilities, the low concentrations of methylene blue were not tested using SERS substrates with copper

nanoparticles.

Copper and silver nanoparticles were also employed as matrices in MALDI-MS for the detection of lipids and fatty acids. Positive phospholipids ions were detected with copper nanoparticles. However, the intensity of the signal and the ion variety were lower compared with the experiment, where copper thin film was employed as a matrix. For this reason, the preparation of matrices with copper nanoparticles, was not considered an efficient method for the detection of lipids from biological tissues. The reasons of low efficiency of copper nanopartciles in the laser desorption experiments were not quite clear and this subject requires further investigation.

On the other hand, a greater intensity and variety of negative phospholipids ions and fatty acids ions were obtained with silver nanoparticles matrices. In this study, small nanoparticles, with mean diameter of $12\,nm$, were found to be the most efficient nanostructures to enhance the signals detected in mass spectra. Similar size of silver nanoparticles has been already mentioned in the literature as optimal for fabrication of LDI matrices [14, 26].

Interestingly, nanoparticles, fabricated by MaSCA, led to better quality of the mass spectra detected in negative ion mode. In earlier experiments, the opposite tendency was found [26]. This difference can be attributed to a a high purity and and monocrystallinity of silver nanoparticles produced with the method presented in this work.

Moreover, the morphology of silver nanoparticles, irradiated with laser beam at different energies, was investigated by AFM and SEM. The same laser as in MALDI experiments was used. The decrease of nanoparticles density was observed with both methods, suggesting the possible melting and surface diffusion of metallic material, after laser irradiation. The phenomenon was found to be strongly dependent on the laser power. With power increase, the particles in the irradiated areas were not found suggesting sublimation of silver Further studies are necessary to better understand the mechanism of the heat transfer between nanoparticles and laser source, affecting MALDI-MS.

64

Bibliography

[1] N. Fernandes, C. F. Rodrigues, A. F. Moreira, and I. J. Correia, "Overview of the application of inorganic nanomaterials in cancer photothermal therapy", Biomater. Sci. **8**, 2990–3020 (2020).

[2] A. Hasan, M. Morshed, A. Memic, S. Hassan, T. Webster, and H. Marei, "Nanoparticles in tissue engineering: applications, challenges and prospects", International Journal of Nanomedicine **13**, 5637–5655 (2018).

[3] S. Kim and M. Qi, "Copper nanorod array assisted silicon waveguide polarization beam splitter", Opt. Express **22**, 9508–9516 (2014).

[4] C. L. Tan and Y. T. Lee, "High-efficiency light-trapping effect using silver nanoparticles on thin amorphous silicon subwavelength structure", Opt. Lett. **38**, 4943–4945 (2013).

[5] C.-W. Yen, H. de Puig, J. O. Tam, J. Gómez-Márquez, I. Bosch, K. Hamad-Schifferli, and L. Gehrke, "Multicolored silver nanoparticles for multiplexed disease diagnostics: distinguishing dengue, yellow fever, and ebola viruses", Lab Chip **15**, 1638–1641 (2015).

[6] G. Qiu, Z. Gai, Y. Tao, J. Schmitt, G. A. Kullak-Ublick, and J. Wang, "Dual-functional plasmonic photothermal biosensors for highly accurate severe acute respiratory syndrome coronavirus 2 detection", ACS Nano **14**, 5268–5277 (2020).

[7] T. N. Ly and S. Park, "High performance detection of alzheimer's disease biomarkers based on localized surface plasmon resonance", Journal of Industrial and Engineering Chemistry **91**, 182–190 (2020).

[8] M. H. Jazayeri, T. Aghaie, R. Nedaeinia, M. Manian, and H. Nickho, "Rapid noninvasive detection of bladder cancer using survivin antibody-conjugated gold nanoparticles (gnps) based on localized surface plasmon resonance (lspr)", eng, Cancer Immunology, Immunotherapy **69**, 1833–1840 (2020).

[9] Q. Tong, W. Wang, Y. Fan, and L. Dong, "Recent progressive preparations and applications of silver-based sers substrates", TrAC Trends in Analytical Chemistry **106**, 246–258 (2018).

[10] M. Zannotti, A. Rossi, and R. Giovannetti, "Sers activity of silver nanosphere, triangular nanoplates, hexagonal nanoplates and quasi-spherical nanoparticles: effect of shape and morphology", Coatings **10**, 288 (2020).

[11] O. Olea-Mejía, M. Fernández-Mondragón, G. Rodríguez-de la Concha, and M. Camacho-López, "Sers-active ag, au and ag–au alloy nanoparticles obtained by laser ablation in liquids for sensing methylene blue", Applied Surface Science **348**, 66–70 (2015).

[12] J. Sekuła, J. Nizioł, W. Rode, and T. Ruman, "Silver nanostructures in laser desorption/ionization mass spectrometry and mass spectrometry imaging", Analyst **140**, 6195–6209 (2015).

[13] T. M. Guinan, O. J. R. Gustafsson, G. McPhee, H. Kobus, and N. H. Voelcker, "Silver coating for high-mass-accuracy imaging mass spectrometry of fingerprints on nanostructured silicon", Analytical Chemistry **87**, 11195–11202 (2015).

[14] C.-K. Chiang, W.-T. Chen, and H.-T. Chang, "Nanoparticle-based mass spectrometry for the analysis of biomolecules", Chem. Soc. Rev. **40**, 1269–1281 (2011).

[15] S. Jackson, K. Baldwin, L. Muller, V. Womack, A. Schultz, C. Balaban, and A. Woods, "Imaging of lipids in rat heart by maldi-ms with silver nanoparticles", Analytical and bioanalytical chemistry **406**, 1377–1386 (2014).

[16] T. Hayasaka, N. Goto-Inoue, N. Zaima, K. Shrivas, Y. Kashiwagi, M. Yamamoto, M. Nakamoto, and M. Setou, "Imaging mass spectrometry with silver nanoparticles reveals the distribution of fatty acids in mouse retinal sections", Journal of the American Society for Mass Spectrometry **21**, 1446–54 (2010).

[17] H. Hartmann, V. Popok, I. Barke, V. Oeynhausen, and K.-H. Meiwes-Broer, "Design and capabilities of an experimental setup based on magnetron sputtering for formation and deposition of size-selected metal clusters on ultra-clean surfaces", The Review of scientific instruments **83**, 073304 (2012).

[18] I. Barke, H. Hartmann, D. Rupp, L. Flückiger, M. Sauppe, M. Adolph, S. Schorb, C. Bostedt, R. Treusch, C. Peltz, S. Bartling, T. Fennel, K.-H. Meiwes-Broer, and T. Möller, "The 3d-architecture of individual free silver nanoparticles captured by x-ray scattering", Nature communications **6**, 6187 (2015).

[19] R. Boyd, I. Pilch, M. Garbrecht, M. Halvarsson, and U. Helmersson, "Double oxide shell layer formed on a metal nanoparticle as revealed by aberration corrected (scanning) transmission electron microscopy", Materials Research Express **1**, 025016 (2014).

[20] A. LaGrow, M. Ward, D. Lloyd, P. Gai, and E. Boyes, "Visualizing the Cu/Cu2O Interface Transition in Nanoparticles with Environmental STEM", Journal of the American Chemical Society **139**, 179–185 (2016).

[21] K. Rice, E. Walker, M. Stoykovich, and A. Saunders, "Solvent-dependent surface plasmon response and oxidation of copper nanocrystals", The Journal of Physical Chemistry C **115**, 1793–1799 (2011).

[22] K. P. Rice, A. S. Paterson, and M. P. Stoykovich, "Nanoscale kirkendall effect and oxidation kinetics in copper nanocrystals characterized by real-time, in situ optical spectroscopy", Particle & Particle Systems Characterization **32**, 373–380 (2015).

[23] E.K. Athanassiou, R.N. Grass and W.J.Stark, "Large-scale production of carbon-coated copper nanoparticles for sensor applications", Nanotechnology **17**, 1668–1673 (2006).

[24] I. Kim, Y. Kim, K. Woo, E.-H. Ryu, K. Y. Yon, G. Cao, and J. Moon, "Synthesis of oxidation-resistant core-shell copper nanoparticles", RSC Adv. **3**, 15169–15177 (2013).

[25] V. Popok, S. Novikov, Yurij, Y. Lebedinskij, A. Markeev, A. Andreev, I. Trunkin, A. Arsenin, and V. Volkov, "Gas-aggregated copper nanoparticles with long-term plasmon resonance stability", Plasmonics **16**, 333–340 (2021).

[26] V. Prysiazhnyi, F. Dycka, J. Kratochvil, V. Stranak, and V. N. Popok, "Effect of ag nanoparticle size on ion formation in nanoparticle assisted ldi ms", Applied Nano **1**, 3–13 (2020).

[27] Z. Wu, F. A. Fernandez-Lima, L. M. Perez, and D. H. Russell, "A New Copper Containing MALDI Matrix That Yields High Abundances of [Peptide + Cu]+ Ions", Journal of the American Society for Mass Spectrometry **20**, 1263–1271 (2009).

[28] M. Sakurai, M. Yang, J. Xu, M. T. Nguyen, T. Yonezawa, K. Hashimoto, and T. Fujino, "Copper ion production using zeolite and application to MALDI MS of small molecules", International Journal of Mass Spectrometry **434**, 179–184 (2018).

[29] S. Inasawa, M. Sugiyama, and Y. Yamaguchi, "Laser-induced shape transformation of gold nanoparticles below the melting point: the effect of surface melting", The Journal of Physical Chemistry B **109**, 3104–3111 (2005).

[30] R. L. Johnston, *Atomic and molecular clusters* (Taylor and Francis, 2002).

[31] R. Kubo, "Electronic Properties of Metallic Fine Particles. I", Journal of The Physical Society of Japan **17**, 975–986 (1962).

[32] B. Issendorff and O. Cheshnovsky, "Metal to insulator transitions in clusters", Annual review of physical chemistry **56**, 549–80 (2005).

[33] V. Vijayakrishnan, A. Chainani, D. Sarma, and C. Rao, "Metal-insulator transitions in metal clusters: a high-energy spectroscopy study of palladium and silver clusters", The Journal of Physical Chemistry **96**, 8679–8682 (1992).

[34] H. N. Aiyer, V. Vijayakrishnan, G. Subbanna, and C. Rao, "Investigations of Pd clusters by the combined use of HREM, STM, high-energy spectroscopies and tunneling conductance measurements", Surface Science **313**, 392–398 (1994).

[35] H. Haberland, T. Hippler, J. Donges, O. Kostko, M. Schmidt, and B. Issendorff, "Melting of sodium clusters: where do the magic numbers come from?", Physical review letters **94**, 035701 (2005).

[36] G. Mie, *Beiträge zur optik trüber medien, speziell kolloidaler metallösungen*, Vol. 25 (Sept. 1908), p. 377.

[37] Uwe Kreibig and Michael Vollmer, *Optical Properties of Metal Clusters* (Springer-Verlag Berlin Heidelberg, 1995).

[38] S. A. Maier, "Localized surface plasmons", in *Plasmonics: fundamentals and applications* (Springer US, 2007), pp. 65–88.

[39] M. Rycenga, C. Cobley, J. Zeng, W. Li, C. Moran, Q. Zhang, D. Qin, and Y. Xia, "Controlling the synthesis and assembly of silver nanostructures for plasmonic applications", Chemical reviews **111**, 3669–712 (2011).

[40] M. Rycenga, P. Camargo, W. Li, C. Moran, and Y. Xia, "Understanding the SERS Effects of Single Silver Nanoparticles and Their Dimers, One at a Time", The journal of physical chemistry letters **1**, 696–703 (2010).

[41] E. Hao and G. Schatz, "Electromagnetic fields around silver nanoparticles and dimers", The Journal of chemical physics **120**, 357–66 (2004).

[42] A. Govorov and H. Richardson, "Generating heat with metal nanoparticles", Nano Today **2**, 30–38 (2007).

[43] G. Baffou and R. Quidant, "Thermo-plasmonics: using metallic nanostructures as nano-sources of heat", Laser & Photonics Reviews **7**, 171–187 (2013).

[44] P. Jain, X. Huang, I. El-Sayed, and M. El-Sayed, "Review of some interesting surface plasmon resonance-enhanced properties of noble metal nanoparticles and their applications to biosystems", Plasmonics **2**, 107–118 (2007).

[45] S. Eustis and M. El-Sayed, "Why gold nanoparticles are more precious than pretty gold: noble metal surface plasmon resonance and its enhancement of the radiative and nonradiative properties of nanocrystals of different shapes", Chemical Society reviews **35**, 209–17 (2006).

[46] X. Huang, I. El-Sayed, W. Qian, and M. El-Sayed, "Cancer cell imaging and photothermal therapy in the near-infrared region by using gold nanorods", Journal of the American Chemical Society **128**, 2115–20 (2006).

[47] J. Anker, W. P. Hall, O. Lyandres, N. Shah, J. Zhao, and R. Duyne, "Biosensing with plasmonic nanosensors", Nature materials **7**, 442–53 (2008).

[48] J. Langer, S. Novikov, and L. Liz-Marzán, "Sensing using plasmonic nanostructures and nanoparticles", Nanotechnology **26**, 322001 (2015).

[49] C.V. Raman, *The Nobel Prize in Physics 1930*, Online accesed 02-March-2021, `https://www.nobelprize.org/prizes/physics/1930/summary/`.

[50] M. Fleischmann, P. Hendra, and A. Mcquillan, "Raman spectra of pyridine adsorbed at a silver electrode", Chemical Physics Letters **26**, 163–166 (1974).

[51] M. Fan, G. Andrade, and A. Brolo, "A review on the fabrication of substrates for surface enhanced raman spectroscopy and their applications in analytical chemistry", Analytica chimica acta **693**, 7–25 (2011).

[52] X.-M. Lin, Y. Cui, Y.-H. Xu, B. Ren, and Z.-Q. Tian, "Surface-enhanced raman spectroscopy: substrate-related issues", Analytical and bioanalytical chemistry **394**, 1729–45 (2009).

[53] S.-Y. Ding, E.-M. You, Z.-Q. Tian, and M. Moskovits, "Electromagnetic theories of surface-enhanced raman spectroscopy", Chem. Soc. Rev. **46**, 4042–4076 (2017).

[54] M. Moskovits, "Surface roughness and the enhanced intensity of raman scattering by molecules adsorbed on metals", The Journal of Chemical Physics **69**, 4159–4161 (1978).

[55] E. L. Ru and P. Etchegoin, *Principles of enhanced raman spectroscopy* (Elsevier, 2009).

[56] S.-Y. Ding, J. Yi, J.-F. Li, B. Ren, D. Wu, D. R. Panneerselvam, and Z.-Q. Tian, "Nanostructure-based plasmon-enhanced raman spectroscopy for surface analysis of materials", Nature reviews materials **1**, 16021 (2016).

[57] A. Balčytis, Y. Nishijima, S. Krishnamoorthy, A. Kuchmizhak, P. Stoddart, R. Petruškevičius, and S. Juodkazis, "From fundamental toward applied sers: shared principles and divergent approaches", Advanced Optical Materials **6**, 1800292 (2018).

[58] E. Le Ru, E. Blackie, M Meyer, and P. Etchegoin, "Surface enhanced raman scattering enhancement factors: a comprehensive study", The Journal of Physical Chemistry C **111**, 13794–13803 (2007).

[59] K. Kneipp, Y. Wang, H. Kneipp, L. Perelman, I. Itzkan, R. Dasari, and M. Feld, "Single molecule detection using surface-enhanced raman scattering (sers)", Physical Review Letters **78**, 1667 (1997).

[60] S. Nie and S. Emory, "Probing single molecules and single nanoparticles by surface-enhanced raman scattering", Science **275**, 1102–6 (1997).

[61] M. Natan, "Concluding remarks surface enhanced raman scattering", Faraday Discussions **132**, 321–328 (2006).

[62] G. Barbillon, "Latest novelties on plasmonic and non-plasmonic nanomaterials for sers sensing", Nanomaterials **10**, 1200 (2020).

[63] R. William, G. Das, V. Dantham, and R. Laha, "Enhancement of single molecule raman scattering using sprouted potato shaped bimetallic nanoparticles", Scientific Reports **9**, 10771 (2019).

[64] Q. K. Doan, M. H. Nguyen, C. D. Sai, V. T. Pham, H. H. Mai, N. H. Pham, T. C. Bach, and V. Tuyen, "Enhanced optical properties of ZnO nanorods decorated with gold nanoparticles for self cleaning surface enhanced Raman applications", Applied Surface Science **505**, 144593 (2020).

[65] G. Yang, X. Fang, Q. Jia, H. Gu, Y. Li, C. Han, and L.-L. Qu, "Fabrication of paper-based SERS substrates by spraying silver and gold nanoparticles for SERS determination of malachite green, methylene blue, and crystal violet in fish", Microchimica Acta **187**, 310 (2020).

[66] Z. Li, X. Huang, and G. Lu, "Recent developments of flexible and transparent sers substrates", Journal of Materials Chemistry C **8**, 3956–3969 (2020).

[67] C. Srichan, M. Ekpanyapong, M. Horprathum, P. Eiamchai, N. Nuntawong, P. Ditsayut, P. Danvirutai, E. Bohez, A. Wisitsoraat, and A. Tuantranont, "Highly-Sensitive Surface-Enhanced Raman Spectroscopy (SERS)-based Chemical Sensor using 3D Graphene Foam Decorated with Silver Nanoparticles as SERS substrate", Scientific Reports **6**, 23733 (2016).

[68] V. Shvalya, G. Filipič, J. Zavašnik, I. Abdulhalim, and U. Cvelbar, "Surface-enhanced raman spectroscopy for chemical and biological sensing using nanoplasmonics: the relevance of interparticle spacing and surface morphology", Applied Physics Reviews **7**, 031307 (2020).

[69] U. Wenning, B. Pettinger, and H. Wetzel, "Anguler-resolved raman spectroscopy of pyridine on copper and gold electrodes", Chemical Physics Letters **70**, 49–54 (1980).

[70] A. V. Markin, N. E. Markina, J. Popp, and D. Cialla-May, "Copper nanostructures for chemical analysis using surface-enhanced Raman spectroscopy", TrAC Trends in Analytical Chemistry **108**, 247–259 (2018).

[71] M. Keating, S. Song, G. Wei, D. Graham, Y. Chen, and F. Placido, "Ordered silver and copper nanorod arrays for enhanced raman scattering created via guided oblique angle deposition on polymer", The Journal of Physical Chemistry C **118**, 4878–4884 (2014).

[72] R.-C. Wang and C.-H. Li, "Cu, cu–cu2o core–shell, and hollow cu2o nanodendrites: structural evolution and reverse surface-enhanced raman scattering", Acta Materialia **59**, 822–829 (2011).

[73] M. Karas, D. Bachmann and F. Hillenkamp, "Influence of the Wavelength in High-Irradiance Ultraviolet Laser Desorption Mass Spectrometry of Organic Molecules", Analytical Chemistry **57**, 2935–2939 (1985).

[74] M. Karas and F. Hillenkamp, "Laser desorption ionization of proteins with molecular masses exceeding 10,000 daltons", Analytical Chemistry **60**, 2299–2301 (1988).

[75] K. Tanaka, H. Waki, Y. Ido, S. Akita, Y. Yoshida, T. Yoshida, and T. Matsuo, "Protein and polymer analyses up to m/z 100 000 by laser ionization time-of-flight mass spectrometry", Rapid Communications in Mass Spectrometry **2**, 151–153 (1988).

[76] K. Tanaka, *Nobel Lecture*, https://www.nobelprize.org/prizes/chemistry/2002/tanaka/lecture/, Online accessed 03- May-2021.

[77] M. Schürenberg, K. Dreiseward, and F. Hillenkamp, "Laser desorption/ionization mass spectrometry of peptides and proteins with particle suspension matrixes", Analytical Chemistry **71**, 221–229 (1999).

[78] J. Sunner, E. Dratz, and Y.-C. Chen, "Graphite surface-assisted laser desorption/ionization time-of-flight mass spectrometry of peptides and proteins from liquid solutions", Analytical Chemistry **67**, PMID: 8633776, 4335–4342 (1995).

[79] K. Dreiseward, "The desorption process in maldi", Chemical Reviews **103**, 395–426 (2003).

[80] R. Knochenmuss and R. Zenobi, "Maldi ionization: the role of in-plume processes", Chemical Reviews **103**, 441–452 (2003).

[81] C. Calvano, A. Monopoli, T. Cataldi, and F. Palmisano, "Maldi matrices for low molecular weight compounds: an endless story?", Analytical and Bioanalytical Chemistry **410**, 4015–4038 (2018).

[82] H. Abdelhamid, "Nanoparticle-based surface assisted laser desorption ionization mass spectrometry: a review", Microchimica Acta **186**, 682 (2019).

[83] R.A. Picca, C. D. Calvano, N. Cioffi and F. Palmisano, "Mechanisms of Nanophase-Induced Desorption in LDI-MS. A Short Review", Nanomaterials **7**, 75 (2017).

[84] K.M. Ng, S.L. Chau, H.W. Tang, X.G. Wei, K.C. Lau, F. Ye and A. M. C. Ng, "Ion-Desorption Efficiency and Internal-Energy Transfer in SurfaceAssisted Laser Desorption/Ionization: More Implication(s) for the Thermal-Driven and Phase-Transition-Driven Desorption Process", J. Phys. Chem. C **119**, 23708–23720 (2015).

[85] V. Prysiazhnyi, F. Dycka, J. Kratochvíl, J. Sterba, and V. Stranak, "Gas-aggregated Ag nanoparticles for detection of small molecules using LDI MS", Analytical and Bioanalytical Chemistry **412**, 1037–1047 (2019).

[86] M. A. Raza, Z. Kanwal, A. Rauf, A. Sabri, S. Riaz, and S. Naseem, "Size- and shape-dependent antibacterial studies of silver nanoparticles synthesized by wet chemical routes", Nanomaterials **6**, 74 (2016).

[87]G. Granata, T. Yamaoka, F. Pagnanelli, and A. Fuwa, "Study of the synthesis of copper nanoparticles: the role of capping and kinetic towards control of particle size and stability", Journal of Nanoparticle Research **18**, 133 (2016).

[88]J. X. Zhang and K. Hoshino, "Chapter 7 - nanomaterials for molecular sensing", in *Molecular sensors and nanodevices (second edition)*, edited by J. X. Zhang and K. Hoshino, Second Edition, Micro and Nano Technologies (Academic Press, 2019), pp. 413–487.

[89]S. Kaabipour and S. Hemmati, "A review on the green and sustainable synthesis of silver nanoparticles and one-dimensional silver nanostructures", Beilstein Journal of Nanotechnology **12**, 102–136 (2021).

[90]C. Daruich de Souza, B. Nogueira, and M. E. Rostelato, "Review of the methodologies used in the synthesis gold nanoparticles by chemical reduction", Journal of Alloys and Compounds **798**, 714–740 (2019).

[91]P. Zhang, P. Li, F. Li, and W. Jiang, "Lactic Acid Based Sol-Gel Process of Ag Nanoparticles and Crystalline Phase Control of Ni Particles in Aqueous Sol-Gel Process", Journal of Sol-Gel Science and Technology **72**, 398–404 (2014).

[92]M. Parashar, V. Shukla, and R. Singh, "Metal oxides nanoparticles via sol–gel method: a review on synthesis, characterization and applications", Journal of Materials Science: Materials in Electronics **31**, 3729–3749 (2020).

[93]G. C. Righini and A. Chiappini, "Glass optical waveguides: a review of fabrication techniques", Optical Engineering **53**, 071819 (2014).

[94]M. Niederberger, "Nonaqueous sol–gel routes to metal oxide nanoparticles", Accounts of chemical research **40**, 793–800 (2007).

[95]L. Mädler, H. Kammler, R. Mueller, and S. Pratsinis, "Controlled synthesis of nanostructured particles by flame spray pyrolysis", Journal of Aerosol Science **33**, 369–389 (2002).

[96]H. Torabmostaedi and T. Zhang, "Effect of nozzle geometry and processing parameters on the formation of nanoparticles using fsp", Chemical Engineering Research and Design **92**, 2470–2478 (2014).

[97]J. P. Hansen, J. Jensen, H. Livbjerg, and T. Johannessen, "Synthesis of ZnO Particles in a Quench-Cooled Flame Reactor", AIChE Journal **47**, 2413 –2418 (2001).

[98]D. Dufaux and R. Axelbaum, "Nanoscale unagglomerated nonoxide particles from a sodium coflow flame", Combustion and Flame **100**, 350–358 (1995).

[99]M. Keskar, C. Sabatini, C. Cheng, and M. Swihart, "Synthesis and characterization of silver nanoparticle-loaded amorphous calcium phosphate microspheres for dental applications", Nanoscale Advances **1**, 627–635 (2019).

[100]T. Karhunen, A. Lähde, J. Leskinen, R. Büchel, O. Waser, U. Tapper, and J. Jokiniemi, "Transition metal-doped lithium titanium oxide nanoparticles made using flame spray pyrolysis", ISRN Nanotechnology **2011**, 1–6 (2011).

[101]B. Schimmoeller, H. Schulz, S. Pratsinis, A. Bareiss, A. Reitzmann, and B. Kraushaar-Czarnetzki, "Ceramic foams directly-coated with flame-made v2o5/tio2 for synthesis of phthalic anhydride", Journal of Catalysis **243**, 82–92 (2006).

[102]R. Strobel and S. Pratsinis, "Flame aerosol synthesis of smart nanostructured materials", Journal of Materials Chemistry **17**, 4743–4756 (2007).

[103]J. R. Creighton and P. Ho, "Introduction to Chemical Vapor Deposition (CVD)", in *Chemical Vapor Deposition*, edited by J.-H. Park (ASM International, 2001), pp. 1–23.

[104]P. Piszczek and A. Radtke, "Silver nanoparticles fabricated using chemical vapor deposition and atomic layer deposition techniques: properties, applications and perspectives: review", in *Noble and precious metals*, edited by M. S. Seehra and A. D. Bristow (IntechOpen, Rijeka, 2018) Chap. 9.

[105]M. Swihart, "Vapor-phase synthesis of nanoparticles", Current Opinion in Colloid & Interface Science **8**, 127–133 (2003).

[106]M. Ullah, M. Ali, and S. B. Abd Hamid, "Surfactant-assisted ball milling: a novel route to novel materials with controlled nanostructure-a review", Reviews on Advanced Materials Science **37**, 1–14 (2014).

[107]C. Dhand, N. Dwivedi, X. J. Loh, A. Ng, N. Verma, R. Beuerman, R. Lakshminarayanan, and S. Ramakrishna, "Methods and strategies for the synthesis of diverse nanoparticles and their applications: a comprehensive overview", RSC Adv. **5**, 105003–105037 (2015).

[108]N. Poudyal, C.-b. Rong, and J. Liu, "Morphological and magnetic characterization of fe, co, and feco nanoplates and nanoparticles prepared by surfactants-assisted ball milling", Journal of Applied Physics **109**, 07B526–07B526 (2011).

[109]T. Jayaramudu, G. M. Raghavendra, K. Varaprasad, G. Subba Reddy, A. Reddy, K. Sudhakar, and R. Sadiku, "Preparation and characterization of poly (ethylene glycol) stabilized nano silver particles by a mechanochemical assisted ball mill process", Journal of Applied Polymer Science **133**, 43027 (2016).

[110]G. Khayati and K. Janghorban, "An investigation on the application of process control agents in the preparation and consolidation behavior of nanocrystalline silver by mechanochemical method", Advanced Powder Technology **23**, 808–813 (2012).

[111]P. Jamkhande, N. Ghule, A. Bamer, and M. Kalaskar, "Metal nanoparticles synthesis: an overview on methods of preparation, advantages and disadvantages, and applications", Journal of Drug Delivery Science and Technology **53**, 101174 (2019).

[112]V. Popok, I. Barke, E. Campbell, and K.-H. Meiwes-Broer, "Cluster–surface interaction: from soft landing to implantation", Surface Science Reports **66**, 347–377 (2011).

[113]M. Raffi, A. Rumaiz, M. Hassan, and S. Shah, "Studies of the growth parameters for silver nanoparticle synthesis by inert gas condensation", Journal of Materials Research **22**, 3378 –3384 (2007).

[114]A. Simchi, R. Ahmadi, s. m. seyed Reihani, and A. Mahdavi, "Kinetics and mechanisms of nanoparticle formation and growth in vapor phase condensation process", Materials & Design **28**, 850–856 (2007).

[115]O. Hagena, "Cluster ion sources (invited)", Review of Scientific Instruments **63**, 2374 –2379 (1992).

[116] A. Yumoto, F. Hiroki, I. Shiota, and N. Niwa, "In situ synthesis of titanium-aluminides in coating with supersonic free-jet pvd using ti and al nanoparticles", Surface and Coatings Technology **169-170**, 499–503 (2003).

[117] S. Peli, E. Cavaliere, G. Benetti, M. Gandolfi, M. Chiodi, C. Cancellieri, C. Giannetti, G. Ferrini, L. Gavioli, and F. Banfi, "Mechanical properties of ag nanoparticle thin films synthesized by supersonic cluster beam deposition", The Journal of Physical Chemistry C **120**, 4673–4681 (2016).

[118] A. P. Caricato, A. Luches, and M. Martino, "Laser fabrication of nanoparticles", in *Handbook of nanoparticles*, edited by M. Aliofkhazraei (Springer International Publishing, Cham, 2015), pp. 1–18.

[119] F. Mafuné, J.-y. Kohno, Y. Takeda, and T. Kondow, "Formation and size control of silver nanoparticles by laser ablation in aqueous solution", The Journal of Physical Chemistry B **104**, 9111–9117 (2000).

[120] R. Poursalehi, A. Zad, and S. M. Mahdavi, "Size, composition and optical properties of copper nanoparticles prepared by laser ablation in liquids", Applied Physics A **88**, 415–419 (2007).

[121] M. Muniz-Miranda, C. Gellini, A. Simonelli, M. Tiberi, F. Giammanco, and E. Giorgetti, "Characterization of copper nanoparticles obtained by laser ablation in liquids", Applied Physics A **110**, 829–833 (2013).

[122] M. Maciulevičius, A. Vinčiūnas, M. Brikas, A. Butsen, N. Tarasenka, N. Tarasenko, and G. Raciukaitis, "Pulsed-laser generation of gold nanoparticles with on-line surface plasmon resonance detection", Applied Physics A **111**, 289–295 (2013).

[123] A. A. Ashkarran, "A novel method for synthesis of colloidal silver nanoparticles by arc discharge in liquid", Current Applied Physics **10**, 1442–1447 (2010).

[124] V. Popok and L. Gurevich, "Charge states of size-selected silver nanoparticles produced by magnetron sputtering", Journal of Nanoparticle Research **21**, 171 (2019).

[125] G. Barmparis, Z. Łodziana, N. López, and I. Remediakis, "Nanoparticle shapes by using wulff constructions and first-principles calculations", Beilstein Journal of Nanotechnology **6**, 361–368 (2015).

[126] S. Pratontep, S. Carroll, C. Xirouchaki, M. Streun, and R. Palmer, "Size-selected cluster beam source based on radio frequency magnetron plasma sputtering and gas condensation", Review of Scientific Instruments **76**, 045103–045103 (2005).

[127] W. Cao and H. Elsayed-Ali, "Stability of ag nanoparticles fabricated by electron beam lithography", Materials Letters **63**, 2263–2266 (2009).

[128] T. Oates, M. Losurdo, S. Noda, and K Hinrichs, "The effect of atmospheric tarnishing on the optical and structural properties of silver nanoparticles", Journal of Physics D: Applied Physics **46**, 145308 (2013).

[129] C. Gattinoni and A. Michaelides, "Atomistic details of oxide surfaces and surface oxidation: the example of copper and its oxides", Surface Science Reports **70**, 424–447 (2015).

[130] J. Leitner, D. Sedmidubský, M. Lojka, and O. Jankovský, "The effect of nanosizing on the oxidation of partially oxidized copper nanoparticles", Materials **13**, 2878 (2020).

[131] J. Kim, S. Ehrman, and T. Germer, "Influence of particle oxide coating on light scattering by submicron metal particles on silicon wafers", Applied Physics Letters **84**, 1278 –1280 (2004).

[132] L. Xu, C. Srinivasakannan, J. Peng, L. Zhang, and D. Zhang, "Synthesis of cu-cuo nanocomposite in microreactor and its application to photocatalytic degradation", Journal of Alloys and Compounds **695**, 263–269 (2016).

[133] L. Yang, D. Chu, and L. Wang, "Cuo core-shell nanostructures: precursor-mediated fabrication and visible-light induced photocatalytic degradation of organic pollutants", Powder Technology **287**, 346–354 (2016).

[134] N. Jardón-Maximino, P. M., R. Sierra-Ávila, C. Avila-Orta, E. Jiménez-Regalado, A. Bello, P. González-Morones, and G. Cadenas-Pliego, "Oxidation of copper nanoparticles protected with different coatings and stored under ambient conditions", Journal of Nanomaterials **2018**, 1–8 (2018).

[135] Y. Wang, Q. Zhang, Y. Wang, L. Vazquez Besteiro, L. Yannan, H. Tan, Z. Wang, A. Govorov, Z. Jin, J. Cooper, J. Zhao, G. Chen, M. Chaker, and D. Ma, "Ultrastable plasmonic cu-based core–shell nanoparticles", Chemistry of Materials **33**, 695–705 (2020).

[136] A. Curry, G. Nusz, A. Chilkoti, and A. Wax, "Substrate effect on refractive index dependence of plasmon resonance for individual silver nanoparticles observed using darkfield microspectroscopy", Optics express **13**, 2668–77 (2005).

[137] T. Ghodselahi and O. Vesaghi, "Localized surface plasmon resonance of cu@cu 2o core–shell nanoparticles: absorption, scattering and luminescence", Physica B: Condensed Matter **406**, 2678–2683 (2011).

[138] O. Peña-Rodríguez and U. Pal, "Effects of surface oxidation on the linear optica properties of cu nanoparticles", Journal of the Optical Society of America B **28**, 2735–2739 (2011).

[139] S. Nilsson, D. Albinsson, T. Antosiewicz, J. Fritzsche, and C. Langhammer, "Resolving single cu nanoparticle oxidation and kirkendall void formation with ¬in situ plasmonic nanospectroscopy and electrodynamic simulations", Nanoscale **11**, 20725–20733 (2019).

[140] S. Bok, G.-H. Lim, and B. Lim, "Uv/ozone treatment for adhesion improvement of copper/epoxy interface", Journal of Industrial and Engineering Chemistry **46**, 199–202 (2017).

[141] S. Novikov, V. Popok, A. Evlyukhin, M. Hanif, P. Morgen, J. Fiutowski, J. Beermann, H.-G. Rubahn, and S. Bozhevolnyi, "Highly stable monocrystalline silver clusters for plasmonic applications", Langmuir **33**, 6062–6070 (2017).

[142] H. Haberland, *History, some basics, and an outlook* (John Wiley & Sons, Ltd, 2017) Chap. 1, pp. 1–21.

[143] S. Marom, M. Plesser, R. Modi, N. Manini, and M. D. Vece, "'planetary' silver nanoparticles originating from a magnetron sputter plasma", Journal of Physics D: Applied Physics **52**, 095301 (2018).

[144] Z.-T. Jiang, S. Thurgate, and P. Wilkie, "Line structure in photoelectron and auger electron spectra of cuox/cu and cu by auger photoelectron coincidence spectroscopy (apecs)", Surface and Interface Analysis **31**, 287 –290 (2001).

[145]M. Biesinger, L. Lau, A. Gerson, and R. Smart, "Resolving surface chemical states in XPS analysis of first row transition metals, oxides and hydroxides: Sc, Ti, V, Cu and Zn", Applied Surface Science **257**, 887–898 (2010).

[146]S. Dutta Roy, M. Ghosh, and J. Chowdhury, "Adsorptive parameters and influence of hot geometries on the SER(R) S spectra of methylene blue molecules adsorbed on gold nanocolloidal particles", Journal of Raman Spectroscopy **46**, 451–461 (2015).

[147]U. Hübner, W. Morgenroth, H. Meyer, T. Sulzbach, B. Brendel, and W. Mirandé, "Downwards to metrology in nanoscale: determination of the afm tip shape with well-known sharp-edged calibration structures", Applied Physics A **76**, 913–917 (2003).

[148]S. Poulston, P. Parlett, P Stone, and M. Bowker, "Surface oxidation and reduction of cuo and cu2o studied using xps and xaes", Surface and interface analysis **24**, 811–820 (1996).

[149]XPS Reference Table Of Elements, Accessed May 20th, 2021, Thermo Fisher Scientific, https://xpssimplified.com/elements/copper.php.

[150]F. A. Makareviciute and A. Pico, "Plasmonic properties of supported metal nanoparticles", (2020).

[151]P. Barber, R. Chang, and H. Massoudi, "Surface-enhanced electric intensities on large silver spheroids", Physical Review Letters **50**, 997–1000 (1983).

[152]M Meier and A Wokaun, "Enhanced fields on large metal particles: dynamic depolarization", Optics letters **8**, 581–3 (1983).

[153]P. Baruah, A. Singh, L. Rangan, A. Sharma, and A. Khare, "Optimization of copper nanoparticles synthesized by pulsed laser ablation in distilled water as a viable sers substrate for karanjin", Materials Chemistry and Physics **220**, 111–117 (2018).

[154]M. Dendisova, V. Prokopec, M. Člupek, and P. Matějka, "Comparison of sers effectiveness of copper substrates prepared by different methods: what are the values of enhancement factors?", Journal of Raman Spectroscopy **43**, 181–186 (2012).

[155]V. Xuan Hoa, N. Dien, T. Thu, H. Pham, C Tran, T. T. Tran, N Ca, P Tho, V. Nguyen, and P. Do, "The sensitive detection of methylene blue using silver nanodecahedra prepared through a photochemical route", RSC Advances **10**, 38974–38988 (2020).

[156]O. Olea-Mejia, M. Fernández-Mondragón, G. Concha, and M. Camacho-López, "SERS-active Ag, Au and Ag–Au alloy nanoparticles obtained by laser ablation in liquids for sensing methylene blue", Applied Surface Science **348**, 66–70 (2015).

[157]S. Imran and S. Sartale, "SILAR grown Ag nanoparticles as an efficient large area SERS substrate", Journal of Raman Spectroscopy **49**, 1274–1287 (2017).

Appendix A

AFM Images

In this section, additional AFM images are shown. These are relative to copper nanoparticles (Fig. A.1), size selected at $V_{EQMS} = 0\,V$ (Fig. A.1a and Fig. A.1b), $V_{EQMS} = 700\,V$ (Fig. A.1c and Fig. A.1d) and $V_{EQMS} = 1300\,V$. Meanwhile, silver nanoparticles deposited at $V_{E}QMS = 200\,V$ (Fig. A.2a and Fig. A.2b), $V_{EQMS} = 500\,V$ (Fig. A.2c and Fig. A.2d), $V_{EQMS} = 1100\,V$ (Fig. A.2e and Fig. A.2f), and $V_{EQMS} = 1700\,V$ (Fig. A.2g and Fig. A.2h), are presented in (Fig. A.2). The structures marked with white circles, were considered for the height analysis presented in Fig. 4.2 and Fig. 4.3.
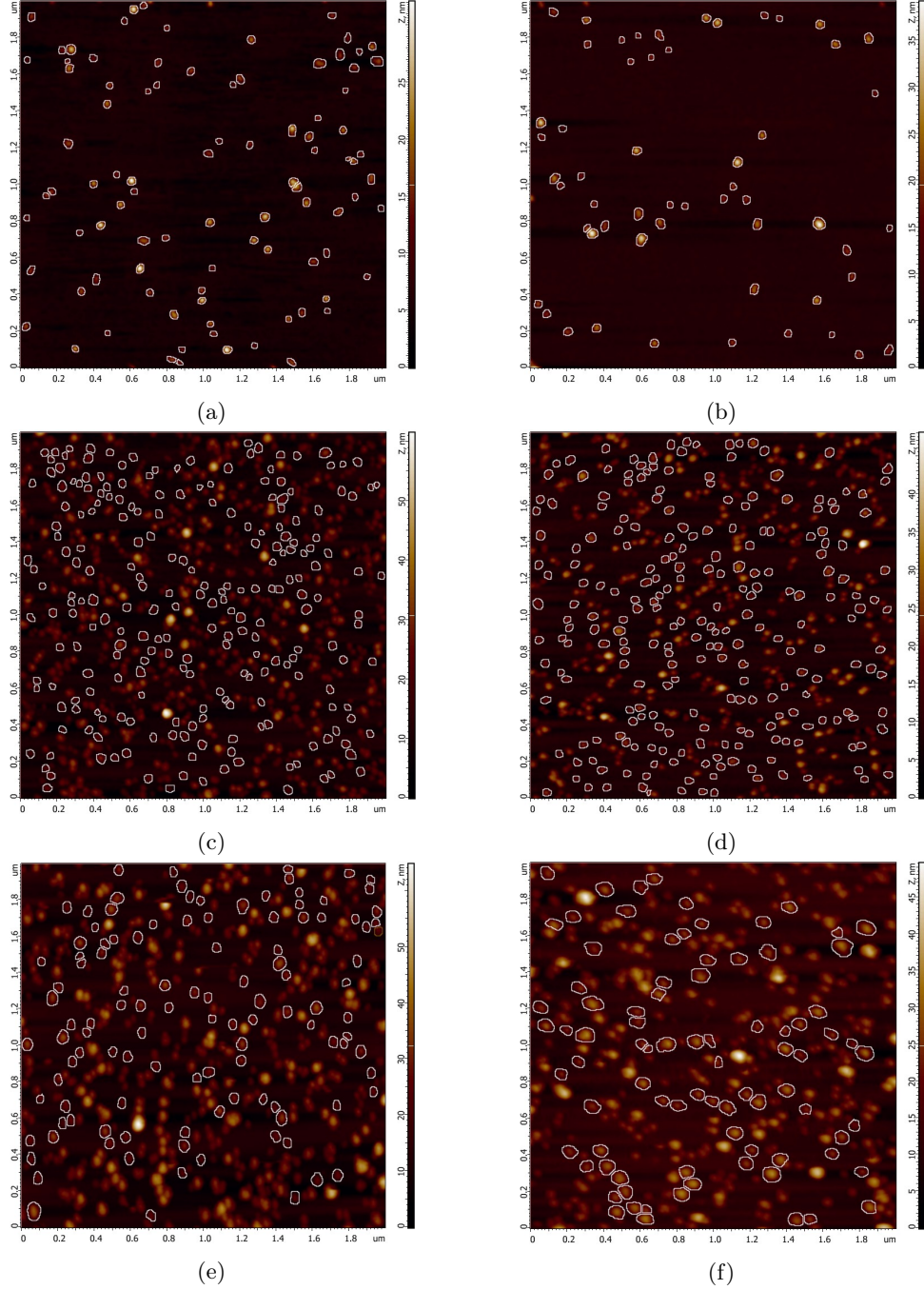
FIGURE A.1: AFM images of copper nanoparticles size selected at
a,b) $0\,V$, c,d) $700\,V$, and e,f) $1300\,V$
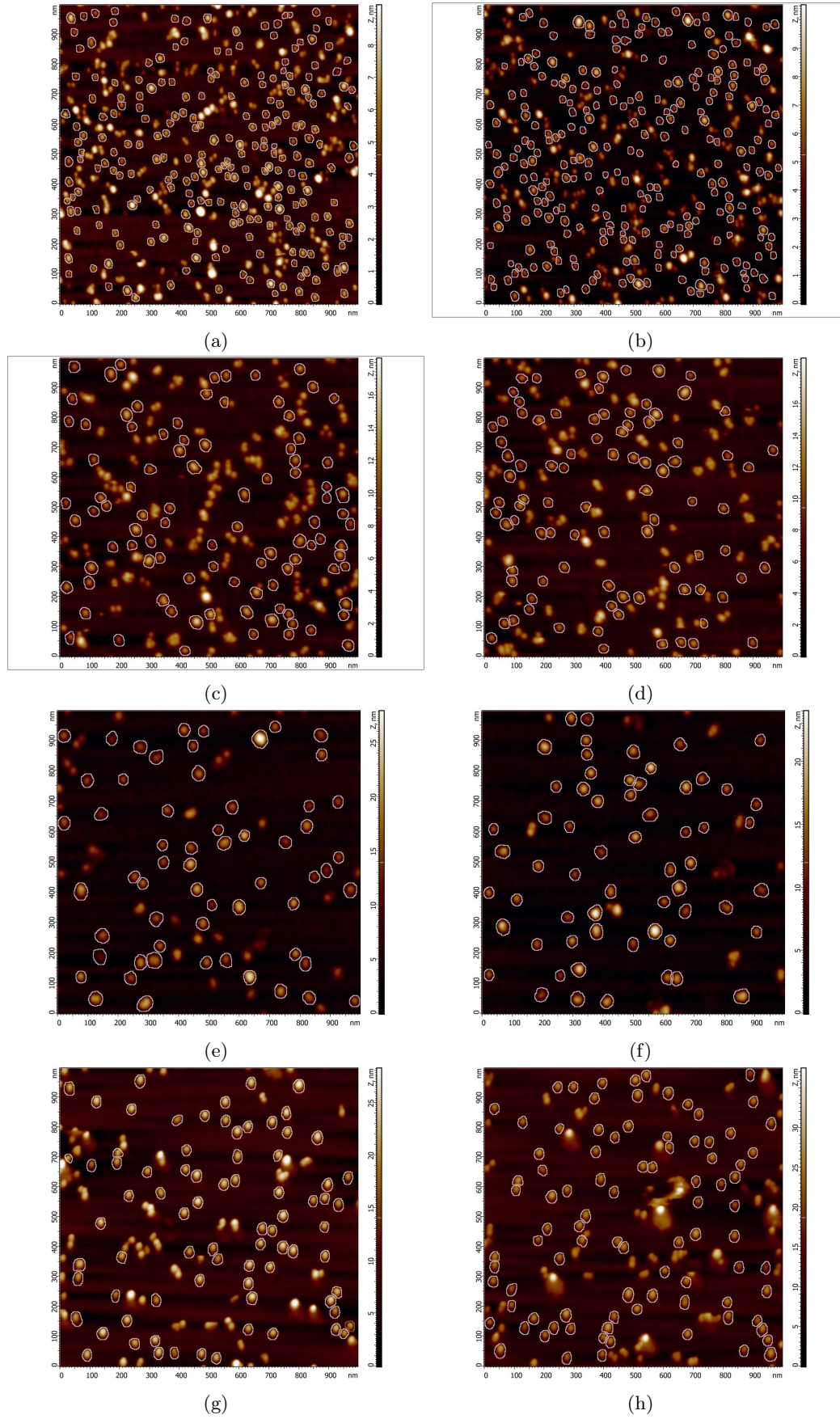
FIGURE A.2: AFM images of silver nanoparticles size selected at a,b)
200 V, c,d) 500 V, e,f) 1100 V and g,h) 1700 V

Appendix B

Extinction Spectra of Copper Nanoparticles

Time evolution of extinction spectra exhibited by copper NPs are presented in this section, supporting the results, shown in Section 4.3.2. These spectra are relative to the periods since the deposition of the particles to the following two months (panels a), the next three months (panels b). The measurements in Fig. B.1 and Fig. B.2 were obtained from non-ozonated copper nanoparticles of different size, small and large, respectively. Similarly, Fig. B.3 and Fig. B.4 illustrate the extinction spectra of small and large, respectively, ozonated copper nanoparticles.

(a)   (b)
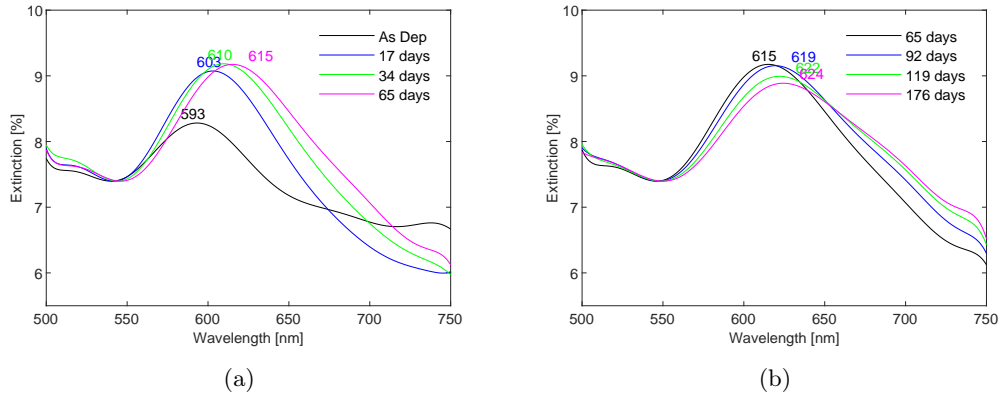
FIGURE B.1: Extinction spectra of pure copper nanoparticles with $d \sim 19\,nm$: a) during the first two months after the deposition and b) during the following four months
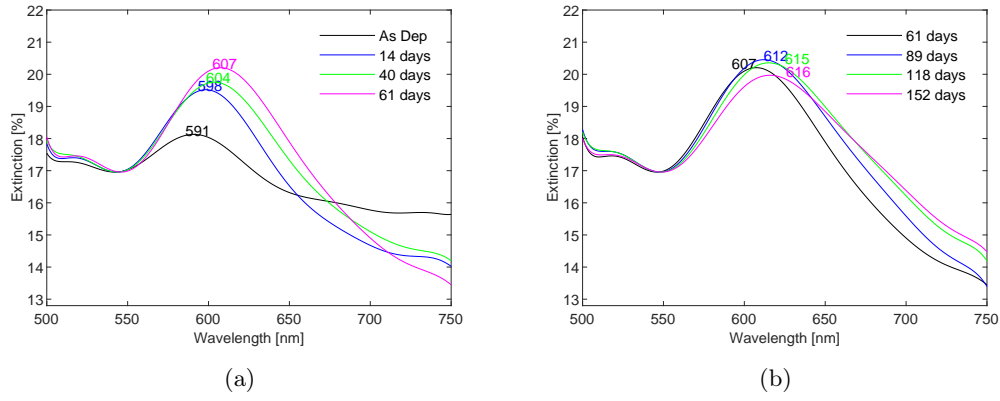
FIGURE B.2: Extinction spectra of pure copper nanoparticles with $d \sim 24\,nm$, a) during the first two months after the deposition and b) during the following three months
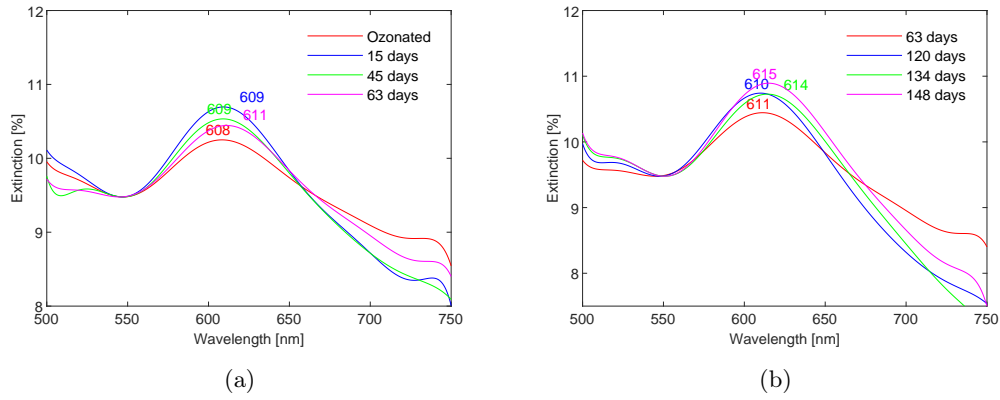

FIGURE B.3: Extinction spectra of ozonated copper nanoparticles with $d \sim 19\,nm$, a) during the first two months after the ozonation and b) during the following three months
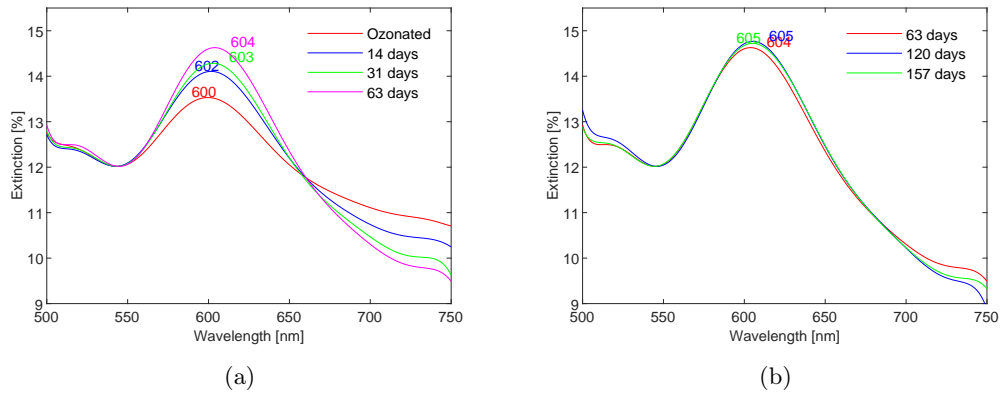

FIGURE B.4: Extinction spectra of ozonated copper nanoparticles with $d \sim 24\,nm$, a) during the first two months after the ozonation and b) during the following three months

Appendix C

SERS Spectra

In this section, several SERS spectra measured in different spots on the samples with $c_{MB} = 1\,\mu M$ (Fig. C.1), $c_{MB} = 1\,\mu M$ (Fig. C.2) and $c_{MB} = 1\,\mu M$ (Fig. C.3), are presented. Different sizes of nanoparticles are considered for each set of samples. The average value of the enhancement factors are presented Table C.1 (fourth and fifth columns), together with the number of spectra considered (third column), mean size of the nanoparticles (second column) and concentration of methylene blue (first column).

TABLE C.1: Average value of the enhancement factors evaluate for different concentrations of methylene blue dried onto silver SERS substrates. The number of spectra considered and the mean size of deposited nanoparticles are also indicated

$c_{MB}\,[\mu M]$	d [nm]	# spectra	avg EF @$1400cm^{-1}$	avg EF @$1600cm^{-1}$
	12	4	$(2.84 \pm 0.16) \times 10^4$	$(1.33 \pm 0.09) \times 10^4$
1	18	9	$(1.70 \pm 0.54) \times 10^4$	$(0.91 \pm 0.31) \times 10^4$
	26	4	$(2.46 \pm 1.14) \times 10^4$	$(1.57 \pm 0.87) \times 10^4$
	12	5	$(5.27 \pm 0.6) \times 10^4$	$(2.39 \pm 0.16) \times 10^4$
0.1	18	5	$(3.22 \pm 0.5) \times 10^4$	$(1.82 \pm 0.52) \times 10^4$
	26	4	$(2.54 \pm 0.4) \times 10^4$	$(1.65 \pm 0.4) \times 10^4$
0.01	12	4	$(3 \pm 0.72) \times 10^5$	$(1.12 \pm 0.24 \times 10^5$

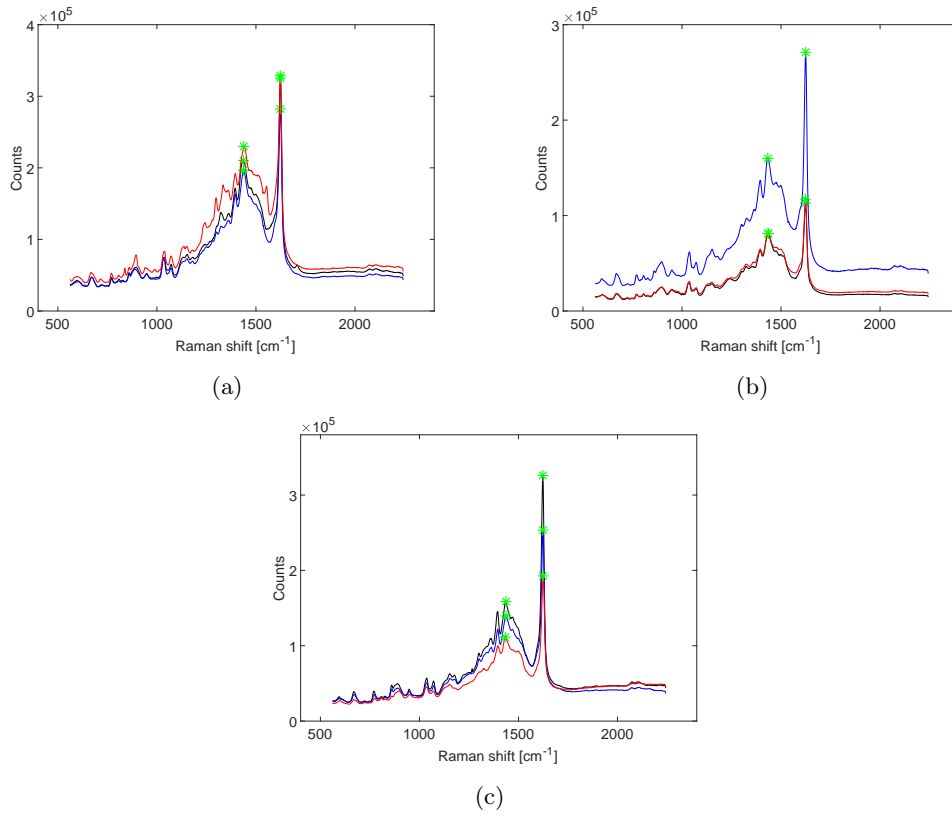FIGURE C.1: SERS spectra from $1\,\mu M$ solution of methylene blue dried onto silver SERS substrates with mean size a) $d \sim 12\,nm$, b) $d \sim 18\,nm$ and c) $d \sim 26\,nm$. The positions of the peaks considered for the evaluation of the enhancement factors are marked in green

(a)

(b)

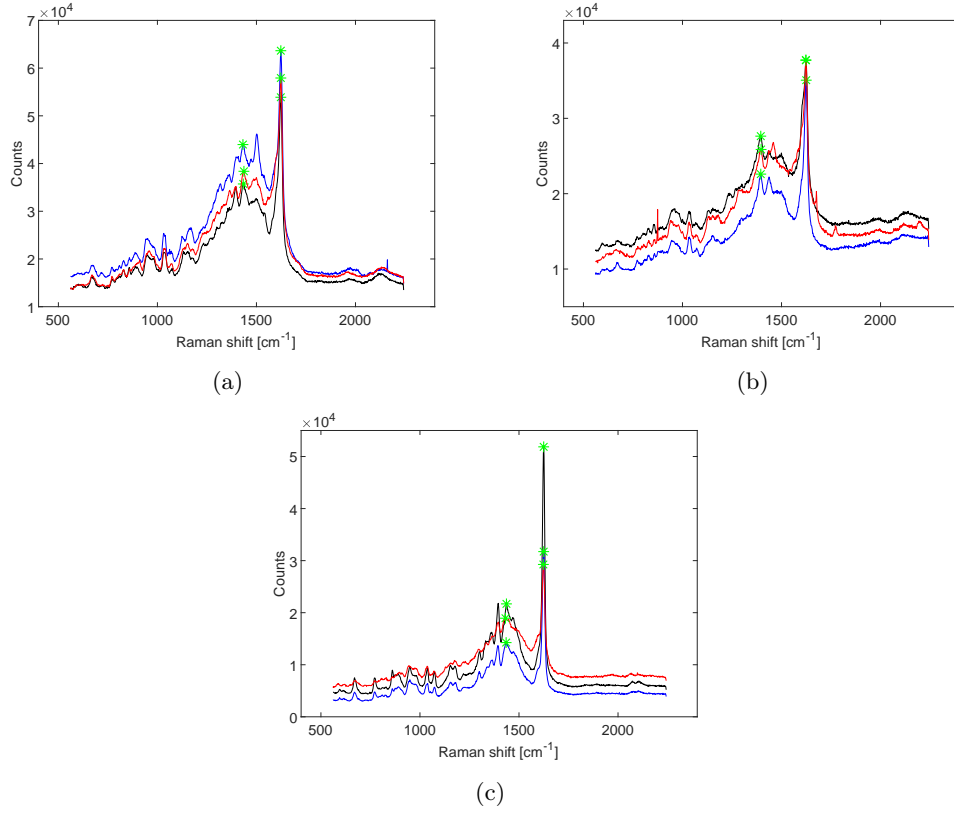
(c)

FIGURE C.2: SERS spectra from $0.1\,\mu M$ solution of methylene blue dried onto silver SERS substrates with mean size a) $d \sim 12\,nm$, b) $d \sim 18\,nm$ and c) $d \sim 26\,nm$. The positions of the peaks considered for the evaluation of the enhancement factors are marked in green

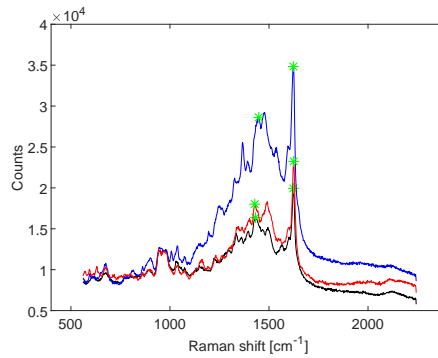FIGURE C.3: SERS spectra from $1\,\mu M$ solution of methylene blue dried onto silver SERS substrates with mean size $d \sim 12\,nm$. The positions of the peaks considered for the evaluation of the enhancement factors are marked in green